

ABSTRACT

FUOCO, LINDSAY CHRISTINE. Flux Synthesis of Metal Oxides and Investigations of their Photoelectrochemical and Magnetic Properties. (Under the direction of Prof. Paul A. Maggard).

The renewable production of fuels from sunlight has generated intense research over the past few decades in the field of semiconducting photoelectrodes, such as for the photon-driven reduction of water. Much research has focused on the identification of materials capable of absorbing visible-light, a major portion of the solar spectrum. Metal-oxides are considered the most promising photoelectrode materials due to their relative stability. However, most have large sized bandgaps making them incapable of visible-light absorption. My research efforts in this area involve the investigation and identification of new metal-oxide based *p*-type photoelectrode materials capable of hydrogen production under visible-light irradiation. Polycrystalline films of $\text{Cu}_5\text{Ta}_{11}\text{O}_{30}$ and $\text{Cu}_3\text{Ta}_7\text{O}_{19}$ were prepared on fluorine-doped tin oxide (FTO) glass starting from their flux synthesis as highly-faceted micron-sized particles. Each photoelectrode material was prepared under various annealing and oxidation temperatures to evaluate their effects on the photocurrent response. The synthetic preparation, phase purity, morphology and optical absorption of each film were evaluated. Films were photoelectrochemically characterized and the flat-band potentials of each were determined by Mott-Schottky analysis and used to determine their valence and conduction band positions.

The second section is focused on the half-metallic, double-perovskite oxides with the composition A_2BReO_6 ($\text{A} = \text{Sr}$ or Ba ; $\text{B} = \text{Fe}$ or Cr). These materials have been the focus of

intense research interest owing to the discovery of low-field intergrain-tunneling magnetoresistance in members of this family. Particle size, morphology and the amount of B/B' site ordering have also been shown to significantly affect the observed intergrain tunneling magnetoresistance. However, current synthesis methods do not allow for the tunable manipulation of any of these types of particle characteristics. My research efforts in this area have focused on several reduced rhenates and use of flux-mediated synthesis as an alternative approach that allows for the tunability of their particle sizes. The flux amount, heating duration and cooling rates were varied and investigated for their effects on particle sizes, extent of B/B' site ordering, as well as magnetic and electrical properties.

© Copyright 2012 by Lindsay Christine Fuoco

All Rights Reserved

Flux Synthesis of Metal Oxides and Investigations of their Photoelectrochemical and
Magnetic Properties

by
Lindsay Christine Fuoco

A dissertation submitted to the Graduate Faculty of
North Carolina State University
in partial fulfillment of the
requirements for the degree of
Doctor of Philosophy

Chemistry

Raleigh, North Carolina

2012

APPROVED BY:

Dr. Paul A. Maggard
Committee Chair

Dr. Mike H. Whangbo

Dr. David Shultz

Dr. Christopher Gorman

DEDICATION

This work is dedicated to all of my family.

BIOGRAPHY

Lindsay Christine Fuoco was born on April 6th, 1984 in Arcadia, California. In the fall of 2002, she enrolled in Virginia Commonwealth University and graduated in the spring of 2006. In the fall of 2006, she joined Professor Paul A. Maggard's research group at North Carolina State University and currently works on flux synthesis of metal oxides and their photoelectrochemical properties.

ACKNOWLEDGMENTS

This dissertation has been possible because of the guidance and support of many individuals who through their assistance, mentoring and nurturing provided me with an excellent platform for doing my research. First and foremost, my deepest thanks to Professor Paul A. Maggard whose knowledge, encouragement and understanding made this dissertation achievable.

Thank you to my committee members, Prof. Chris Gorman, Prof. Mike H. Whangbo and Prof. David Shultz. I would like to thank Dr. Shultz for use of his SQUID and his group members Rob Schmidt and Geoff Lewis for their assistance with data collection.

I would like to thank my labmates Nacole King, Kathryn Wilberding, Jonathan Boltersdorf, Ian Sullivan, Lan Lou, Prangya Sahoo and former labmates Haisheng Lin and David Arney for making the lab a productive and enjoyable place.

Finally, I would to thank my family for all of their support and love.

TABLE OF CONTENTS

LIST OF TABLES	vi
LIST OF FIGURES	vii
PART 1: FLUX SYNTHESIS OF METAL OXIDE PARTICLES: PHOTOELECTROCHEMISTRY	1
CHAPTER 1. INTRODUCTION TO PHOTOELECTROCHEMISTRY.....	2
EXPERIMENTAL TECHNIQUES.....	7
REFERENCES	19
CHAPTER 2. Preparation and Photoelectrochemical Properties of p-type $\text{Cu}_5\text{Ta}_{11}\text{O}_{30}$ and $\text{Cu}_3\text{Ta}_7\text{O}_{19}$ Semiconducting Polycrystalline Films	22
EXPERIMENTAL.....	25
RESULTS AND DISCUSSION.....	28
CONCLUSIONS.....	36
SUPPORTING INFORMATION.....	53
REFERENCES	63
CHAPTER 3. The Effect of Oxidation on the Structural Properties of p-type CuNbO_3 , CuNb_3O_8 , $\text{Cu}_5\text{Ta}_{11}\text{O}_{30}$ and $\text{Cu}_3\text{Ta}_7\text{O}_{19}$	65
EXPERIMENTAL.....	66
RESULTS AND DISCUSSION.....	68
CONCLUSIONS.....	69
REFERENCES	87
PART 2: FLUX SYNTHESIS OF METAL OXIDE PARTICLES: INTERGRAIN TUNNELING MAGNETORESISTANCE.....	88
CHAPTER 4. INTRODUCTION TO MAGNETORESISTANCE.....	89
REFERENCES	102
CHAPTER 5. Rapid Molten-salt Syntheses of $\text{Sr}_2\text{FeReO}_6$, $\text{Ba}_2\text{FeReO}_6$ and $\text{Sr}_2\text{CrReO}_6$: Particle Sizes, B/B'-site Disorder, and Magnetic Properties	106
EXPERIMENTAL.....	109
RESULTS AND DISCUSSION.....	111
CONCLUSIONS.....	117
SUPPORTING INFORMATION.....	136
REFERENCES	145
CHAPTER 6. CONCLUSIONS.....	148
REFERENCES	154

LIST OF TABLES

Table 3.1	Lattice parameters for CuNbO_3 , CuNb_3O_8 , $\text{Cu}_5\text{Ta}_{11}\text{O}_{30}$ and $\text{Cu}_3\text{Ta}_7\text{O}_{19}$ calculated from the PXR.	70
Table 4.1	Magnetic and electronic properties, crystallographic parameters and the most common synthesis method employed for the half-metallic and related double-perovskites. Ferromagnetic is represented as FM, antiferromagnetic as AFM, paramagnetic as PM and canted ferromagnetism as CFM. Blank fields indicate an absence of a property defined in literature.	97
Table 5.1	Powder X-ray diffraction refinement results for lattice constants and B/B' site ordering in $\text{Sr}_2\text{FeReO}_6$ (Space group $I4/m$).	118
Table 5.2	Powder X-ray diffraction refinement results for lattice constants and B/B' site ordering in $\text{Ba}_2\text{FeReO}_6$ (Space group $Fm-3m$).	119
Table 5.3	Powder X-ray diffraction refinement results for lattice constants and B/B' site ordering in $\text{Sr}_2\text{CrReO}_6$ (Space group $Fm-3m$).	120
Table 5.4	Magnetic properties of the flux-prepared double-perovskites, including spontaneous and remanent magnetization (M_s and M_r respectively) and coercive field (H_c). Also shown is the fractional site occupancies of B/B' cations obtained by PXR refinements.	121
Table 5.S1	PXR refinement data for $\text{Ba}_2\text{FeReO}_6$	136
Table 5.S2	PXR refinement data for $\text{Sr}_2\text{FeReO}_6$	137
Table 5.S3	PXR refinement data for $\text{Sr}_2\text{CrReO}_6$	138
Table 5.S4	PXR refinement results including thermal parameters for $\text{Sr}_2\text{FeReO}_6$ synthesized using a 0.5:1 flux for 12 h, $\text{Ba}_2\text{FeReO}_6$ at a 1:1 flux for 6 h radiatively cooled and $\text{Sr}_2\text{CrReO}_6$ at a 1:1 flux for 6 h radiatively cooled.	139

LIST OF FIGURES

Figure 1.1	PEC cell configuration of (A) <i>n</i> -type semiconductor electrode with a Pt counter electrode and (B) a <i>p</i> -type semiconductor electrode with a Pt counter electrode.	13
Figure 1.2	Solar irradiance spectrum as a function of photon wavelength.	14
Figure 1.3	Schematic drawing of the band positions in an ideal semiconductor where the hydrogen and oxygen potentials lie within the conduction and valence bands of the material. These positions have been shown vs. NHE for a solution pH = 0.	15
Figure 1.4	The band positions of selected photocatalysts shown vs. NHE at pH = 1. Image adapted from reference 4.	16
Figure 1.5	Schematic energy diagram of the band positions for the solid solution $(\text{Cu}_x\text{Na}_{1-x})_2\text{Ta}_4\text{O}_{11}$ with increasing Cu(I) content, $\text{CuNb}_{13}\text{O}_{33}$, CuNbO_3 and CuNb_3O_8	17
Figure 1.6	Experimental photoelectrochemical measurement setup.	18
Figure 2.1	Powder X-ray diffraction data for (a) as-prepared $\text{Cu}_5\text{Ta}_{11}\text{O}_{30}$, (b) calculated pattern of $\text{Cu}_5\text{Ta}_{11}\text{O}_{30}$, and films of $\text{Cu}_5\text{Ta}_{11}\text{O}_{30}$, (c) annealed at 400 °C and oxidized at 250 °C, (d) annealed at 400 °C and oxidized at 350 °C, (e) annealed at 400 °C and oxidized at 450 °C, (f) annealed at 400 °C and oxidized at 550 °C, and (g) annealed at 500 °C and oxidized at 350 °C.	38
Figure 2.2	Powder X-ray diffraction data for (a) bulk $\text{Cu}_3\text{Ta}_7\text{O}_{19}$, (b) $\text{Cu}_3\text{Ta}_7\text{O}_{19}$ film annealed at 500 °C and (c) oxidized at 350 °C (d) calculated pattern of $\text{Cu}_3\text{Ta}_7\text{O}_{19}$	39
Figure 2.3	SEM images of a $\text{Cu}_5\text{Ta}_{11}\text{O}_{30}$ film (A) after annealing at 400 °C for 3 h, (B) a ~30 ° tilted cross-section view of film after oxidizing at 250 °C for 3 h, and (C and D) after annealing at 400 °C for 3 h before and after oxidizing at 350 °C, respectively.	40
Figure 2.4	SEM images of a $\text{Cu}_3\text{Ta}_7\text{O}_{19}$ film (A) after annealing at 500 °C for 3 h, (B) an ~30 ° tilted cross-section view of film, and (C and D) and after the chronoamperometry measurements, respectively.	41

Figure 2.5	Current-potential curves in aqueous 0.5 M Na ₂ SO ₄ solution (pH = 6.3) under chopped visible-light irradiation for Cu ₅ Ta ₁₁ O ₃₀ films annealed at 400 °C for 3 h and not oxidized or oxidized for 3 h at 250 °C, 350 °C (upper chart), and oxidized for 3 h at 450 °C, 550 °C (lower chart).	42
Figure 2.6	Current-potential curves in aqueous 0.5 M Na ₂ SO ₄ solution (pH = 6.3) under chopped visible-light irradiation for Cu ₅ Ta ₁₁ O ₃₀ films annealed at 400 °C and 500°C followed by oxidation at 350 °C for 3 h.	43
Figure 2.7	Current-potential curves in aqueous 0.5 Na ₂ SO ₄ solution (pH = 6.3) under chopped visible-light irradiation for Cu ₃ Ta ₇ O ₁₉ films annealed at 500 °C for 3 h and not oxidized or oxidized for 3 h at 350 °C and 550 °C.	44
Figure 2.8	Mott-Schottky plots for the (A) Cu ₃ Ta ₇ O ₁₉ and (B) Cu ₅ Ta ₁₁ O ₃₀ polycrystalline films annealed at 500 °C.	45
Figure 2.9	Incident-photon-to-current (IPCE) efficiencies (upper plot) for Cu ₅ Ta ₁₁ O ₃₀ films annealed at 400 °C or 500 °C and oxidized at 350 °C or 550 °C, and (lower plot) a Cu ₃ Ta ₇ O ₁₉ film annealed at 500 °C and no oxidation.	46
Figure 2.10	Current-potential curves for a Cu ₅ Ta ₁₁ O ₃₀ film annealed at 500 °C and oxidized at 350 °C in aqueous 0.5 M Na ₂ SO ₄ solution (pH = 6.3) under chopped frontside or backside visible-light illumination.	47
Figure 2.11	UV-Vis diffuse reflectance spectra for (upper plot) Cu ₅ Ta ₁₁ O ₃₀ films annealed at 400 °C and oxidized at various temperatures from 250 °C to 550 °C, and (lower plot) Cu ₃ Ta ₇ O ₁₉ films annealed at 500 °C and oxidized at 350 °C.	48
Figure 2.12	Cu 2p core-level spectra for Cu ₅ Ta ₁₁ O ₃₀ (upper plot) and Cu ₃ Ta ₇ O ₁₉ (lower plot) films annealed at 500 °C without oxidation (A), oxidized at 350 °C before (B) and after chronoamperometry (C).	49
Figure 2.13	Calculated band-structure <i>k</i> -space diagram for Cu ₃ Ta ₇ O ₁₉ , with arrows labeling the higher band-dispersion directions.	50

Figure 2.14	Calculated electron density for the lowest-energy conduction band states (A; reddish-orange density) and for the highest-energy valence band states (B; yellowish-green density), which is concentrated within the TaO ₇ layers and the TaO ₆ /Cu layers, respectively.	51
Figure 2.15	Cathodic photocurrents under visible-light irradiation of <i>p</i> -type Cu ₅ Ta ₁₁ O ₃₀ and Cu ₃ Ta ₇ O ₁₉ polycrystalline films, and a plot of the electron density for the lowest-energy conduction band states of a TaO ₇ layer that is found in each solid.	52
Figure 2.S1	Powder X-ray diffraction data for (a) Cu ₅ Ta ₁₁ O ₃₀ oxidized at 750 °C for 3 h, (b) calculated pattern of CuTa ₂ O ₆ , and (c) calculated pattern of Ta ₂ O ₅	53
Figure 2 S2	Thermogravimetric analyses (in air) versus time for Cu ₅ Ta ₁₁ O ₃₀ (upper) at 250 °C, 350 °C and 550 °C and for Cu ₃ Ta ₇ O ₁₉ (lower) at 350 °C and 550 °C.	54
Figure 2.S3	Powder x-ray diffraction data of (A) calculated Cu ₅ Ta ₁₁ O ₃₀ and (B) the Cu ₅ Ta ₁₁ O ₃₀ film after chronoamperometry (-0.4 V applied bias potential) for 1 h.	55
Figure 2.S4	O 1s core-level spectra for Cu ₅ Ta ₁₁ O ₃₀ (upper plot) and Cu ₃ Ta ₇ O ₁₉ (lower plot) films annealed at 500 °C without oxidation (A), oxidized at 350 °C before (B) and after chronoamperometry (C).	56
Figure 2 S.5	Ta 4f core-level spectra for Cu ₅ Ta ₁₁ O ₃₀ (upper plot) and Cu ₃ Ta ₇ O ₁₉ (lower plot) films annealed at 500 °C without oxidation (A), oxidized at 350 °C before (B) and after chronoamperometry (C).	57
Figure 2.S6	Chronoamperometry for the Cu ₅ Ta ₁₁ O ₃₀ sample analyzed by XPS.	58
Figure 2.S7	Chronoamperometry for the Cu ₃ Ta ₇ O ₁₉ sample analyzed by XPS.	59
Figure 2.S8	Electron-density plots from the calculated electronic structures of Cu ₅ Ta ₁₁ O ₃₀ for the lowest-energy states (blue electron density; unfilled) in the conduction band (on left) and the highest-energy states (red electron density; filled) in the valence band (on right). The “[“ brackets label the three different types of tantalate layers.	60

Figure 2.S9	Electron-density plots from the calculated electronic structures of $\text{Cu}_3\text{Ta}_7\text{O}_{19}$ for the lowest-energy states (blue electron density; unfilled) in the conduction band (A) and the highest-energy states (red electron density; filled) in the valence band (B) for just the Cu(I)/ TaO_6 layer. The “[“ brackets label the three different types of tantalate layers.	61
Figure 2.S10	Chronoamperometric measurements in aqueous 0.5 M Na_2SO_4 solution (pH = 6.3) for $\text{Cu}_5\text{Ta}_{11}\text{O}_{30}$ films annealed at 500 °C under vacuum and oxidized at 350 °C with zero applied voltage under visible-light illumination.	62
Figure 3.1	Current-potential curves in aqueous 0.5 M Na_2SO_4 solution (pH = 6.3) under chopped visible-light irradiation for a CuNbO_3 film annealed at 500 °C for 3 h and oxidized for 3 h at 350 °C.	71
Figure 3.2	Current-potential curves in aqueous 0.5 M Na_2SO_4 solution (pH = 6.3) under chopped visible-light irradiation for a CuNb_3O_8 film annealed at 500 °C for 3 h and oxidized for 3 h at 350 °C.	72
Figure 3.3	Current-potential curves in aqueous 0.5 M Na_2SO_4 solution (pH = 6.3) under chopped visible-light irradiation for a $\text{Cu}_5\text{Ta}_{11}\text{O}_{30}$ film annealed at 500 °C for 3 h and oxidized for 3 h at 350 °C.	73
Figure 3.4	Current-potential curves in aqueous 0.5 M Na_2SO_4 solution (pH = 6.3) under chopped visible-light irradiation for a $\text{Cu}_3\text{Ta}_7\text{O}_{30}$ film annealed at 500 °C for 3 h and oxidized for 3 h at 350 °C.	74
Figure 3.5	Crystal structures of $\text{Cu}_5\text{Ta}_{11}\text{O}_{30}$ (A) and $\text{Cu}_3\text{Ta}_7\text{O}_{19}$ (B).	75
Figure 3.6	Crystal structures of CuNbO_3 (A) and CuNb_3O_8 (B).	76
Figure 3.7	PXRD patterns for CuNbO_3 non-oxidized (A), oxidized at 250 °C (B), and 350 °C (C). Also shown is the calculated pattern of CuNbO_3	77
Figure 3.8	PXRD patterns for CuNb_3O_8 non-oxidized (A), oxidized at 250 °C (B), 350 °C (C) and 450 °C (D).	78
Figure 3.9	PXRD patterns for $\text{Cu}_5\text{Ta}_{11}\text{O}_{30}$ non-oxidized (A), oxidized at 250 °C (B), 350 °C (C) and 450 °C (D). Also shown is the calculated pattern of $\text{Cu}_5\text{Ta}_{11}\text{O}_{30}$ (E).	79

Figure 3.10	PXRD patterns for $\text{Cu}_3\text{Ta}_7\text{O}_{19}$ non-oxidized (A), oxidized at 250 °C (B), 350 °C (C) and 450 °C (D). Also shown is the calculated pattern of $\text{Cu}_3\text{Ta}_7\text{O}_{19}$ (E).....	80
Figure 3.11	UV-Vis diffuse reflectance spectra for (upper plot) CuNbO_3 with no oxidation and oxidized for 3 h at 250 °C and 350 °C, and (lower plot) CuNb_3O_8 with no oxidation and oxidized for 3 h at 250 °C, 350 °C and 450 °C.	81
Figure 3.12	UV-Vis diffuse reflectance spectra for (upper plot) $\text{Cu}_3\text{Ta}_7\text{O}_{19}$ with no oxidation and oxidized for 3 h at 250 °C, 350 °C and 450 °C and (lower plot) $\text{Cu}_5\text{Ta}_{11}\text{O}_{30}$ with no oxidation and oxidized for 3 h at 250 °C, 350 °C and 450 °C.	82
Figure 3.13	Unit cell lattice parameters versus oxidation temperature for CuNbO_3	83
Figure 3.14	Unit cell lattice parameters versus oxidation temperature for CuNb_3O_8	84
Figure 3.15	Unit cell lattice parameters for $\text{Cu}_5\text{Ta}_{11}\text{O}_{30}$	85
Figure 3.16	Unit cell lattice parameters for $\text{Cu}_3\text{Ta}_7\text{O}_{19}$	86
Figure 4.1	An illustration of ITMR where the set up on the right is in the absence of a magnetic field where tunneling is less favored. The set up on the left represents the tunneling of an electron that occurs in the presence of a magnetic field.	99
Figure 4.2	A representation of the spin density-of-states at the Fermi level for a normal metal, ferromagnetic metal and a half-metal.	100
Figure 4.3	Crystal structure of the B-site ordered $\text{A}_2\text{BB}'\text{O}_6$ double-perovskite with space group $Fm\bar{3}m$. BO_6 octahedra are shown in green, $\text{B}'\text{O}_6$ octahedra are shown in pink, A atoms are shown in blue and O atoms are shown in gray.	101
Figure 5.1	Crystal structure of $\text{Sr}_2\text{FeReO}_6$. FeO_6 polyhedra are shown in green, MO_6 octahedra are shown in pink, Sr atoms are shown in grey and oxygen atoms are shown in blue.....	122
Figure 5.2	Crystal structure of $\text{Sr}_2\text{CrReO}_6$. CrO_6 polyhedra are shown in light blue, ReO_6 octahedra are shown in pink, Sr atoms are shown in grey and oxygen atoms are shown in blue.....	123

Figure 5.3	Crystal structure of $\text{Ba}_2\text{FeReO}_6$. FeO_6 polyhedra are shown in green, ReO_6 octahedra are shown in pink, Ba atoms are shown in dark green and oxygen atoms are shown in blue.	124
Figure 5.4	PXRD Rietveld refinement results for $\text{Sr}_2\text{FeReO}_6$ synthesized using a 0.5:1 flux for 12 h. The observed profile is indicated by the circles and the calculated profile by the solid line. Bragg peak positions are indicated by vertical peaks. The difference diffractogram is shown at the bottom.	125
Figure 5.5	PXRD Rietveld refinement results for $\text{Ba}_2\text{FeReO}_6$ synthesized using a 1:1 flux and radiatively cooled. The observed profile is indicated by the circles and the calculated profile by the solid line. Bragg peak positions are indicated by vertical peaks. The difference diffractogram is shown at the bottom.	126
Figure 5.6	PXRD Rietveld refinement results for $\text{Sr}_2\text{CrReO}_6$ synthesized using a 1:1 flux radiatively cooled. The observed profile is indicated by the circles and the calculated profile by the solid line. Bragg peak positions are indicated by vertical peaks. The difference diffractogram is shown at the bottom.	127
Figure 5.7	SEM images for $\text{Sr}_2\text{FeReO}_6$ synthesized using a molten NaCl/KCl flux at (A) a 0.5:1 ratio for 3 h, (B) 0.5:1 ratio for 12 h, (C) a 1:1 ratio for 3 h, and (D) a 1:1 ratio for 12 h.	128
Figure 5.8	SEM images for $\text{Ba}_2\text{FeReO}_6$ synthesized using a molten NaCl/KCl flux at (A) a 1:1 ratio for 6 h, (B) 3:1 ratio for 6 h, (C) a 3:1 ratio for 6 h and quenching; $\text{Sr}_2\text{CrReO}_6$ using (D) a 1:1 ratio for 6 h, (E) a 1:1 ratio and slow cooling over 24 h and (F) a 3:1 ratio for 6 h and quenching. Samples in A, B and D were radiatively cooled.	129
Figure 5.9	M(H) curves for $\text{Sr}_2\text{FeReO}_6$ synthesized using a molten NaCl/KCl flux at 750°C at a 0.5:1 and 1:1 ratio for both 3 h and 12 h.	130
Figure 5.10	M(H) curves for $\text{Ba}_2\text{FeReO}_6$ synthesized using a molten NaCl/KCl flux at 800°C at a 1:1 flux ratio for 6 h and 3:1 flux ratio for 6 h radiatively cooling, a 3:1 flux ratio for 6 h rapidly quenched, and a 1:1 flux ratio for 6 h slow cooled over 24 h.	131

Figure 5.11	M(H) curves for $\text{Sr}_2\text{CrReO}_6$ synthesized using a molten NaCl/KCl flux at 800 °C at a 1:1 flux ratio for 6 h and 3:1 flux ratio for 6 h radiatively cooled, a 3:1 flux ratio for 3 h and rapidly quenched, and a 1:1 flux ratio for 6 h and slowly cooled over 2 days.....	132
Figure 5.12	Temperature dependence of the resistivity for $\text{Sr}_2\text{FeReO}_6$ synthesized by the solid state method and at a 1:1 flux for 3 h; $\text{Ba}_2\text{FeReO}_6$ at a 1:1 flux for 6 h and radiatively cooled and $\text{Sr}_2\text{CrReO}_6$ at a 1:1 flux for 6 h and radiatively cooled.	133
Figure 5.13	Temperature and magnetic-field dependence of the resistivity for polycrystalline $\text{Sr}_2\text{FeReO}_6$ pellets prepared via the solid-state and flux-synthetic routes (1:1 molar ratio, 3 h).....	134
Figure 5.14	An SEM image of $\text{Sr}_2\text{FeReO}_6$ synthesized in high-purity in an NaCl/KCl flux at 750 °C for 3 h with homogeneous particles ranging from ~50 – 100 nm in size. Temperature and magnetic-field dependence of the electrical resistivity for polycrystalline $\text{Sr}_2\text{FeReO}_6$ pellets prepared via the solid-state and flux-synthetic routes (1:1 molar ratio, 3 h).....	135
Figure 5.S1	PXRD Rietveld refinement results for $\text{Sr}_2\text{CrReO}_6$ synthesized using a molten NaCl/KCl flux at (A) a 1:1 flux for 6 h and slow cooling over 2 days, (B) a 3:1 flux for 6 h and rapidly quenched and (C) a 3:1 flux for 6 h radiatively cooled. The observed profile is indicated by the circles and the calculated profile by the solid line. Bragg peak positions are indicated by vertical peaks. The difference diffractogram is shown at the bottom.....	140
Figure 5.S2	PXRD Rietveld refinement results for $\text{Sr}_2\text{FeReO}_6$ synthesized by (A) solid state method; using a molten NaCl/ KCl flux at (B) a 1:1 flux for 12 h, (C) a 1:1 flux for 3 h and (D) a 0.5:1 flux for 3 h. The observed profile is indicated by the circles and the calculated profile by the solid line. Bragg peak positions are indicated by vertical peaks. The difference diffractogram is shown at the bottom.....	141
Figure 5.S3	PXRD Rietveld refinement results for $\text{Ba}_2\text{FeReO}_6$ synthesized by using a molten NaCl/KCl flux at (A) a 3:1 flux for 6 h and slow cooling over 24 h, (B) a 3:1 flux for 6 h and rapidly quenched and (C) a 3:1 flux for 6 h radiatively cooled. The observed profile is indicated by the circles and the calculated profile by the solid line. Bragg peak positions are indicated by vertical peaks. The difference diffractogram is shown at the bottom.....	142

Figure 5.S4	Temperature-dependent resistivity measurements at 0 kG and 3 kG for $\text{Sr}_2\text{CrReO}_6$ particles prepared by a NaCl/KCl flux synthesis at 800 °C for 6 h using a 1:1 flux:product molar ratio radiatively cooled.....	143
Figure 5.S5	Temperature-dependent resistivity measurements at 0 kG and 3 kG for $\text{Ba}_2\text{FeReO}_6$ particles prepared by a NaCl/KCl flux synthesis at 800 °C for 6 h using a 1:1 flux:product molar ratio radiatively cooled.....	144
Figure 6.1	The valence and conduction band positions for $\text{Cu}_5\text{Ta}_{11}\text{O}_{30}$ and $\text{Cu}_3\text{Ta}_7\text{O}_{19}$ determined from their flat-band potentials vs. RHE (pH 6.3) with respect to the water oxidation and reduction potentials.	152
Figure 6.2	Temperature and magnetic-field dependence of the resistivity for a polycrystalline $\text{Sr}_2\text{FeReO}_6$ pellet prepared by flux synthesis. Also shown is an illustration of ITMR where the set up above is in the absence of a magnetic field where tunneling does not occur as readily. The set up on the left represents the tunneling of an electron that occurs in the presence of a magnetic field.	153

**PART 1: FLUX SYNTHESIS OF METAL OXIDE PARTICLES:
PHOTOELECTROCHEMISTRY**

CHAPTER 1

INTRODUCTION TO PHOTOELECTROCHEMISTRY

Solar hydrogen generation through photoelectrochemical water splitting using metal-oxides as photoelectrode materials has attracted considerable interest in the field of renewable energy. With the world energy consumption estimated to double by 2050 and the diminishing of our energy reserves, increased research efforts have focused on the development of a sustainable energy source to supply our growing energy needs.¹ While estimations of the fossil fuel reserves that comprise of 85% of our current energy consumption range from 40-80 years for oil, 60-160 years of natural gas and 150-400 years for coal, the effects of depleting reserves will be felt far sooner as they become harder to recover.^{2,3} The generation of greenhouse gasses from the combustion of fuels and their impact on the environment also poses a more immediate concern.⁴ Therefore an investigation into clean sustainable energy source alternatives to fossil fuels with the potential to address our growing energy demands is needed. The solar driven photoelectrochemical production hydrogen from water using metal-oxide based photoelectrodes has been gaining considerable research over the past few decades as a potentially clean renewable energy source alternative to the current combustion of fossil fuels. A photoelectrochemical cell for the production of hydrogen from water was first reported in 1972 by Fujishima and Honda using *n*-TiO₂ as a photoelectrode under ultra-violet

illumination and a 0.5 V applied potential.⁵ Since this discovery, many types of materials have been explored as potential photoelectrode materials for water splitting with the most promising being metal-oxides due to their relatively higher inherent stability against photocorrosion compared to non-oxide semiconductors.

The basic photoelectrochemical cell (PEC) setup consists of an anode where water oxidation occurs and a cathode where water reduction occurs in which one of these consists of a photoactive semiconductor and the other of a metal such as Pt serving as a counter electrode submersed in an aqueous electrolyte. Shown in Figure 1.1 are the PEC configurations for *n*-type and *p*-type photoactive semiconductor electrodes. If the photoactive material is an *n*-type material such as *n*-TiO₂, water splitting is initiated when the photoactive electrode (photoanode) is irradiated with photons equal to or greater in energy than the bandgap of the material. Upon illumination, electrons from the valence band are excited to the conduction band and create electron-hole pairs. The electrons and holes are separated by an electric field inside the semiconductor (space charge layer) and the electrons travel to the conducting contact via an external connection to the Pt counter electrode (cathode) where they can reduce water to form H₂. The holes are swept towards the semiconductor electrolyte surface and can oxidize water to form O₂. If the photoactive material is *p*-type, it acts as the photocathode and water is preferentially reduced on the semiconductor surface and water is oxidized at the counter electrode. The overall water splitting reaction is $\text{H}_2\text{O} + 2h\nu \rightarrow \text{H}_2 + 1/2\text{O}_2$ ($h\nu$ = photon energy) and can be driven by light with a wavelength ≤ 1008 nm (1.23 eV) (Figure 1.2). In some cases, the photovoltage between electrodes is less than 1.23 eV and an external bias can be applied.⁶ With the

majority of the solar spectrum composed of visible-light, visible-light absorption is a key requirement in a semiconductor for water splitting.

In an ideal semiconductor for overall water splitting, the potential of the conduction band edge should be more negative than the H^+/H_2 redox potential and the valence band edge should be more positive than the $\text{O}_2/\text{H}_2\text{O}$ oxidation potential as shown in Figure 1.3.⁷ In the case of *n*-type TiO_2 and many other metal oxides, the conduction and valence bands suitably straddle the water oxidation and reduction potentials, but their bandgap sizes are too large and restricts them to only ultraviolet-light absorption. A relatively smaller number of *n*-type metal oxides that absorb at visible-light energies have been explored for use as water oxidation catalysts, such as $\alpha\text{-Fe}_2\text{O}_3$, WO_3 , and BiVO_4 .⁸⁻¹⁰ However, their decreases in bandgap size are generally found to originate from a downshift in the conduction band energy, and thus making most all of them unsuitable for use as *p*-type photoelectrodes for the reduction of water. The band positions with respect to the water oxidation and reduction potentials for selected metal-oxide and non-oxide photocatalysts are shown in Figure 1.4.

Narrow-bandgap non-oxide semiconductors such as GaN and CdS have been explored as *p*-type photoelectrode materials, however they lack the stability of metal-oxides and are readily deactivated through photocorrosion and self-oxidation.^{11,12} Just a few examples of *p*-type semiconducting oxides that function as photocathodes under visible-light irradiation have been discovered so far, including Cu_2O , CaFe_2O_4 , and metal-ion doped Fe_2O_3 .¹³⁻¹⁶ Thus a primary critical direction in this area is the identification of new *p*-type photoelectrode metal oxides capable of visible-light absorption.

Recent research efforts in the Maggard group have focused on achieving smaller bandgap sizes via the use of Nb(V) or Ta(V) cations (empty d^0 -orbitals) that form the conduction band states in early transition-metal oxides, together with a Cu(I) cation (filled d^{10} -orbitals) that can form higher energy valence-band states.¹⁷⁻²⁰ For example, the isoelectronic substitution of Cu(I) for the Na cation in the NaNbO_3 photocatalyst decreases its bandgap size from ~ 3.4 eV to ~ 2.0 eV via the creation of a new higher-energy valence band consisting of the filled Cu d^{10} orbitals, as found in CuNbO_3 .^{17,21} For the solid solution $(\text{Cu}_x\text{Na}_{1-x})_2\text{Ta}_4\text{O}_{11}$, increasing the Cu(I) content from $x = 0.05$ to $x = 0.77$ was found to decrease the bandgap from 3.2 eV to 2.7 eV, as shown in Figure 1.5.²² Thus my research efforts in this field extend the use Cu(I)/Ta(V)-based compounds as potential photoelectrodes for the photoelectrochemical splitting of water.

In addition to the appropriate location of the conduction and valence band positions, an ideal photoelectrode material must also be capable of efficient charge transport.¹ Poor mobility of charge carriers would prevent the effective transport of charges from the bulk of the material to the surface, and thus decreasing its photocatalytic efficiency. Decreased charge mobility in metal-oxides is often caused by the presence of defects in the material that can serve as recombination centers for the photogenerated electrons or holes, and preventing efficient charge transport to the electrolyte semiconductor surface. Previous studies on the photocurrent response of $\alpha\text{-Fe}_2\text{O}_3$ photoelectrodes have been shown to be highly dependent on the preparation conditions.²³ In general, the observed photocurrent in $\alpha\text{-Fe}_2\text{O}_3$ photoelectrodes was found to increase under synthesis conditions that improved the crystallinity of the material.²³ Therefore, it is critical to employ a preparation method that

allows for the preparation of highly crystalline products. Mixed-metal oxides are typically prepared using solid-state techniques in which products of high purity and crystallinity are often hard to obtain. An alternative approach to the synthesis of these materials is to use a molten-flux synthetic method, which employs the use of a molten-salt as a solvent media and enables the formation of highly crystalline products. Previous research efforts in the Maggard group have explored the use of flux-synthesis for the preparation of photocatalyst materials in particulate photocatalytic systems, and which have shown increased catalytic rates in comparison to solid-state preparation methods.²² However, the use of flux-synthesis of the preparation of photoelectrochemical electrodes has never been explored.

The major research efforts of my work described in part 1 of this document is the identification of two new *p*-type photoelectrode, i.e. $\text{Cu}_5\text{Ta}_{11}\text{O}_{30}$ and $\text{Cu}_3\text{Ta}_7\text{O}_{19}$, capable of hydrogen production under visible-light. Polycrystalline films of each were prepared starting from their flux-synthesis by and tested for photoelectrochemical water splitting. Oxidation of these films was found to enhance the photocathodic response and the effects of oxidation and annealing temperatures were probed for each system. Films were characterized using Powder X-ray Diffraction, UV-Visible Spectroscopy, Scanning Electron Microscopy and Thermogravimetric analyses. The surfaces of the films before and after photoelectrochemical testing were also probed using X-ray Photoelectron Spectroscopy to investigate possible photocorrosion at the film's surfaces. The flat-band potentials of each were determined using a Mott-Schottky analysis and used to calculate the valence and conduction band positions. Through these studies we seek to provide a better understanding

of these materials as *p*-type photoelectrodes and to provide a basis for identifying and investigating other potential *p*-type metal oxides.

EXPERIMENTAL TECHNIQUES

Molten-Salt Flux Synthesis

Flux syntheses were performed by first combining mixtures of analytical reagent grade reactants inside a glovebox under a nitrogen or argon atmosphere. The reactants were ground together in a mortar and pestle for 20 minutes prior to and after the addition of the desired flux. The resulting mixtures were loaded into fused silica ampules and flame sealed on a vacuum line. The reaction ampules were heated in a ceramic tube furnace. The heating profiles and molar ratios are described further in each chapter. The flux was removed from the resulting products by washing. More details are provided in each chapter.

Polycrystalline Film Preparation

Polycrystalline films were prepared on fluorine-doped tin oxide glass slides (FTO) (TEC-15 from Pilkington Glass Inc.). Prior to sample deposition, the FTO slides were cleaned by sonication in deionized water, acetone and ethanol for 20 minutes each for two cycles. A ~ 2 cm² area was then masked off on each slide using two layers of Scotch tape. Approximately 30 mg of sample was ground in ethanol as a dispersant and spread over the slide using the doctor-blade technique. The films were then dried at room temperature and

the tape was removed. All films were annealed in a ceramic processing furnace under vacuum at ~30 milibar. Further details are given in each chapter.

Powder X-ray Diffraction

Powder X-ray diffraction (PXRD) patterns of all synthesized products were collected on an INEL diffractometer using Cu K α_1 ($\lambda = 1.54056 \text{ \AA}$) radiation from a sealed tube X-ray generator (35 kV, 30 mA) in transmission mode using a curved position detector (CPS120). Samples were prepared by placing approximately 40 mg of dry sample onto a piece of Scotch tape adhered to the sample holder. The sample was spread across the tape as a uniform smooth layer and a second piece of tape was then placed over the tape containing the sample. The sample holder was placed in the rotating mount located between the direct beam of the incident X-rays and the detector. Data were collected for approximately 1 hour each. The resulting patterns were analyzed using Winplotr²⁴ and compared to calculated patterns from the ICSD and the ICDD databases using the programs FindIt and Match!.^{25,26}

High-resolution powder X-ray diffraction data sets used in Rietveld refinements and unit cell calculations were collected at room temperature on a Rigaku R-Axis Spider equipped with a curved image plate detector and Cu K α_1 radiation from a sealed-tube X-ray source. Samples were loaded into 0.1-0.3 mm borosilicate capillaries and data was collected for 2 h. The resulting 2-D images were integrated to produce conventional 2 θ intensity patterns using 2DP.²⁵ Refinements were performed by the Rietveld method using the WPF Refinement option in Jade 9.²⁸

UV-Visible Diffuse Reflectance

UV-Visible diffuse Reflectance Spectra (DRS) were collected on a Shimadzu UV-3600 equipped with an integrating sphere. Approximately 30 mg of sample was pressed onto a BaSO₄ powder holder and placed along the external window. Pressed BaSO₄ powder was used as a reference and the data were plotted as the remission function $F(R_{\infty}) = (1 - R_{\infty})^2 / (2R_{\infty})$, where R is diffuse reflectance based on the Kubelka-Munk theory of diffuse reflectance.²⁹ The bandgap size (E_g) was estimated using the formula E_g (eV) = (1240/ λ_g (nm)) where λ_g is extrapolated from the linear rise in the absorption curve.

Thermogravimetric Analyses (TGA)

Thermogravimetric analyses were carried out on a TA Instruments Q50. A weighed amount (~20 mg) of each sample was loaded onto Pt pans, equilibrated and tarred at room temperature in open air. Samples were stepped to temperatures of 250 °C, 350 °C, or 550 °C at a heating rate of 16.0 °C/min and held there for 3 h.

Scanning Electron Microscopy

Scanning electron microscopy (SEM) on a JEOL 6400 was performed in order to examine the particle size distribution and morphology of the reaction products. Bulk samples were prepared by placing approximately 10 mg of dry sample on a piece of double sided coated carbon tape adhered to an aluminum specimen stub. A fast stream of nitrogen gas was then applied over the sample to ensure ample separation of the particles for a size distribution analysis. Polycrystalline films were characterized on FTO glass as prepared. All

samples were then sputter coated with a thin layer of gold colloid particles (~40) to increase the conductivity of the sample and to maximize the spatial resolution. The microstructure and particle size distribution were imaged at magnifications ranging from 10,000-100000 \times . The film thicknesses were measured at a tilted 30°, and the correction applied as thickness = observed thickness \times (1 / cos(30°)).

X-ray Photoelectron Spectroscopy

X-ray photoelectron spectra were collected on a PHOIBIS 150 equipped with a hemispherical analyzer using monochromatized Mg (K_{α} = 1,254 eV) radiation. A chamber base pressure of approximately 10^{-10} mbar was achieved under ultrahigh vacuum. The binding energies were internally calibrated to the C 1s peak at 285.0 eV.

Semiconducting Quantum Interference Device

Magnetization measurements were collected on a Quantum Design MPMS XL SQUID magnetometer with a maximum field capability of 7 T and a temperature range from 2-400 K. A typical sample was prepared by placing a weighed amount (~20 mg) of dry homogeneous sample into a diamagnetic gelatin capsule. The gelatin capsule was inserted into a diamagnetic straw and secured with additional pieces of straw and polyimide tape. Each sample was corrected for the diamagnetism of the atomic cores using Pascal's constants.³⁰ The diamagnetism of the sample holder was also corrected using a background scan subtraction. Magnetization measurements were recorded from 5 K to 400 K in a field

that varied from 1-3 T depending on the sample. Magnetization field hysteresis loops were collected from -7 T to 7 T at 5 K. Further details are provided in each chapter.

Resistivity Measurements

Electrical resistivity measurements were collected using an MMR Hall and Van Der Pauw measurement system with a variable temperature hall Dewar equipped with a four probe setup and micro-miniature refrigeration unit. Samples were prepared by pressing approximately 250 mg of dry sample into a pellet with a 10 mm diameter. Pellets were mounted on the stage of a variable temperature micro-miniature refrigeration unit using a small amount of Dow Corning 360 silicone heat sink. The four probes installed in the sample Dewar were then lowered onto the sample and the Dewar was sealed and vacuumed down to approximately 10 millitorr. During magnetoresistance type measurements, the Dewar was placed between the two poles of a GMW 5403 electromagnet.

Photoelectrochemical Measurements

All photoelectrochemical measurements were performed in a custom-fabricated Teflon cell with the prepared polycrystalline film as the working electrode, Pt as the counter electrode and a standard calomel saturated KCl electrode as the reference electrode. A 0.5 M Na_2SO_4 aqueous solution, adjusted to $\text{pH} = 6.3$ using dilute H_2SO_4 (aq), was used as the electrolyte and the cell was purged with argon gas 30 minutes prior to and during all measurements. An electrochemical analyzer (Princeton Applied Research, PARSTAT 2263) with PowerSuite software was used to measure photocurrent and to carry out

chronoamperometry experiments. Films were irradiated from the backside using a 400 W Xe arc lamp equipped with a long-pass cutoff filter (>420 nm) and band-pass filters as appropriate. Mott-Schottky measurements were obtained using the AC electrochemical impedance method, with an AC amplitude of 5 mV at an applied frequency of 12 kHz. The experimental setup used for all photoelectrochemical measurements is shown in Figure 1.6.

Incident-photon-to-current conversion efficiency (IPCE) measurements were carried out using band-pass filters of four different wavelengths (352, 451, 522, and 603 nm). The number of photons of monochromatic light reaching the electrode surface was measured at each wavelength using a Si photodiode. The % IPCE is defined as $[(1239.8 \times \text{photocurrent density [mA/cm}^2]) / (\text{wavelength [nm]} \times \text{photon flux [mW/cm}^2])] \times 100$.

Dissertation Organization

This dissertation has been organized in the form of papers either recently published or in preparation to be published. They are divided into two major sections: 1. Flux Synthesis of Metal-Oxide Particles: Photoelectrochemistry (Chapters 1-3) and 2. Flux Synthesis of Metal Oxide-Particles: Intergrain Tunneling Magnetoresistance. (Chapters 4-5).

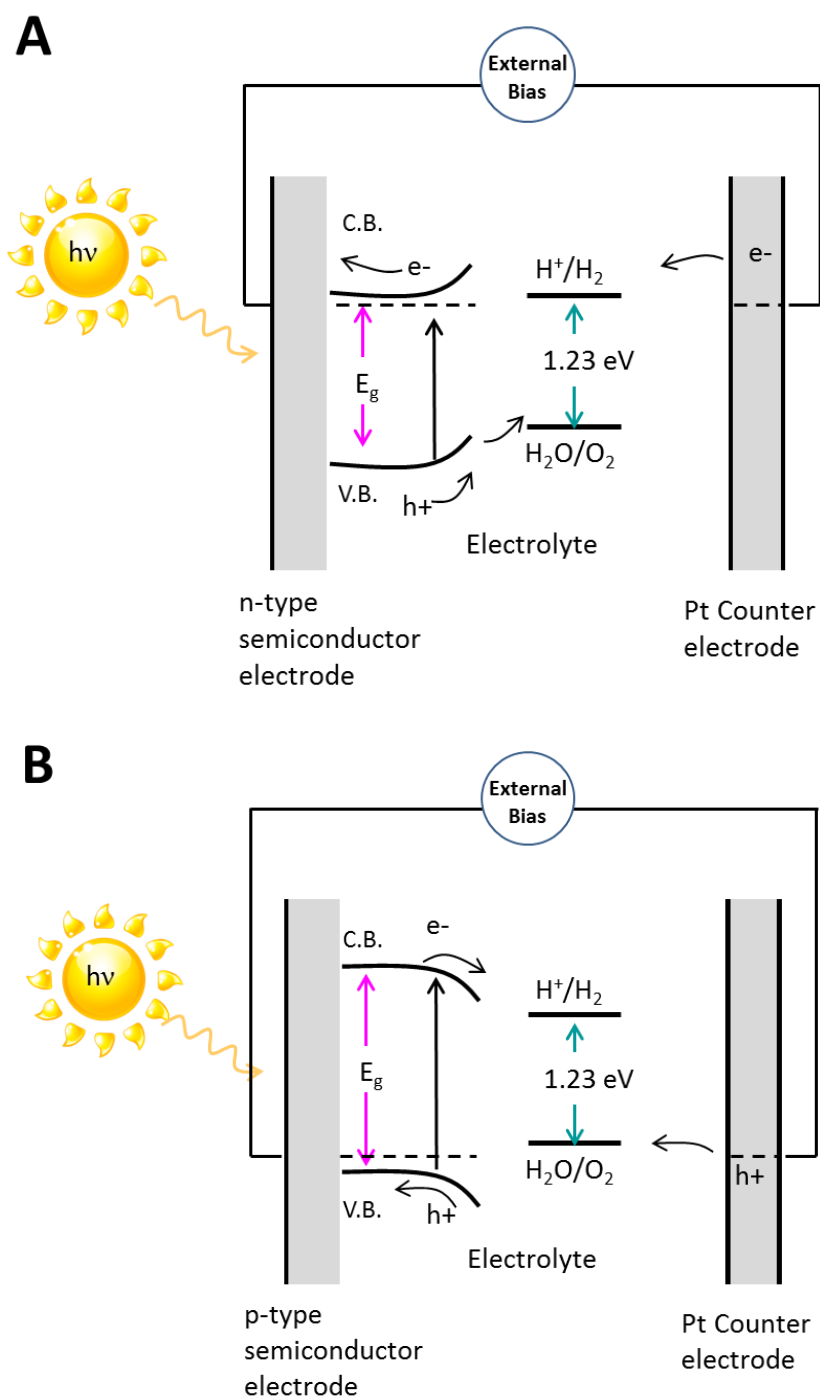


Figure 1.1. PEC cell configuration of (A) *n*-type semiconductor electrode with a Pt counter electrode and (B) a *p*-type semiconductor electrode with a Pt counter electrode.

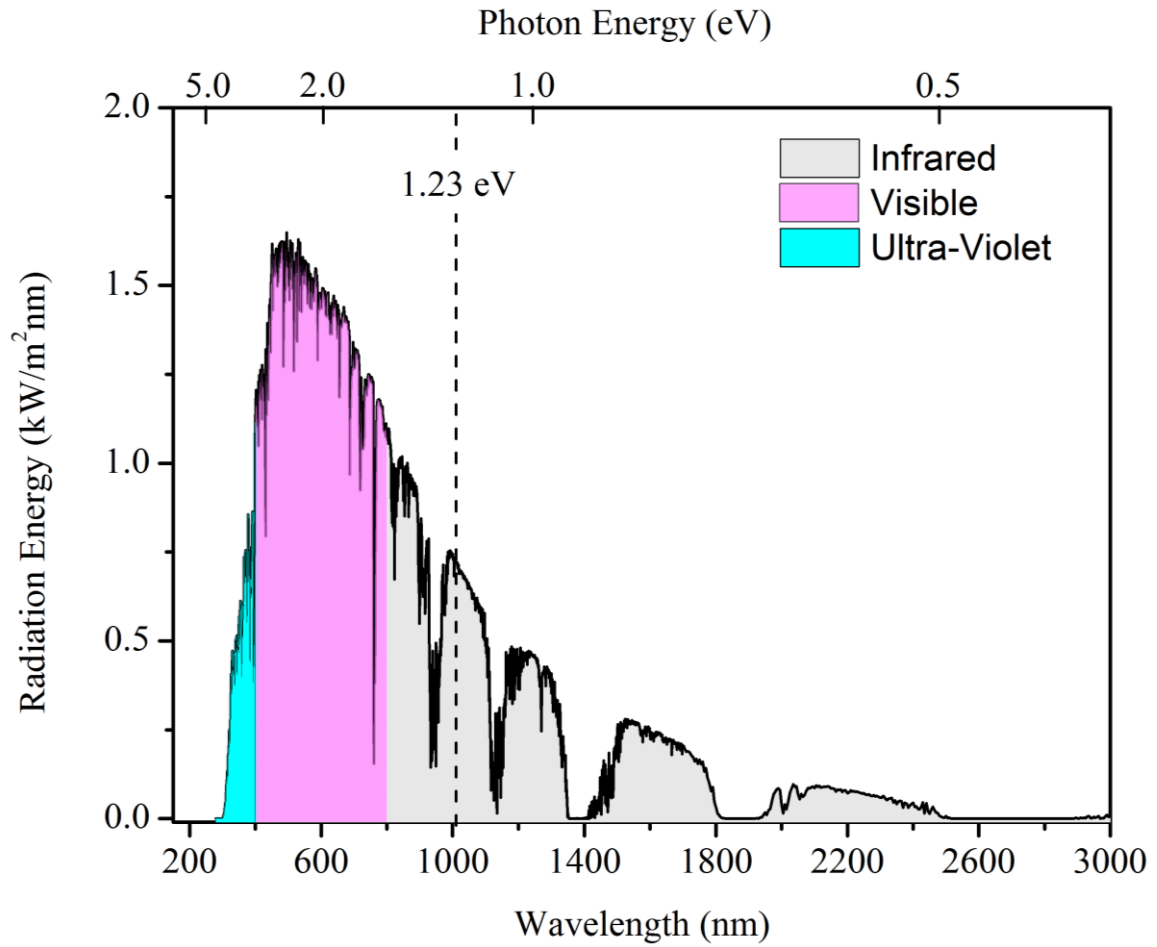


Figure 1.2. Solar irradiance spectrum as a function of photon wavelength.³¹

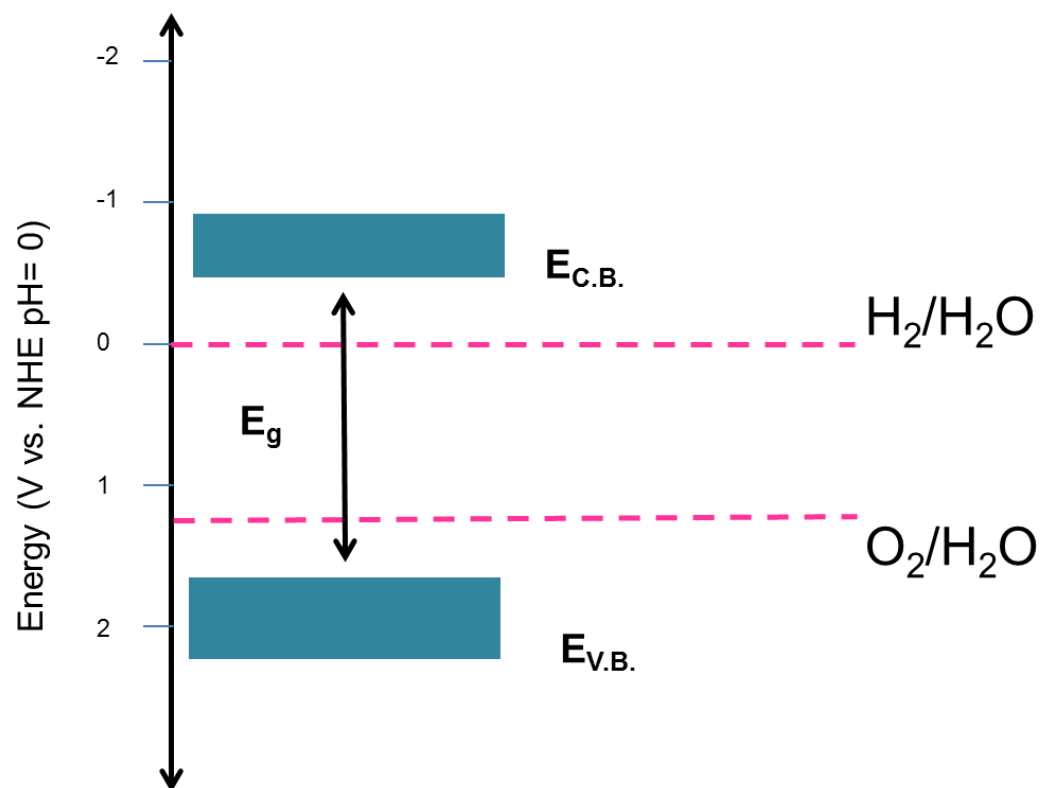


Figure 1.3. Schematic energy diagram of an ideal water-splitting photocatalyst where the hydrogen and oxygen potentials lie outside the conduction and valence bands of the material. These positions have been shown vs. NHE for a solution pH = 0.

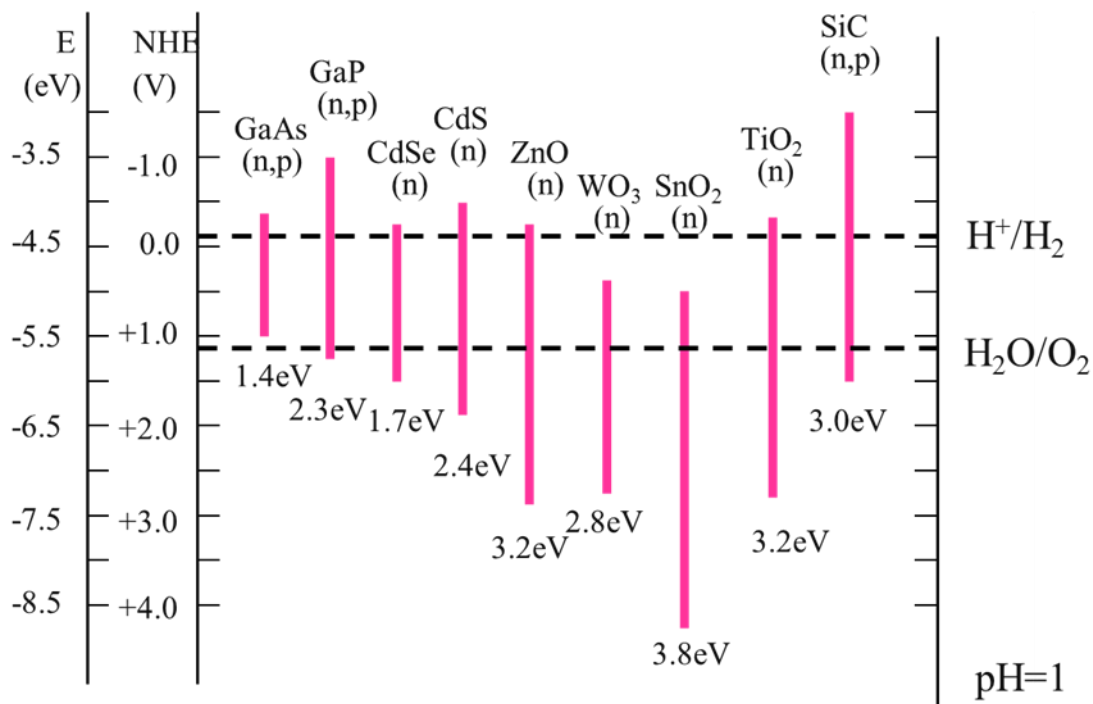


Figure 1.4. Previously reported band positions of selected photocatalysts shown vs. NHE at pH = 1. Image has been adapted from reference 4.

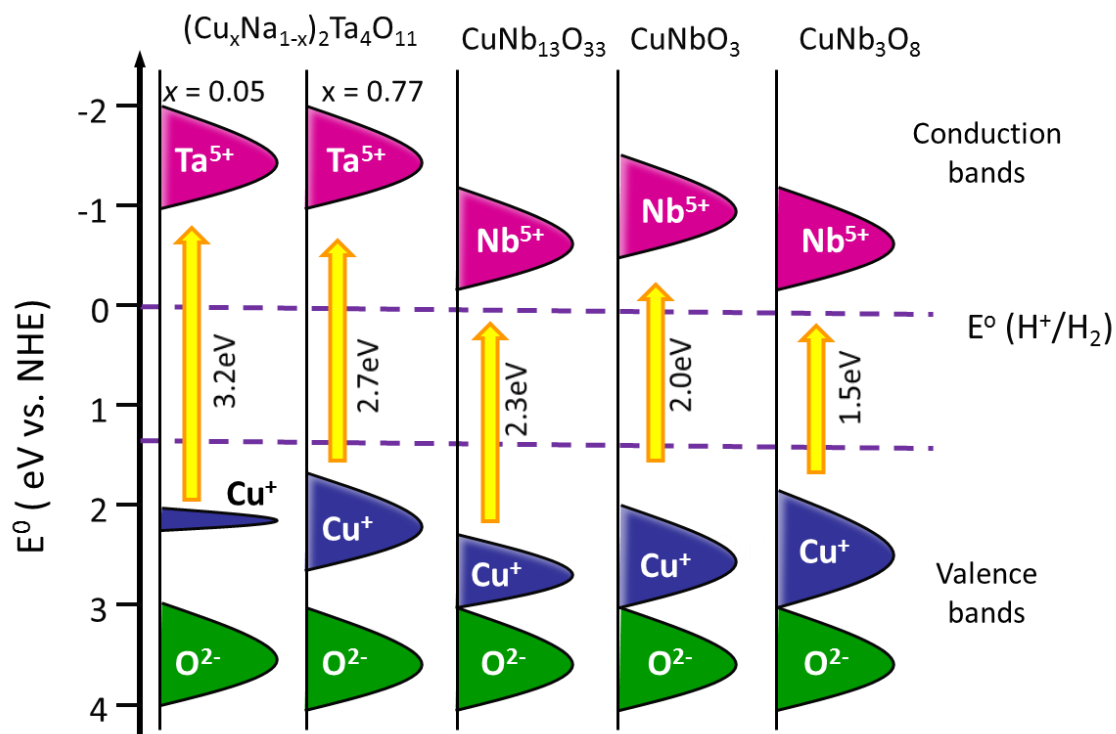


Figure 1.5. Schematic energy diagram of the band positions for the solid solution $(\text{Cu}_x\text{Na}_{1-x})_2\text{Ta}_4\text{O}_{11}$ with increasing Cu(I) content, $\text{CuNb}_{13}\text{O}_{33}$, CuNbO_3 and CuNb_3O_8 .

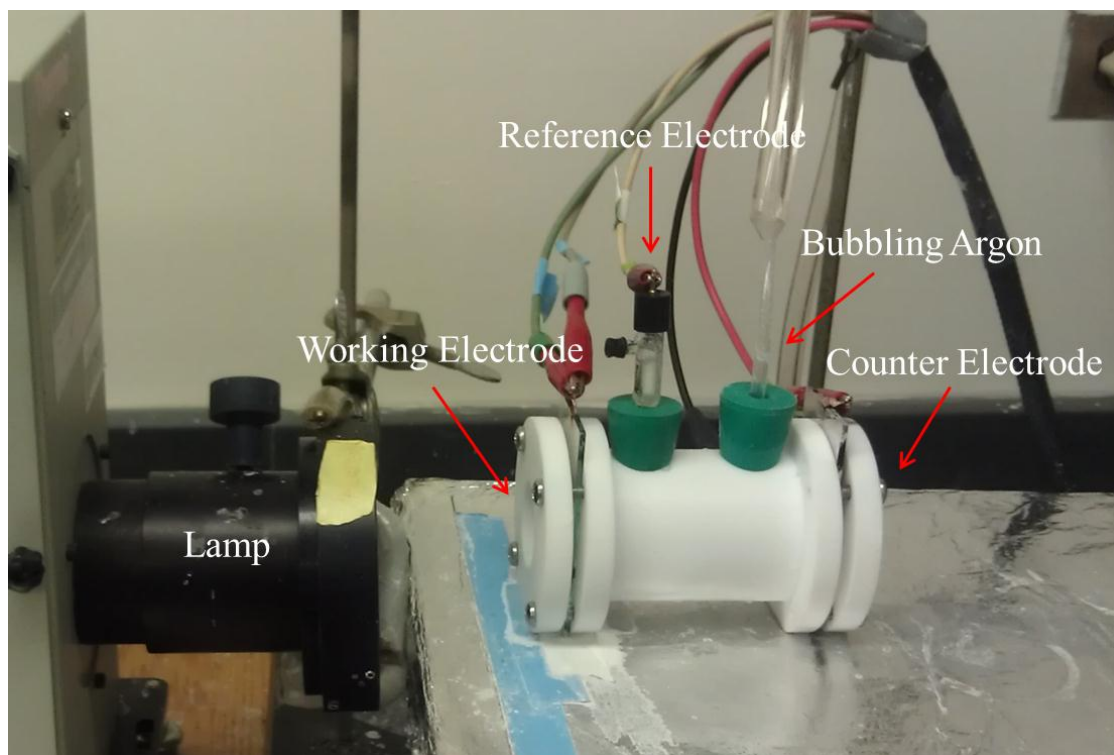


Figure 1.6. Experimental photoelectrochemical measurement setup.

REFERENCES

- (1) Nocera, D. G. *Inorg. Chem.* **2009**, *48*.
- (2) Van de Krol, R.; Gratzel, M. *Photoelectrochemical Hydrogen Production*; Springer: Cambridge, Massachusetts, **2012**; Vol. 1.
- (3) Lewis, N. S.; Nocera, D. G. *Basic Research Needs for Solar Energy Utilization: report of the Basic Energy Sciences Workshop on Solar Energy Utilization*, **2005**.
- (4) Gratzel, M. *Nature* **2001**, *414*, 338.
- (5) Fujishima, A.; Honda, K. *Nature* **1972**, 238.
- (6) Grimes, C. A.; Varghese, O. K.; Ranjan, S. *Light, Water, Hydrogen; The Solar Generation of Hydrogen by Water*; Springer: New York NY, **2008**.
- (7) Chen, Z.; Jaramillo, T. F.; Deutsch, T. G.; Kleiman-Shwarsctein, A.; Forman, A. J.; Gaillard, N.; Garland, R.; Takanabe, K.; Heske, C.; Sunkara, M.; McFarland, E. W.; Domen, K.; Miller, E. L.; Turner, J. A.; Dinh, H. *J. Mater. Res* **2010**, *25*, 3.
- (8) Kennedy, J. H.; Frese, K. W. *J. Electrochem. Soc.* **1978**, *125*, 709.
- (9) Sayama, K.; Nomura, A.; Zou, Z.; Aby, R.; Abe, Y.; Arakawa, H. *Chem. Commun.* **2003**, 2908.
- (10) Hodes, G.; Cahen, D.; Manassen, J. *Nature* **1976**, *260*, 312.
- (11) Mills, A.; Le Hunte, S. *J. of Photochem. Photobiol.* **1997**, *108*, 1.
- (12) Abe, R. *Photochemistry Reviews* **2010**, *11*, 179.
- (13) Shintaro, I.; Yamada, K.; Matsunaga, T.; Hagiwara, H.; Matsumoto, Y.; Ishihara, T. *J. Am. Chem. Soc.* **2010**, *132*, 17343.

- (14) Hara, M.; Konda, T.; Komoda, M.; Ikeda, S.; Shinohara, K.; Tanaka, A.; Konda, J. N.; Domen, K. *Chem. Commun.* **1998**.
- (15) Ingler, W. B.; Baltrus, J. P.; Khan, S. U. M. *J. Am. Chem. Soc.* **2004**, *126*, 10238.
- (16) Leygraf, C.; Hendewerk, M.; Somorjal, G. A. *J. Phys. Chem.* **1982**, *86*, 4484.
- (17) Joshi, U.; Palasyuk, A. M.; Maggard, P. A. *J. Phys. Chem. C* **2011**, *115*, 13534.
- (18) Palasyuk, O.; Palasyuk, A. M.; Maggard, P. A. *J. Solid State Chem.* **2010**, *183*, 814.
- (19) Palasyuk, O.; Palasyuk, A.; Maggard, P. A. *Inorg. Chem.* **2010**, *49*, 10571.
- (20) Joshi, U. A.; Palasyuk, A.; Arney, D.; Maggard, P. A. *J. Phys. Chem. Lett.* **2010**, *1*, 2719.
- (21) Li, G.; T., K.; Wang; D.; Zou, Z.; Ye, J. *J. Phys. Chem. Solids* **2008**, *69*, 2487.
- (22) Joshi, U.A., Palasyuk, A., Arney, D., Maggard, P.A. *J. Phys. Chem. Lett.* **2010**, 2719.
- (23) Alexander, B.D., Kulesza, P.J., Rutkowska, I., Solarska, R., Agustynski, J. *J. Mater. Chem.* **2008**, 2298.
- (24) Rodriguez-Carvajal, J., Roisnel, T., *FullProf and WinPLOTR*; Commission for Powder Diffraction, International Union for Crystallography: Renes France, **2004**.
- (25) *Inorganic Crystal Structure Database*; 1.4.4 ed. Fachinformationszentrum Karlsruhe, Germany, **2008**.
- (26) Brandenburg, K., Putz, H.; Crystal Impact: Bonn, Germany, **2007**.
- (27) Rigaku **2010**.
- (28) MDI In Jade 9; Materials Data Incorporated: **2009**.
- (29) Kubelka, P.; Munk, F. *Z. Tech. Physik* **1931**, *12*, 593.
- (30) Bain, G. A.; Berry, J. F. *J. Chem. Ed.* **2008**, *85*, 532.

- (31) NREL 2009. AM 1.5 Global solar spectrum derived from SMARTS v.2.9.2; <http://rredc.nrel.gov/solar/spectra/am1.5/>.

CHAPTER 2

Preparation and Photoelectrochemical Properties of *p*-type $\text{Cu}_5\text{Ta}_{11}\text{O}_{30}$ and $\text{Cu}_3\text{Ta}_7\text{O}_{19}$ Semiconducting Polycrystalline Films

Based on the paper published in the Journal of Physical Chemistry C

Journal of Physical Chemistry C. 2012, 116, 10490-10497.

Lindsay Fuoco, Upendra A. Joshi and Paul A. Maggard

Department of Chemistry, North Carolina State University, Raleigh, NC 27695

TOC Caption: Cathodic photocurrents under visible-light irradiation of *p*-type $\text{Cu}_5\text{Ta}_{11}\text{O}_{30}$ and $\text{Cu}_3\text{Ta}_7\text{O}_{19}$ polycrystalline films, and a plot of the electron density for the lowest-energy conduction band states of a TaO_7 layer that is found in each solid.

ABSTRACT

New *p*-type polycrystalline films of semiconducting $\text{Cu}_5\text{Ta}_{11}\text{O}_{30}$ and $\text{Cu}_3\text{Ta}_7\text{O}_{19}$ were prepared on fluorine-doped tin oxide (FTO) glass starting from their CuCl-flux synthesis as highly-faceted micron-sized particles. The particles were annealed on FTO at 400 – 500 °C, followed by a mild oxidation in air at between 250 – 550 °C. In an aqueous 0.5 M Na_2SO_4 electrolyte solution (pH = 6.3), the films exhibit strong cathodic photocurrents under irradiation by visible and/or ultraviolet-light, and which increased with higher annealing and

oxidation temperatures owing to increased *p*-type carrier concentration and better electrical contact between particles. Thermogravimetric analyses show the oxidation treatments result in an oxygen uptake at concentrations of $\sim 3 \times 10^{20} \text{ cm}^{-3}$ at 250 °C, to $\sim 4 \times 10^{21} \text{ cm}^{-3}$ at 550 °C, with the higher temperatures leading to the decomposition of the film. The $\text{Cu}_5\text{Ta}_{11}\text{O}_{30}$ and $\text{Cu}_3\text{Ta}_7\text{O}_{19}$ bulk powders exhibit bandgap sizes of $\sim 2.59 \text{ eV}$ and $\sim 2.47 \text{ eV}$, respectively, and show an onset of their cathodic photocurrents at wavelengths of $\sim 500 - 550 \text{ nm}$. Mott-Schottky measurements of their flat-band potentials have been used to determine the valence band positions at approximately $+1.06$ and $+1.19 \text{ V}$ versus SHE (pH = 6.3), and thus conduction band positions of about -1.53 and -1.28 V for $\text{Cu}_5\text{Ta}_{11}\text{O}_{30}$ and $\text{Cu}_3\text{Ta}_7\text{O}_{19}$, respectively. The band positions are thus suitably located for the photon-driven reduction and oxidation of water. The highest observed incident-photon-to-current efficiencies (IPCE %) for hydrogen production were $\sim 5 \%$ at 350 nm and $\sim 1-2 \%$ at 500 – 600 nm. Electronic structure calculations based on density functional- theory methods show that the conduction band states are delocalized within layers of TaO_7 pentagonal bipyramids, while the valence band states originate within layers of linearly coordinated Cu(I) cations. The lowest-energy bandgap transitions involve a metal-to-metal charge transfer between Cu(I) and Ta(V) cations in these two types of layers. Compared to other Cu(I) oxides, these structures possess sufficiently disperse bands for high carrier mobility within these layers, thus explaining the strong cathodic photocurrents of the films.

INTRODUCTION

The renewable production of fuels from sunlight has generated intense research over the past few decades in the field of semiconducting photoelectrodes, such as for the photon-driven reduction of water or carbon dioxide.¹⁻⁴ Much recent work has focused on the synthesis and development of photoelectrodes capable of utilizing visible-light, and which is a significant fraction of the solar spectrum. The use of metal oxides as photoelectrodes, typically as *n*-type, is attractive owing to their relatively higher inherent stability against photocorrosion. However, metal oxides often suffer from large bandgap sizes that restrict their use to only ultraviolet energies, such as in *n*-type TiO₂. A relatively smaller number of *n*-type metal oxides that absorb at visible-light energies have been explored for use as water oxidation catalysts, such as α -Fe₂O₃, WO₃, and BiVO₄.⁵⁻⁷ However, these decreases in bandgap size are generally found to originate from a downshift in the conduction band energy, and thus making most all of them unsuitable for use as *p*-type photoelectrodes for the reduction of water or carbon dioxide. Just a few examples of *p*-type semiconducting oxides that function as photocathodes under visible-light irradiation have been discovered so far, including Cu₂O, CaFe₂O₄, and metal-ion doped Fe₂O₃.⁸⁻¹¹ Our research efforts in the area have focused on the reduction of bandgap sizes via the use of Nb(V) or Ta(V) cations (empty d^0 -orbitals) that form the conduction band states in early transition-metal oxides, together with a Cu(I) cation (filled d^{10} -orbitals) that can form high-energy valence-band states.¹²⁻¹⁵ For example, the isoelectronic substitution of Cu(I) for the Na cation in the NaNbO₃ photocatalyst decreases its bandgap size from ~3.4 eV to ~2.0 eV via the creation of a new higher-energy valence band consisting of the filled Cu d^{10} orbitals, as found in CuNbO₃.^{12,16}

Recently, we reported the preparation of a polycrystalline CuNbO_3 film as the first *p*-type semiconducting photoelectrode in the Cu(I)-niobate system.¹² However, the preparation and properties of analogous *p*-type Cu(I)-tantalate photoelectrodes remain unexplored. The few known Cu(I) based tantalates include $\text{Cu}_3\text{Ta}_7\text{O}_{19}$, $\text{Cu}_5\text{Ta}_{11}\text{O}_{30}$, and the $\text{Na}_{1-x}\text{Cu}_x\text{Ta}_4\text{O}_{11}$ solid solution.^{13,15,17} These exhibit bandgap sizes down to ~ 2.5 eV, and form in layered structures with the general formula $\text{A}_x\text{Ta}_{3n+1}\text{O}_{8n+3}$. The structure of each member of this family consists of layers of TaO_7 pentagonal bipyramids that alternate with layers of linearly coordinated Cu(I) and TaO_6 octahedra. Nearly all known transition-metal oxide photoelectrodes consist of octahedral MO_6 coordination environments, and almost nothing is known regarding the influence of MO_7 coordination environments on photoelectrochemically-relevant properties. Further, with the exception of $\text{Cu}_3\text{Ta}_7\text{O}_{19}$, these structures exhibit significant Cu-site vacancies of up to $\sim 33\%$.^{13,14} These vacant sites are thus likely accessible to dopants or the incorporation of extra O atom defects.

EXPERIMENTAL

Synthesis and Film Preparation. The syntheses of $\text{Cu}_5\text{Ta}_{11}\text{O}_{30}$ and $\text{Cu}_3\text{Ta}_7\text{O}_{19}$ were performed by a molten-salt flux method using CuCl as the flux. Stoichiometric mixtures of reagent grade Ta_2O_5 (Alfa Aesar, min. 99.99%) and Cu_2O (Alfa Aesar, min. 99.9%) were combined with CuCl (Alfa Aesar, min 99%) at a 10:1 molar ratio (flux:product) in a glovebox with an Argon atmosphere. The reactant mixtures were ground together, loaded into a fused silica ampule, and flame sealed on a vacuum line. The reaction vessels were heated to 900 °C for $\text{Cu}_5\text{Ta}_{11}\text{O}_{30}$ and to 700 °C for $\text{Cu}_3\text{Ta}_7\text{O}_{19}$ for 24 h, and allowed to

radiatively cool in the furnaces. The resulting products were washed with 3M NH₄OH to remove the CuCl flux.

Characterization. Solid-state products were characterized by high resolution powder X-ray diffraction (PXRD) on an INEL diffractometer using Cu K α_1 ($\lambda = 1.54056 \text{ \AA}$) radiation from a sealed-tube X-ray generator equipped with a curved position sensitive detector (CPS120), as well as on a Rigaku R-Axis Spider with a curved image-plate detector. The samples annealed on FTO slides were scraped off of the slides for characterization. Lattice parameters for Cu₅Ta₁₁O₃₀ and Cu₃Ta₇O₁₉ were refined using the Jade 9 software package¹⁸ to $a = 6.2243(9) \text{ \AA}$ and $c = 32.513(6) \text{ \AA}$ for Cu₅Ta₁₁O₃₀ and $a = 6.2338(5) \text{ \AA}$ and $c = 20.166(1) \text{ \AA}$ for Cu₃Ta₇O₁₉, which were consistent with previous reports.^{13,17} Field-emission scanning electron microscopy were performed on a JEOL SEM 6400. Film thicknesses were measured at a tilted 30°, and the correction applied as thickness = observed thickness $\times (1 / \cos(30^\circ))$. UV-Vis diffuse reflectance spectra were collected on a Shimadzu UV-3600 equipped with an integrating sphere. Pressed barium sulfate powder was used as a reference and the data were plotted as the remission function $F(R_\infty) = (1 - R_\infty)^2 / (2R_\infty)$, where R is diffuse reflectance based on the Kubelka-Munk theory of diffuse reflectance.¹⁹ Thermogravimetric analyses were carried out on a TA Instruments Q50. To simulate the same conditions used for the oxidation of the films, the samples were loaded onto Pt pans and stepped to temperatures of 250 °C, 350 °C, or 550 °C at a heating rate of 16.0 °C/ min and held there for 3 h. Samples were characterized by X-ray Photoelectron Spectroscopy (XPS) on a PHOIBIS 150 equipped with a hemispherical analyzer using monochromatized Mg (K $\alpha = 1,254 \text{ eV}$) radiation. A chamber base pressure of approximately 10^{-10} mbar was

achieved under ultrahigh vacuum. The binding energies were internally calibrated to the C 1s peak at 285.0 eV.

Photoelectrochemical measurements were carried out in a Teflon cell with the $\text{Cu}_5\text{Ta}_{11}\text{O}_{30}$ or $\text{Cu}_3\text{Ta}_7\text{O}_{19}$ polycrystalline film as the working electrode, Pt foil as the counter electrode, and a standard calomel reference electrode (SCE). Films were immersed in a 0.5 M Na_2SO_4 electrolyte solution that was adjusted to a pH of ~ 6.3 using dilute H_2SO_4 . The cell was purged with argon gas 30 minutes prior to and during all measurements. An electrochemical analyzer (Princeton Applied Research, PARSTAT 2263) with PowerSuite software was used to measure photocurrent and to carry out chronoamperometry experiments. Films were irradiated from the backside using a 400 W Xe arc lamp equipped with a long-pass cutoff filter (>420 nm) and band-pass filters as appropriate. Further details of the experimental setup have been described in detail elsewhere.¹² For comparison, frontside and backside irradiation studies were performed on $1 \times 1 \text{ cm}^2$ films able to freely rotate within the cell and allowing either frontside or backside illumination under identical conditions. Mott-Schottky measurements were obtained using the AC electrochemical impedance method, with an AC amplitude of 5 mV at an applied frequency of 12 kHz. Incident-photon-to-current conversion efficiency (IPCE) measurements were carried out using band-pass filters of four different wavelengths (352, 451, 522, and 603 nm). The number of photons of monochromatic light reaching the electrode surface was measured at each wavelength using a Si photodiode. The % IPCE is defined as $[(1239.8 \times \text{photocurrent density} [\text{mA}/\text{cm}^2]) / (\text{wavelength} [\text{nm}] \times \text{photon flux} [\text{mW}/\text{cm}^2])] \times 100$.

Electronic Structure Calculations. Band-structure calculations were performed on the geometry-optimized structures of $\text{Cu}_5\text{Ta}_{11}\text{O}_{30}$ and $\text{Cu}_3\text{Ta}_7\text{O}_{19}$ with the use of the plane wave density-functional theory package CASTEP.²⁰ The Perdew-Burke Ernzerhof functional in the generalized-gradient approximation and ultrasoft-core potentials were employed in the calculations.²¹ The selection of equally distributed k -points within the Brillouin zone was automatically calculated according to the Monkhorst pack scheme.²²

RESULTS AND DISCUSSION

Film Characterization. The $\text{Cu}_5\text{Ta}_{11}\text{O}_{30}$ and $\text{Cu}_3\text{Ta}_7\text{O}_{19}$ semiconductors were prepared in high purity according to powder X-ray diffraction (PXRD) and are shown in Figure 2.1 and Figure 2.2 for $\text{Cu}_5\text{Ta}_{11}\text{O}_{30}$ and $\text{Cu}_3\text{Ta}_7\text{O}_{19}$ respectively. Each diffraction peak could be indexed to the theoretical patterns, and the lattice constants were refined to the expected values for their reported crystal structures. After annealing and oxidation of the films, the PXRD data generally confirmed the high crystalline purities of the semiconductors were maintained. However, the $\text{Cu}_5\text{Ta}_{11}\text{O}_{30}$ films oxidized at 450 °C and 550 °C exhibited minor amounts of Ta_2O_5 impurities, and as well, at temperatures of 550 °C the films generally showed significant peak broadening and decreased crystallinity as shown in Figure 2.3 for a $\text{Cu}_3\text{Ta}_7\text{O}_{19}$ oxidized at 550 °C. The total oxidation of $\text{Cu}_5\text{Ta}_{11}\text{O}_{30}$ and $\text{Cu}_3\text{Ta}_7\text{O}_{19}$ was accomplished at a temperature of 750 °C for 3 h in air, yielding Ta_2O_5 and CuTa_2O_6 that contains the oxidized Cu(II) cations. Shown in Figures 2.4 and 2.5 are SEM images of the polycrystalline films of $\text{Cu}_5\text{Ta}_{11}\text{O}_{30}$ and $\text{Cu}_3\text{Ta}_7\text{O}_{19}$ before and after the oxidation treatments. Both sets of images reveal distributions of highly-faceted micron-sized particles, with either

coffin-shaped or irregular block-shaped/hexagonal morphologies for $\text{Cu}_5\text{Ta}_{11}\text{O}_{30}$ and $\text{Cu}_3\text{Ta}_7\text{O}_{19}$, respectively. Specific particle dimensions range from about 3 to 15 μm . Estimated total film thicknesses formed in these samples were measured by cross-sectional SEM images to be fairly thick films, at $\sim 80 \mu\text{m}$ for both. These same particle sizes and morphologies were conserved even after the annealing and oxidation treatments at high temperatures. These results confirmed that high-purity polycrystalline films could be formed.

Photoelectrochemical Properties. Cyclic-voltammetric measurements of $\text{Cu}_5\text{Ta}_{11}\text{O}_{30}$ and $\text{Cu}_3\text{Ta}_7\text{O}_{19}$ films were carried out under chopped visible-light irradiation for an applied bias voltage range of +0.1 to -0.6 V versus SCE, as shown in Figures 2.5, 2.6 and 2.7. For each, a significant cathodic photocurrent was observed that increased with an increasingly negative potential bias, indicating their *p*-type nature in the depletion condition. The measured cathodic photocurrent is weak for the non-oxidized $\text{Cu}_5\text{Ta}_{11}\text{O}_{30}$ film, Figure 2.5, but increases significantly with increasing oxidation temperatures at up to $\sim 1.5 \text{ mA/cm}^2$ at -0.6 V. The increase is notably most significant between 250 °C and 350 °C. At higher oxidation temperatures of 450 °C and 550 °C even stronger photocurrents were observed of $\sim 2.2 \text{ mA/cm}^2$ at -0.6 V (Supporting Information), but these specific films exhibited Ta_2O_5 impurities after the oxidation treatment. Shown in Figure 2.6, a comparison of the cathodic photocurrents for the $\text{Cu}_5\text{Ta}_{11}\text{O}_{30}$ films annealed at 400 °C and 500 °C (in vacuum), followed by oxidation in air at 350 °C, shows that this leads to an even higher photocurrent response of $\sim 2.6 \text{ mA/cm}^2$. This result originates from a better sintering and electrical contact between the particles. By contrast, the $\text{Cu}_3\text{Ta}_7\text{O}_{19}$ films exhibited a significant cathodic photocurrent

even in the absence of its oxidation at high temperatures, shown in Figure 2.7. Its cathodic photocurrent approximately doubled with its oxidation at higher temperatures. The difference in the photocurrent response of the non-oxidized films may be attributed to the Cu(I) site vacancies present in $\text{Cu}_5\text{Ta}_{11}\text{O}_{30}$ but absent in the $\text{Cu}_3\text{Ta}_7\text{O}_{19}$ structure.

The flat-band potentials of the films were characterized using frequency-dependent Mott-Schottky measurements,²³ shown in Figure 2.8, which involves a measurement of the apparent capacitance as a function of potential under depletion conditions. The negative slope of the data shows the expected behavior of a *p*-type semiconductor. The films show some frequency dispersion, but the linear regions can be extrapolated to give *x*-axis intercepts ($V_0 = 0.62$ V and 0.75 V versus SCE at pH = 6.3; or $+0.86$ V and $+0.99$ V versus RHE) that can be used to determine the flat-band potential (V_{fb}) from the equation $V_0 = V_{fb} - kT/e$,² where *k* is the Boltzmann constant, *T* is temperature and *e* is electron charge. This gives flat-band potentials (V_{fb}) of $+0.88$ V and $+1.01$ V versus RHE for $\text{Cu}_5\text{Ta}_{11}\text{O}_{30}$ and $\text{Cu}_3\text{Ta}_7\text{O}_{19}$ films, respectively. For *p*-type semiconductors, the valence band energy (E_v) can be calculated from the flat-band potential (V_{fb}) with the equation:²³ $E_v = V_{fb} + kT \ln(N_A/N_V)$ where N_A is the acceptor concentration (calculated below) and N_V is the effective density of states (typically $\sim 10^{19}$) at the valence band edge. The flat-band potentials yield valence band positions of $+1.06$ V and $+1.19$ V versus RHE (pH = 6.3). Adding the optical bandgap size to the valence band positions gives the conduction band positions at -1.53 V and -1.28 V versus RHE. The energies of the minority carriers at the conduction band edge are thus much more negative than the redox couples for the reduction of water to hydrogen (-0.38 V) at this pH.

The incident-photon-to-current efficiencies (IPCE) of each film for water reduction are plotted in Figure 2.9 as a function of wavelength at an applied potential of -0.6 V, and after subtraction of the dark background current. The $\text{Cu}_5\text{Ta}_{11}\text{O}_{30}$ films show an onset edge at $\sim 475 - 500$ nm consistent with its measured optical bandgap size of ~ 2.59 eV, or ~ 479 nm, and reaching a maximum IPCE of $\sim 5\%$. Both higher annealing and oxidation temperatures of the film lead to a minor shifting of the IPCE curves to higher efficiencies. However, the IPCE does not fall completely to 0% at sub-bandgap energies, especially with higher annealing and oxidation temperatures. This is likely indicative of mid-bandgap states that can facilitate the surface charge transfer with sub-bandgap light irradiation, especially for the higher oxidation temperatures and dopant concentrations (described below). By contrast, the non-oxidized $\text{Cu}_3\text{Ta}_7\text{O}_{19}$ film shows a cleaner onset edge in the IPCE spectrum at ~ 500 nm, consistent with its measured optical bandgap size of ~ 2.47 eV, or ~ 502 nm. A maximum of the IPCE of $\sim 4\%$ is reached, and which falls to 0% for sub-bandgap light energies. In each of the films, higher cathodic photocurrents lead to an increasing dark current at the most negative applied potential, and also to a more rapid decay of the photocurrent. At a low or zero applied constant potential, the dark current and decay in the photocurrent response could be minimized, but which eventually decayed over the course of an hour (Supporting Information). Both PXRD and FESEM measurements taken subsequent to the photocurrent measurements showed no detectable changes in crystalline products, but that did reveal a significant break-up of the particles in the film. Considering the films are backside irradiated and the fact that these solids have absorption coefficients of $\sim 250-700$ cm^{-1} ,¹³ then more than $\sim 64\%$ of the light will be absorbed by the bottom ~ 13 $\mu\text{m} - 36$ μm of the film. With film

thicknesses of ~ 80 μm , the reduction of water is thus achieved deep within the polycrystalline films and closer to the FTO-glass back contact than to the external electrolyte. Shown in Figure 2.10 for $\text{Cu}_5\text{Ta}_{11}\text{O}_{30}$ (500 $^\circ\text{C}$ anneal, 350 $^\circ\text{C}$ oxidation), are both frontside and backside cyclic voltammetry scans taken under chopped visible-light irradiation. Only somewhat larger photocurrents were observed for the backside irradiation, showing that hole transport to the surface is slightly more difficult than electron transport to the back contact.

Thermogravimetric and UV-Vis diffuse reflectance data were taken in order to probe the origin of the significant increase in cathodic photocurrent with the film oxidation temperature. The acceptor densities (N_A) for each of the films have been calculated from the slopes of the Mott-Schottky plots to be $\sim 1.0 \times 10^{16} \text{ cm}^{-3}$ for both. Upon a slow oxidation of the films for 3 h in air at 250 $^\circ\text{C}$ to 550 $^\circ\text{C}$, the polycrystalline films exhibited a significant oxygen uptake of from $\sim 0.17 - 1.00$ oxygen atoms per formula unit of $\text{Cu}_5\text{Ta}_{11}\text{O}_{30}$ and $\sim 0.37 - 1.32$ oxygen atoms per formula unit of $\text{Cu}_3\text{Ta}_7\text{O}_{19}$ (see Supporting Information). The highest oxygen uptake and oxidation temperature of 550 $^\circ\text{C}$ yielded a partial decomposition of the products. However, at 250 $^\circ\text{C}$ the oxygen uptake corresponded to dopant oxygen densities of $\sim 3.2 \times 10^{20}$ oxygen-dopant/ cm^3 , and at 350 $^\circ\text{C}$ of $\sim 1.0 \times 10^{21}$ oxygen-dopant/ cm^3 . The significant enhancement of cathodic photocurrent between these two temperatures is explained by the order of magnitude change in the oxygen-atom dopant density, and which are both about four orders of magnitude greater than the non-oxidized films. The UV-Vis diffuse reflectance spectra are shown in Figure 2.11 for both oxidized and non-oxidized films of $\text{Cu}_5\text{Ta}_{11}\text{O}_{30}$ and $\text{Cu}_3\text{Ta}_7\text{O}_{19}$. The optical absorption edges of the non-oxidized films were both sharp and clearly defined, consistent with previous reports of

their bandgap sizes of ~2.59 eV and ~2.47 eV.¹³ However, oxidation of the $\text{Cu}_5\text{Ta}_{11}\text{O}_{30}$ and $\text{Cu}_5\text{Ta}_{11}\text{O}_{30}$ films at temperatures of 350 °C or greater results in the disappearance of a defined absorption edge and instead a broad diffuse reflectivity that is more characteristic of a degenerate semiconductor. This occurs concomitantly with the sharp increase in photocurrents observed in Figure 2.5. While a higher electrical conductivity enhances the mobility of charge carriers and thus the cathodic photocurrents, the high amount of *p*-type dopants ($> 10^{19}$ - 10^{20} cm^{-3} in most cases) most likely results in a degenerate semiconductor under these conditions.

In order to investigate changes in the oxidation states and coordination environments at the particles' surfaces, X-ray photoelectron spectra were taken for $\text{Cu}_5\text{Ta}_{11}\text{O}_{30}$ and $\text{Cu}_3\text{Ta}_7\text{O}_{19}$ before and after oxidation as well as before and after photocurrent measurements, as shown in Figure 2.12. Before oxidation, both films exhibited two Cu $2p_{3/2}$ absorption peaks at 932.9 eV and 934.7 eV, as well as two Cu $2p_{1/2}$ absorption peaks located at 952.6 eV and 954.7 eV, corresponding to Cu(I) and Cu(II) respectively. For $\text{Cu}_3\text{Ta}_7\text{O}_{19}$, these two sets of absorption peaks are shifted to slightly lower binding energies and are less resolved, indicating a greater amount of Cu(II) present at the surfaces compared to the $\text{Cu}_5\text{Ta}_{11}\text{O}_{30}$ phase. After oxidation of the films at 350 °C, both only exhibited broad Cu $2p_{3/2}$ absorption peaks corresponding to primarily Cu(II) at the surfaces. Intense shake-up satellite peaks present at 943.8 eV and 962.7 eV, characteristic of the open-shell $3d^9$ configuration of Cu (II), were also observed for the oxidized samples.²⁴ The Cu 2p spectra remained unchanged for data taken before and after chronoamperometry measurements for 1 h. However, the presence of small amounts of Cu(0) at the surfaces would not be detectable because the

expected chemical shift associated with the binding energies of Cu(0) is only 0.1 eV lower than those for Cu(I). XPS data for the O 1s core-level binding energies, given in the Supporting Information, are consistent with those reported for Cu(I) in Cu₂O.²⁵ Oxidation of both phases resulted the presence of an additional peak at lower energies consistent with Cu(II) in the CuO phase.²⁵ The Ta 4f core-level binding energies were measured at ~28 eV and ~26 eV, consistent with Ta(V) ions present in both of the compounds. While oxidation of the samples resulted in a shift of these absorption peaks to lower energies, no differences were observed before and after the chronoamperometric measurements. Taken together, these data are consistent with the oxidation of Cu(I) at the surfaces to Cu(II), but with no detectable changes resulting from the photocathodic currents to suggest that corrosion is occurring at the surfaces. However, the formation of Cu(0) also cannot be ruled out.

Electronic Band-Structure Calculations. Electronic structures were calculated based on plane-wave DFT-methods from the geometry-optimized crystal structures reported for both of the Cu(I)-tantalate structures.¹³ These structures consist of layers of edge-shared TaO₇ pentagonal bipyramids as well as layers of Cu(I)/TaO₆ octahedra. The difference is that while the Cu₃Ta₇O₁₉ structure is comprised of the stacking of double layers of TaO₇ units, the Cu₅Ta₁₁O₃₀ structure consists of alternating single and double layers of the TaO₇ units. The calculated band structure for Cu₃Ta₇O₁₉ is plotted in Figure 2.13, and predicts the highest carrier mobilities within the 2D plane defined by $k = K \rightarrow G \rightarrow M$ (labeled with arrows) in the plane of the TaO₇ layers, but a lower mobility for the reciprocal directions along $k = L \rightarrow M \rightarrow K$ between the layers. The effective mass of the carriers is inversely proportional to the rate of change of the band energy in k -space (i.e., $m^* \propto (\partial E)^2 / \partial^2 k$),²⁶ and

which leads to higher carrier mobilities (μ) for more disperse bands. Shown in Figure 2.14 are the two types of layers and the calculated electron-density plots of the highest-energy parts of the valence band (reddish-orange electron density; right) and the lowest-energy components of the conduction band (yellowish green electron density, left). Thus, electron density in these layers represents the lowest-energy bandgap transition between the conduction and valence bands, and which is primarily a transition between filled Cu d^{10} and empty Ta d^0 -based crystal orbitals. The valence band states are shown to reside predominantly on Cu(I) ions, while the conduction band states are found to occur over both the TaO₇ in the double layers as well as the isolated TaO₆ octahedra. Surprisingly, the single layers of TaO₇ in Cu₅Ta₁₁O₃₀ do not contribute to these conduction band states, but only its double layer structural feature that it shares in common with Cu₃Ta₇O₁₉. Additional minor contributions arise from the bridging oxygen ligands between the edge-linked TaO₇ polyhedra, and showing that excited electrons into this band would migrate within the 2D layers of this structure. The isolated Cu(I)/TaO₆ layer in Figure 2.14 shows that while there are shared Cu–O–Ta bridging interactions that would facilitate a charge-transfer transition to the tantalate layer, there are no direct Cu–O–Cu bridges to facilitate hole transport within these layers of the structures. The direct Cu – Cu distances are $\sim 3.10\text{\AA}$ within these structures. Further, the plausible location for the incorporation of oxygen dopants into this layer is between three neighboring Cu(I) sites (e.g., at $x = 2/3$, $y = 1/3$, $z = 0.0952$ in Cu₅Ta₁₁O₃₀), giving reasonable Cu–O distances of $\sim 1.80\text{-}1.90\text{\AA}$, as similarly recently reported for LaCuO_{2.66}.²⁷ Further investigations are necessary to characterize the type and location of the *p*-type oxygen-atom defect sites within these structures.

CONCLUSIONS

New *p*-type polycrystalline films of semiconducting $\text{Cu}_5\text{Ta}_{11}\text{O}_{30}$ and $\text{Cu}_3\text{Ta}_7\text{O}_{19}$ could be prepared on FTO glass at 400 – 500 °C and oxidation in air at between 250 – 550 °C. The films exhibit strong cathodic photocurrents under irradiation by visible and/or ultraviolet-light irradiation, and which increased with higher annealing and oxidation temperatures owing to a better sintering of the particles as well as by increasing the concentration of *p*-type dopants. Onset of their cathodic photocurrents is found to begin at wavelengths of ~500 – 550 nm, with new *p*-type polycrystalline films of semiconducting $\text{Cu}_5\text{Ta}_{11}\text{O}_{30}$ and $\text{Cu}_3\text{Ta}_7\text{O}_{19}$ could be prepared on FTO glass at 400 – 500 °C and oxidation in air at between 250 – 550 °C. The films exhibit strong cathodic photocurrents under irradiation by visible and/or ultraviolet-light irradiation, and which increased with higher annealing and oxidation temperatures owing to a better sintering of the particles as well as by increasing the concentration of *p*-type dopants. Onset of their cathodic photocurrents is found to begin at wavelengths of ~500 – 550 nm, with highest observed incident-photon-to-current efficiencies of ~5 % at 350 nm and ~1-2 % at 500 – 600 nm. Mott-Schottky plots locate the valence band positions at +1.06 V and +1.19 V (versus SHE at pH = 6.3) and conduction band positions at –1.53 V and –1.28 V for $\text{Cu}_5\text{Ta}_{11}\text{O}_{30}$ and $\text{Cu}_3\text{Ta}_7\text{O}_{19}$, respectively. DFT-based electronic structure calculations reveal the conduction band states derive from the double layers of TaO_7 pentagonal bipyramids with the highest calculated band dispersion and mobility of the minority carriers within this layer. Thus, these initial investigations of two new *p*-type semiconductors show that they can be prepared as polycrystalline films and which show promise for potential use in solar-energy-to-fuels production. A full investigation of the

effects of different thicknesses and particle sizes of the films on their stability and cathodic photocurrent is ongoing and will be reported in a future study.

ACKNOWLEDGEMENTS

The authors acknowledge support of this research from the Chemical Sciences, Geosciences and Biosciences Division, Office of Basic Energy Sciences, Office of Science, U.S. Department of Energy (DE-FG02-07ER15914).

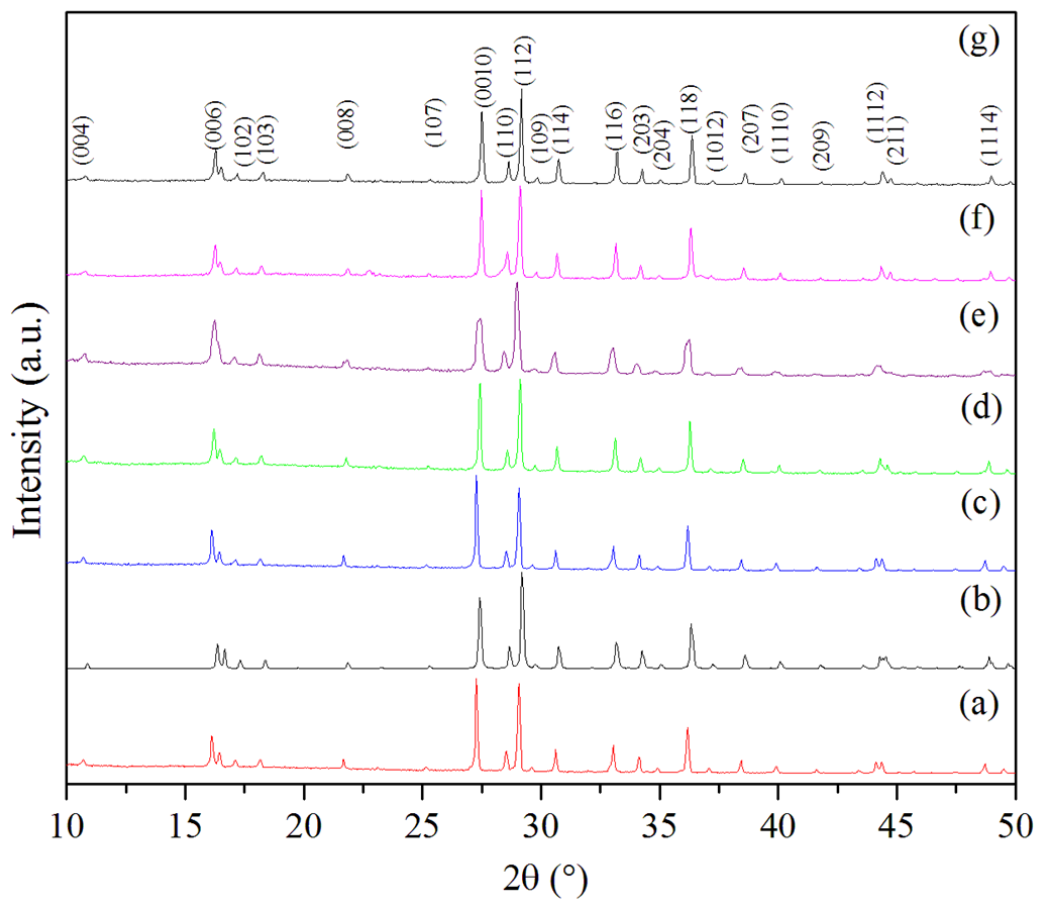


Figure 2.1. Powder X-ray diffraction data for (a) as-prepared $\text{Cu}_5\text{Ta}_{11}\text{O}_{30}$, (b) calculated pattern of $\text{Cu}_5\text{Ta}_{11}\text{O}_{30}$, and films of $\text{Cu}_5\text{Ta}_{11}\text{O}_{30}$, (c) annealed at 400 °C and oxidized at 250 °C, (d) annealed at 400 °C and oxidized at 350 °C, (e) annealed at 400 °C and oxidized at 450 °C, (f) annealed at 400 °C and oxidized at 550 °C, and (g) annealed at 500 °C and oxidized at 350 °C.

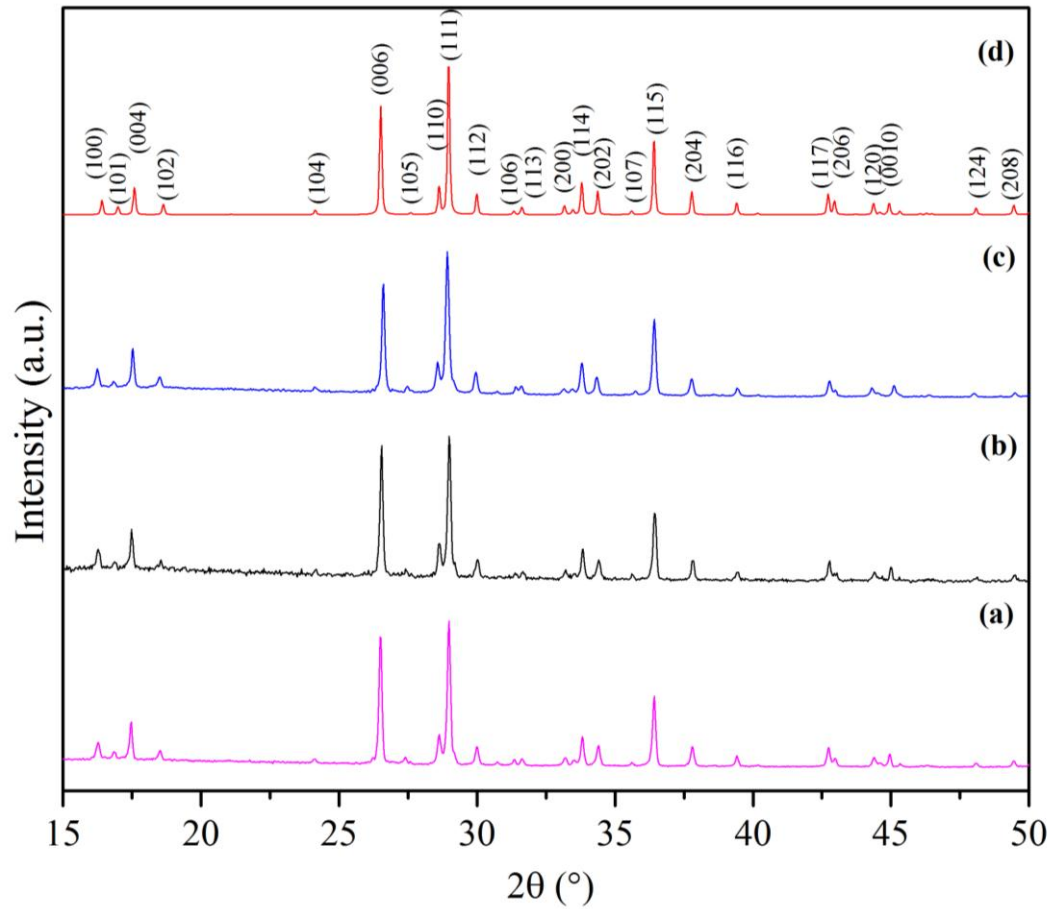


Figure 2.2. Powder X-ray diffraction data for (a) bulk $\text{Cu}_3\text{Ta}_7\text{O}_{19}$, (b) $\text{Cu}_3\text{Ta}_7\text{O}_{19}$ film annealed at 500 °C and (c) oxidized at 350 °C (d) calculated pattern of $\text{Cu}_3\text{Ta}_7\text{O}_{19}$.

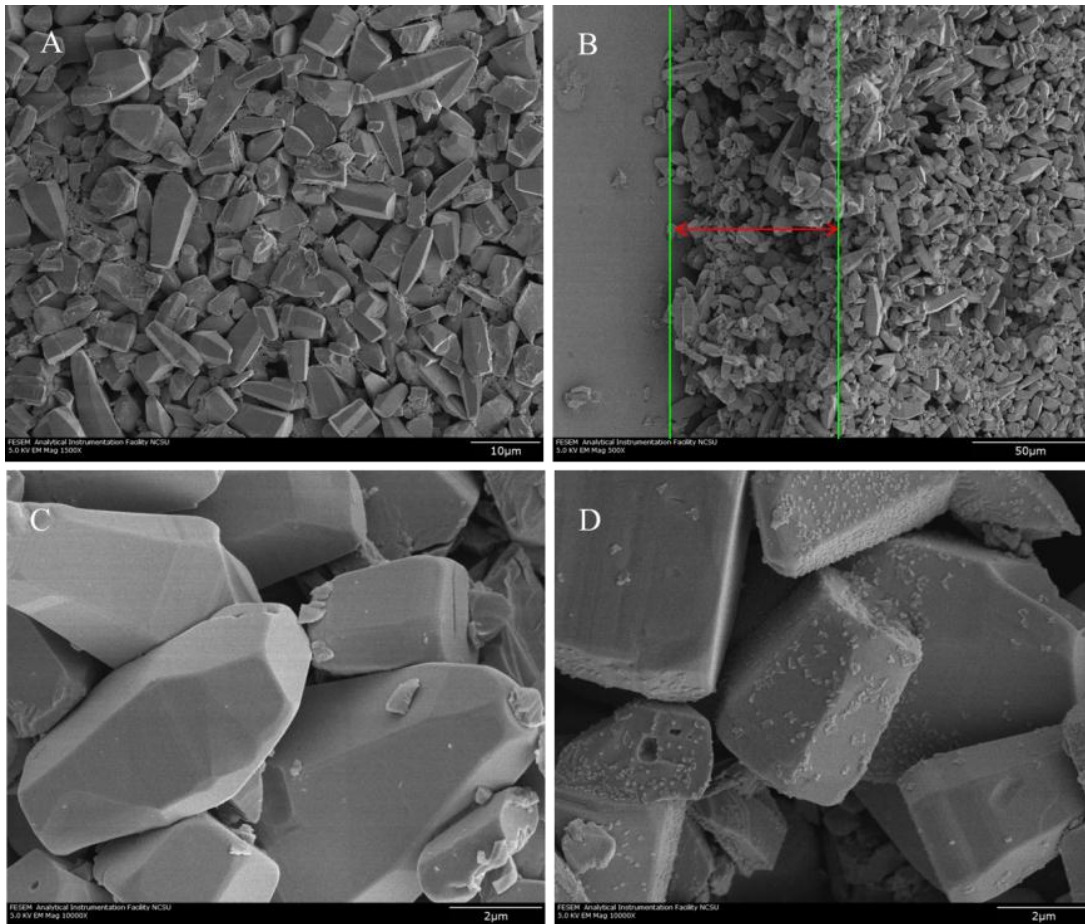


Figure 2.3. SEM images of a $\text{Cu}_5\text{Ta}_{11}\text{O}_{30}$ film (A) after annealing at 400 °C for 3 h, (B) an $\sim 30^\circ$ tilted cross-section view of film after oxidizing at 250 °C for 3 h, and (C and D) after annealing at 400 °C for 3 h before and after oxidizing at 350 °C, respectively.

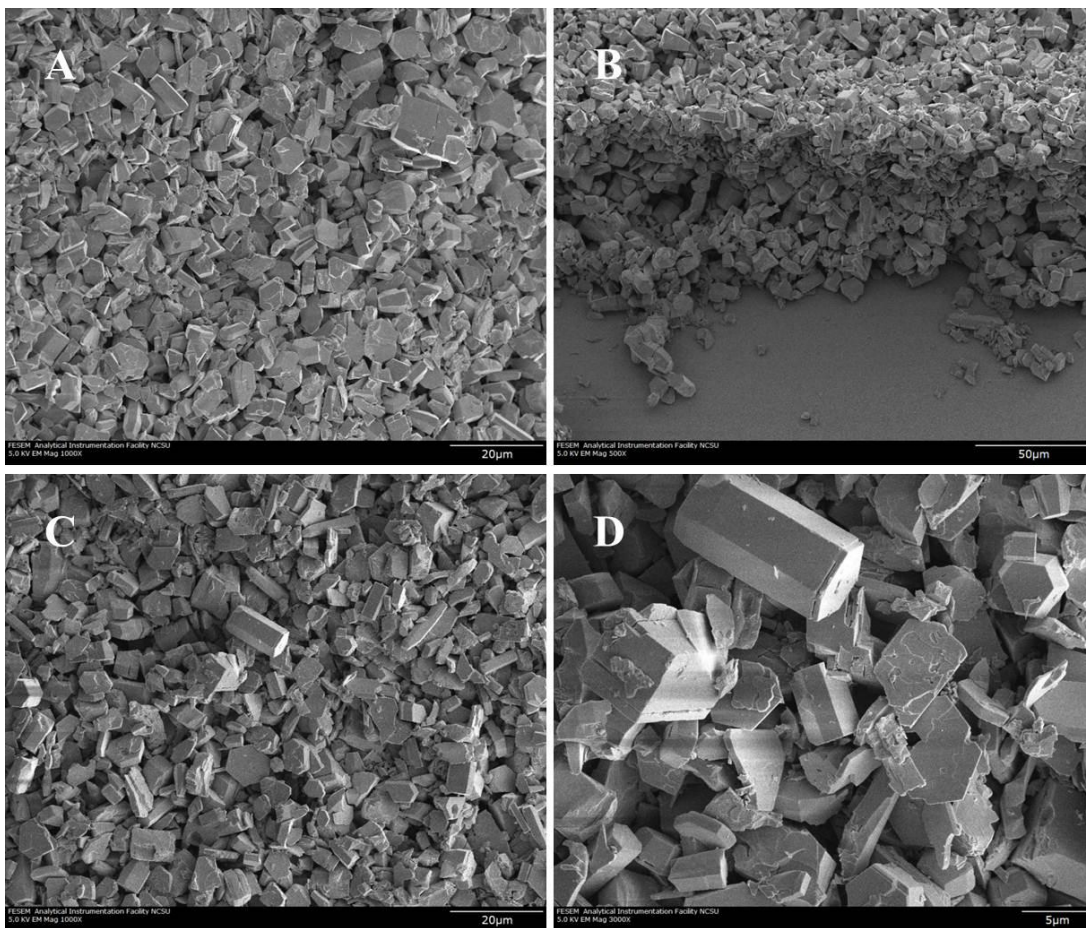


Figure 2.4. SEM images of a $\text{Cu}_3\text{Ta}_7\text{O}_{19}$ film (A) after annealing at $500\text{ }^\circ\text{C}$ for 3 h, (B) an $\sim 30^\circ$ tilted cross-section view of film, and (C and D) and after the chronoamperometry measurements, respectively.

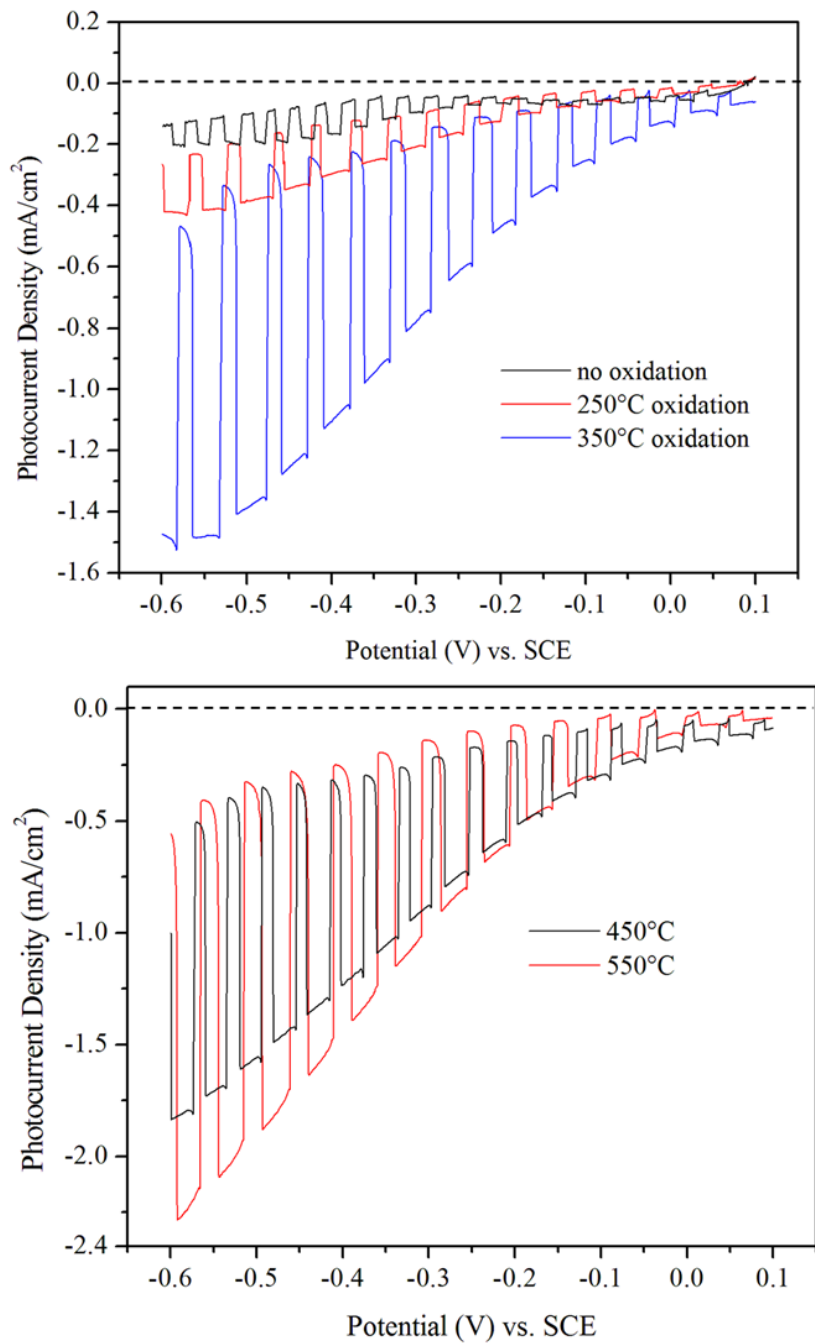


Figure 2.5. Current-potential curves in aqueous 0.5 M Na₂SO₄ solution (pH = 6.3) under chopped visible-light irradiation for Cu₅Ta₁₁O₃₀ films annealed at 400 °C for 3 h and not oxidized or oxidized for 3 h at 250 °C, 350 °C (upper chart), and oxidized for 3 h at 450 °C, 550 °C (lower chart).

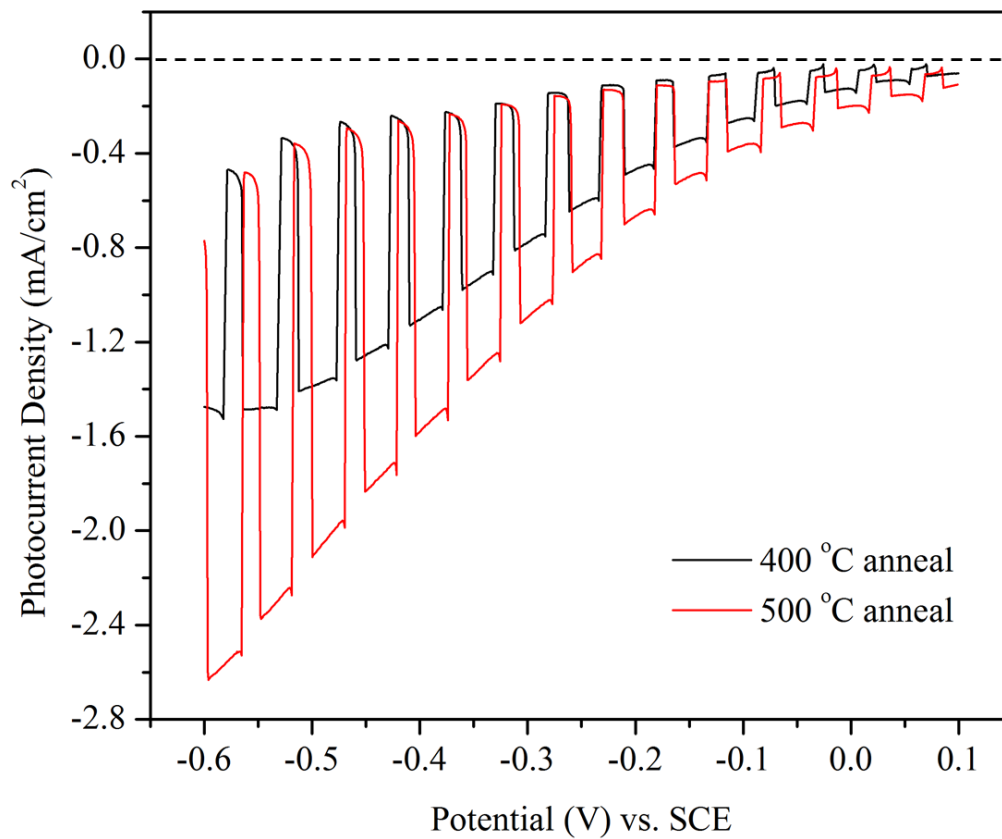


Figure 2.6. Current-potential curves in aqueous 0.5 M Na_2SO_4 solution (pH = 6.3) under chopped visible-light irradiation for $\text{Cu}_5\text{Ta}_{11}\text{O}_{30}$ films annealed at 400 °C and 500°C followed by oxidation at 350 °C for 3 h.

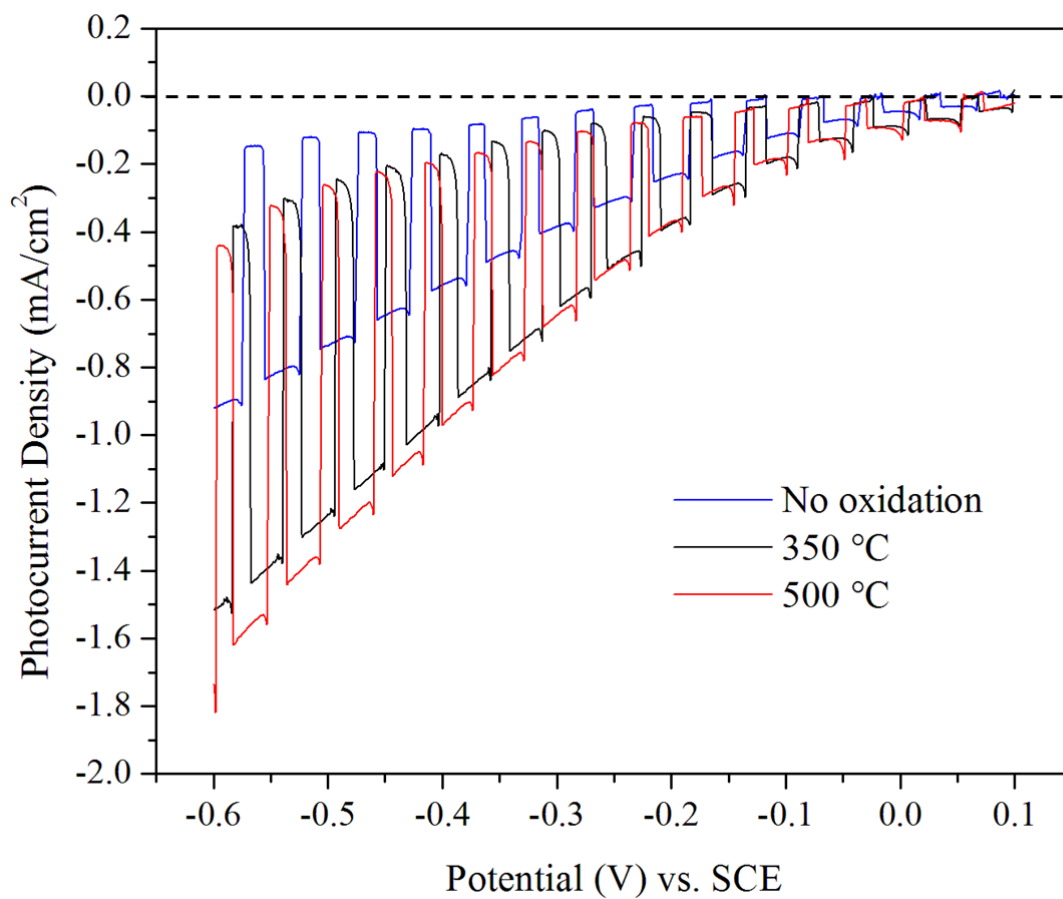


Figure 2.7. Current-potential curve in aqueous 0.5 Na₂SO₄ solution (pH = 6.3) under chopped visible-light irradiation for Cu₃Ta₇O₁₉ films annealed at 500 °C for 3 h and not oxidized or oxidized for 3 h at 350 °C and 550 °C.

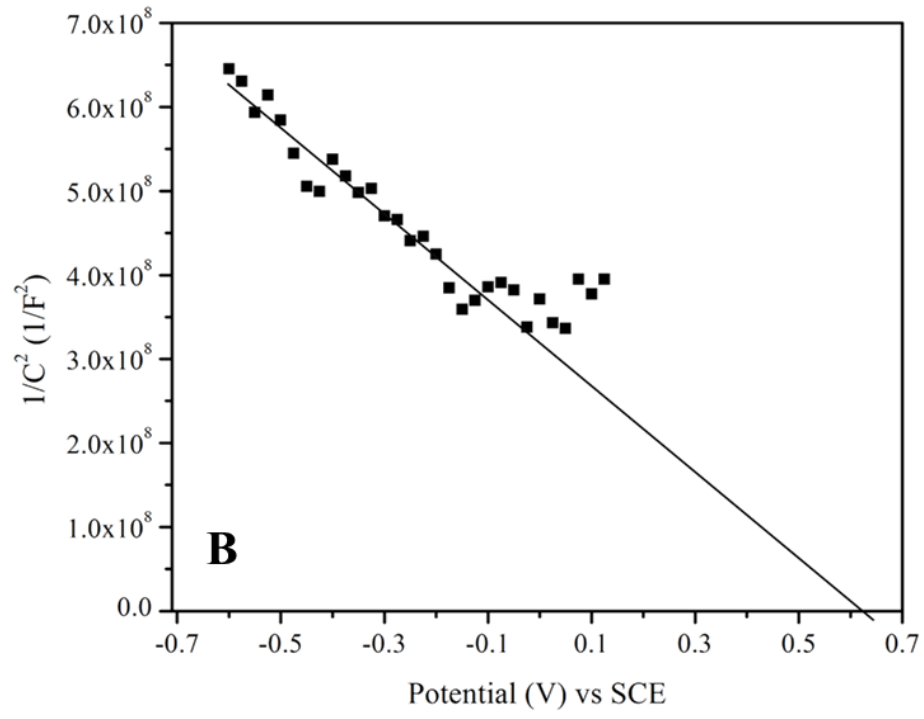
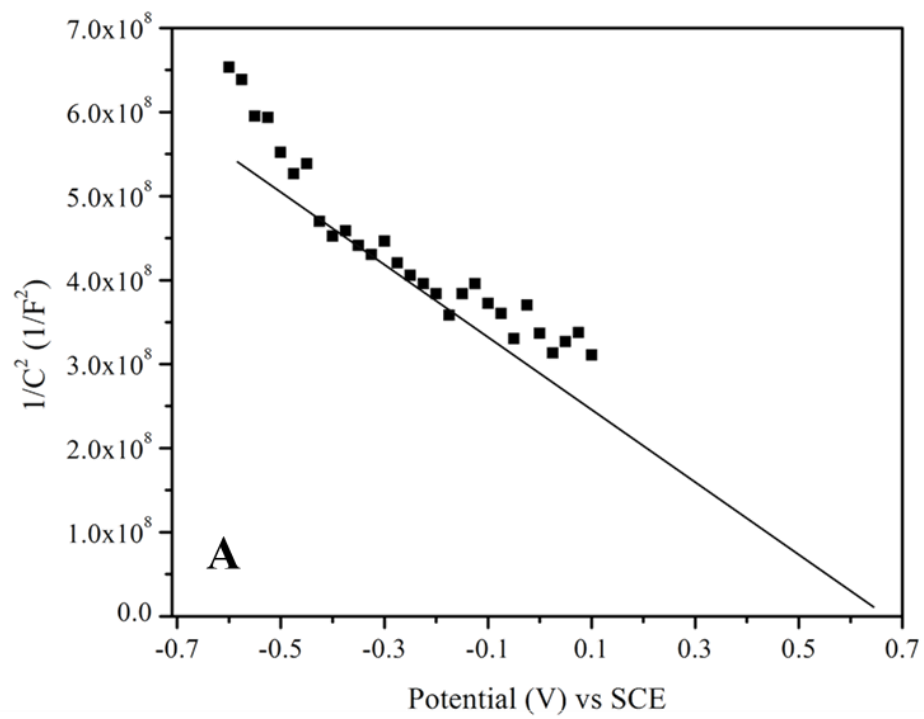


Figure 2.8. Mott-Schottky plots for the (A) $\text{Cu}_3\text{Ta}_7\text{O}_{19}$ and (B) $\text{Cu}_5\text{Ta}_{11}\text{O}_{30}$ polycrystalline films annealed at 500°C .

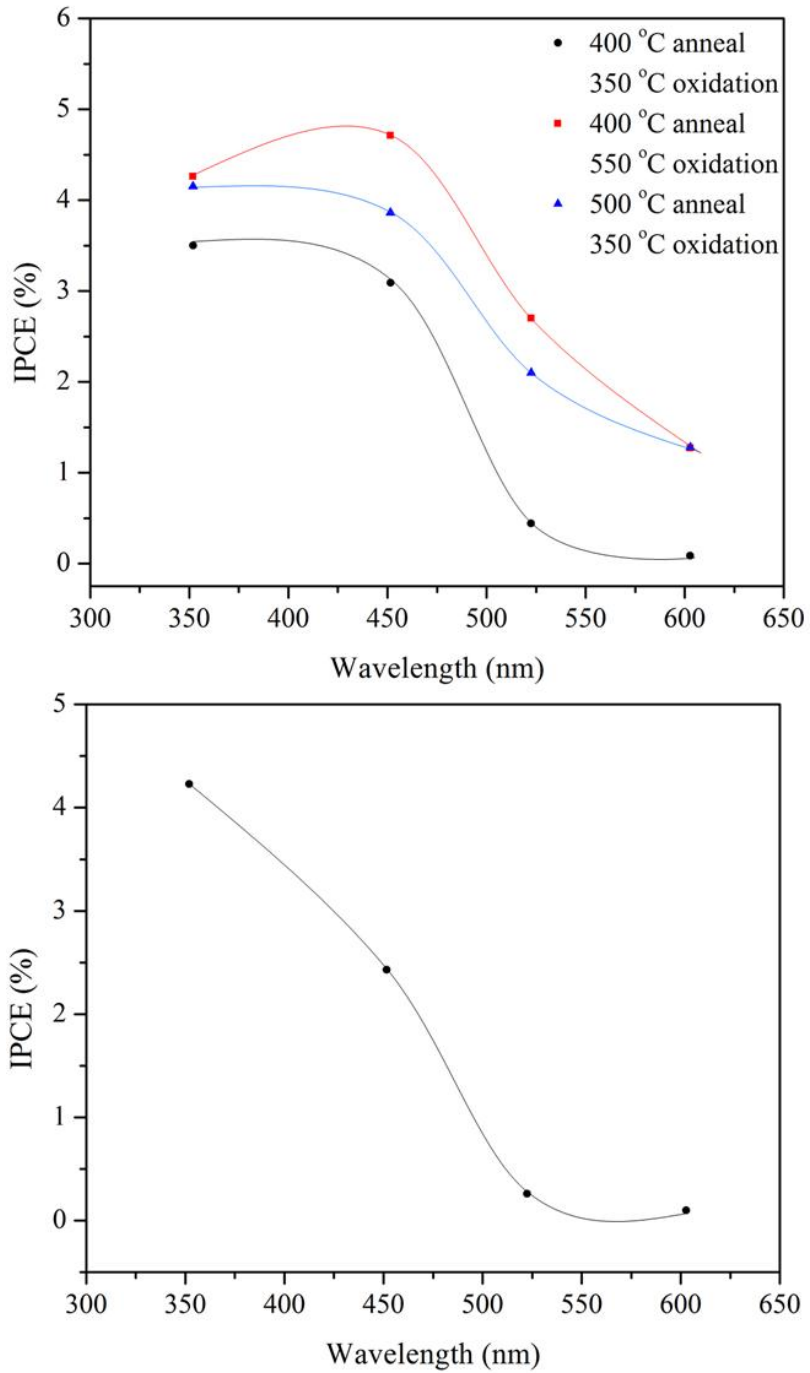


Figure 2.9. Incident-photon-to-current (IPCE) efficiencies (upper plot) for $\text{Cu}_5\text{Ta}_{11}\text{O}_{30}$ films annealed at 400 °C or 500 °C and oxidized at 350 °C or 550 °C, and (lower plot) a $\text{Cu}_3\text{Ta}_7\text{O}_{19}$ film annealed at 500 °C and no oxidation.

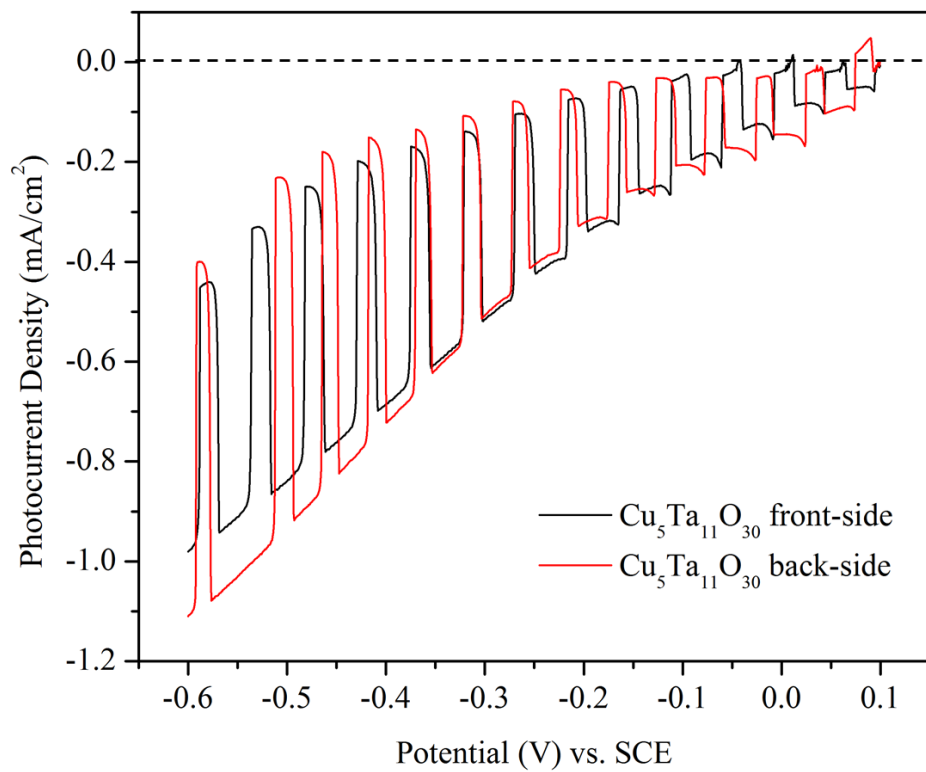


Figure 2.10. Current-potential curves of $\text{Cu}_5\text{Ta}_{11}\text{O}_{30}$ film annealed at $500\text{ }^\circ\text{C}$ and oxidized at $350\text{ }^\circ\text{C}$ in aqueous $0.5\text{ M Na}_2\text{SO}_4$ solution ($\text{pH} = 6.3$) under chopped frontside or backside visible-light illumination.

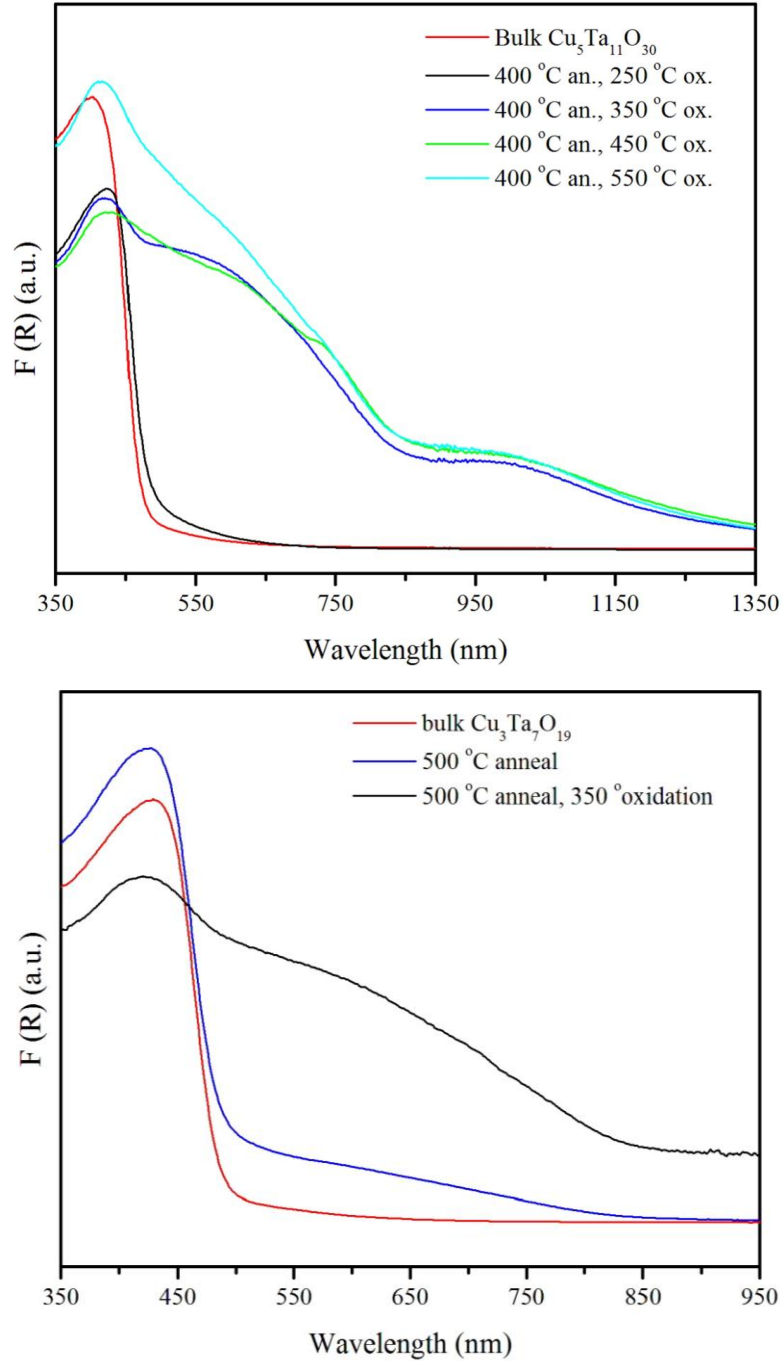


Figure 2.11. UV-Vis diffuse reflectance spectra for (upper plot) $\text{Cu}_5\text{Ta}_{11}\text{O}_{30}$ films annealed at 400 °C and oxidized at various temperatures from 250 °C to 550 °C, and (lower plot) $\text{Cu}_3\text{Ta}_7\text{O}_{19}$ films annealed at 500 °C and oxidized at 350 °C.

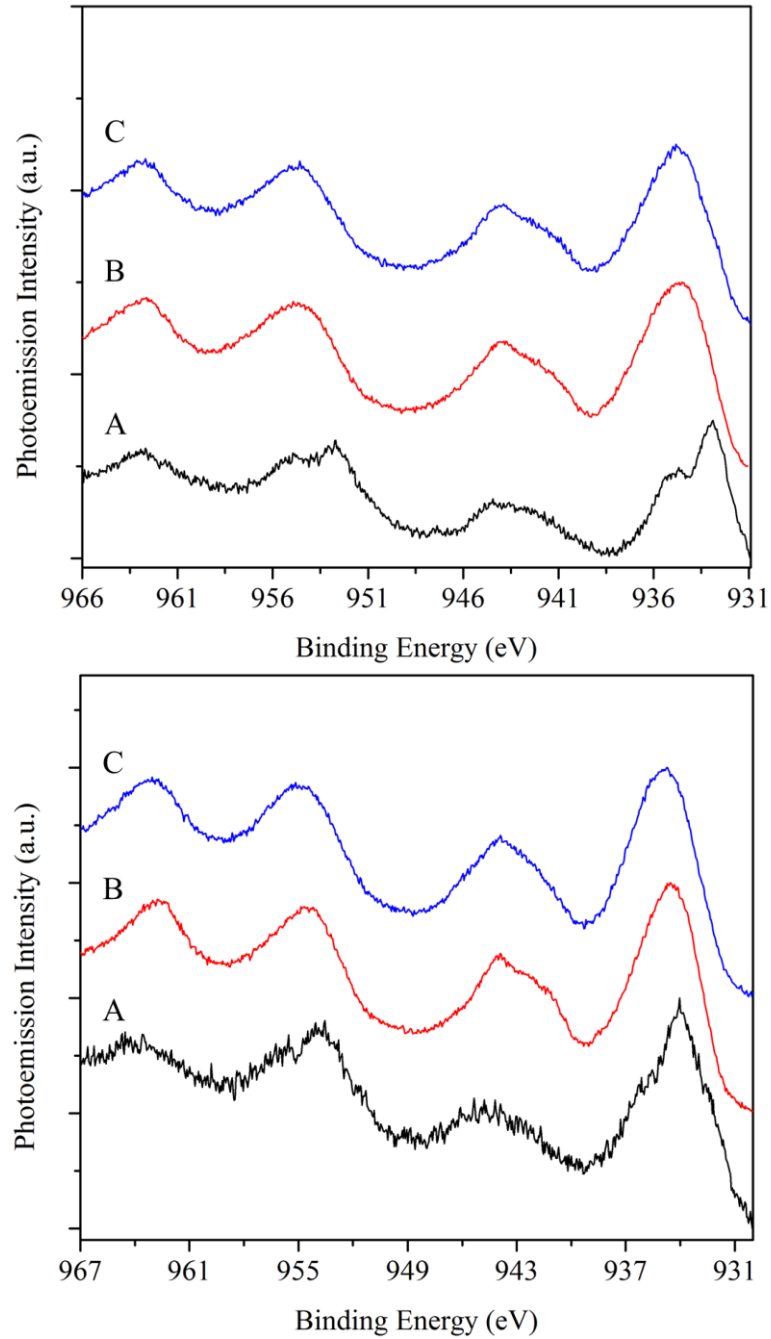


Figure 2.12. Cu 2p core-level spectra for $\text{Cu}_5\text{Ta}_{11}\text{O}_{30}$ (upper plot) and $\text{Cu}_3\text{Ta}_7\text{O}_{19}$ (lower plot) films annealed at 500 °C without oxidation (A), oxidized at 350 °C before (B) and after chronoamperometry (C).

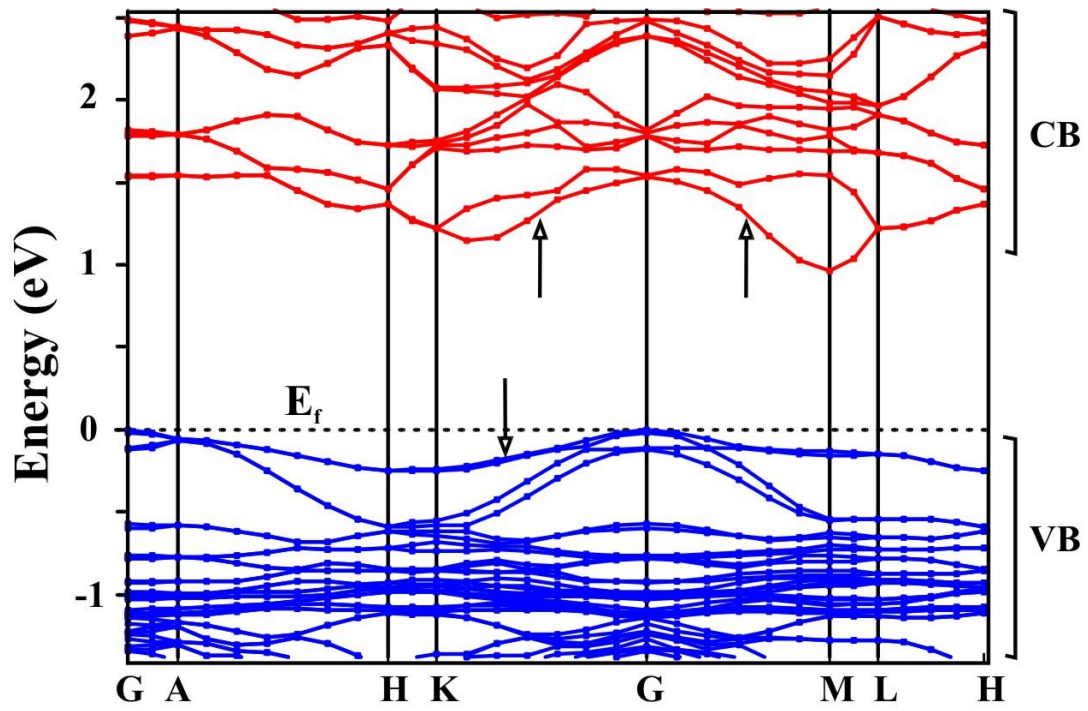


Figure 2.13. Calculated band-structure k -space diagram for $\text{Cu}_3\text{Ta}_7\text{O}_{19}$, with arrows labeling the higher band-dispersion directions.

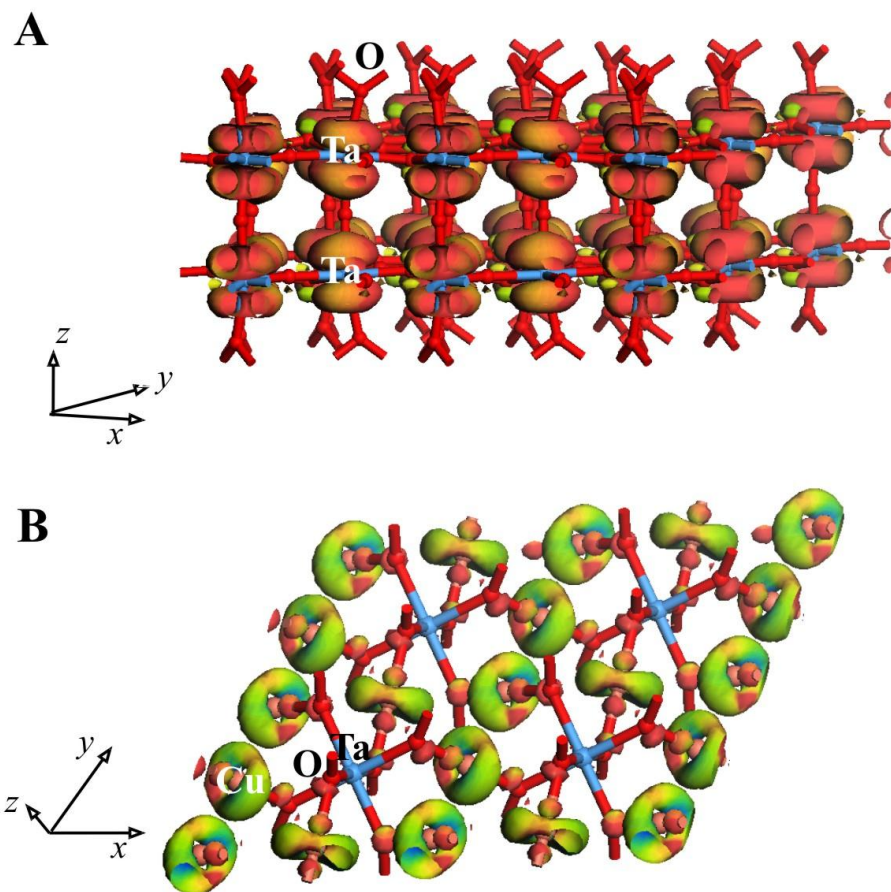


Figure 2.14. Calculated electron density for the lowest-energy conduction band states (A; reddish-orange density) and for the highest-energy valence band states (B; yellowish-green density), which is concentrated within the TaO₇ layers and the TaO₆/Cu layers, respectively.

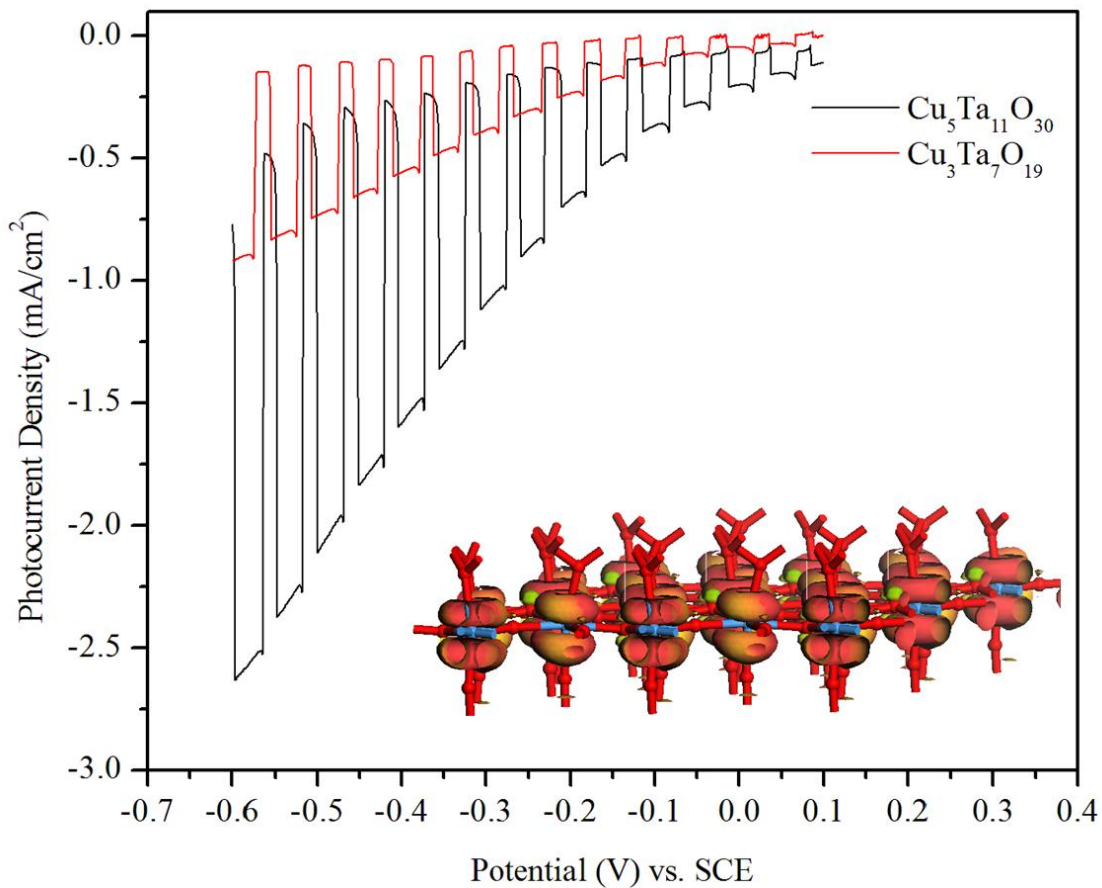


Figure 2.15. TOC Caption Cathodic photocurrents under visible-light irradiation of *p*-type $\text{Cu}_5\text{Ta}_{11}\text{O}_{30}$ and $\text{Cu}_3\text{Ta}_7\text{O}_{19}$ polycrystalline films, and a plot of the electron density for the lowest-energy conduction band states of a TaO_7 layer that is found in each solid.

SUPPORTING INFORMATION

“Preparation and Photoelectrochemical Properties of *p*-type $\text{Cu}_5\text{Ta}_{11}\text{O}_{30}$ and $\text{Cu}_3\text{Ta}_7\text{O}_{19}$ Semiconducting Polycrystalline Films”

Lindsay Fuoco, Upendra A. Joshi and Paul A. Maggard

Department of Chemistry, North Carolina State University, Raleigh, NC 27695

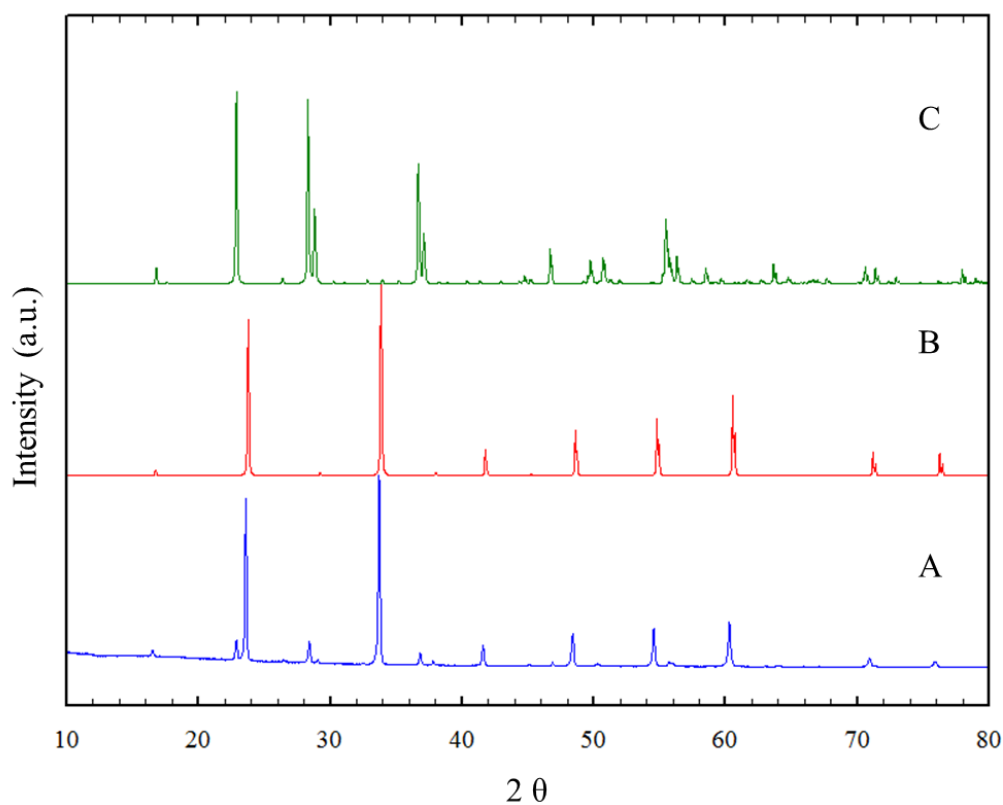


Figure 2.S1. Powder X-ray diffraction data for (a) $\text{Cu}_5\text{Ta}_{11}\text{O}_{30}$ oxidized at 750 °C for 3 h, (b) calculated pattern of CuTa_2O_6 , and (c) calculated pattern of Ta_2O_5 .

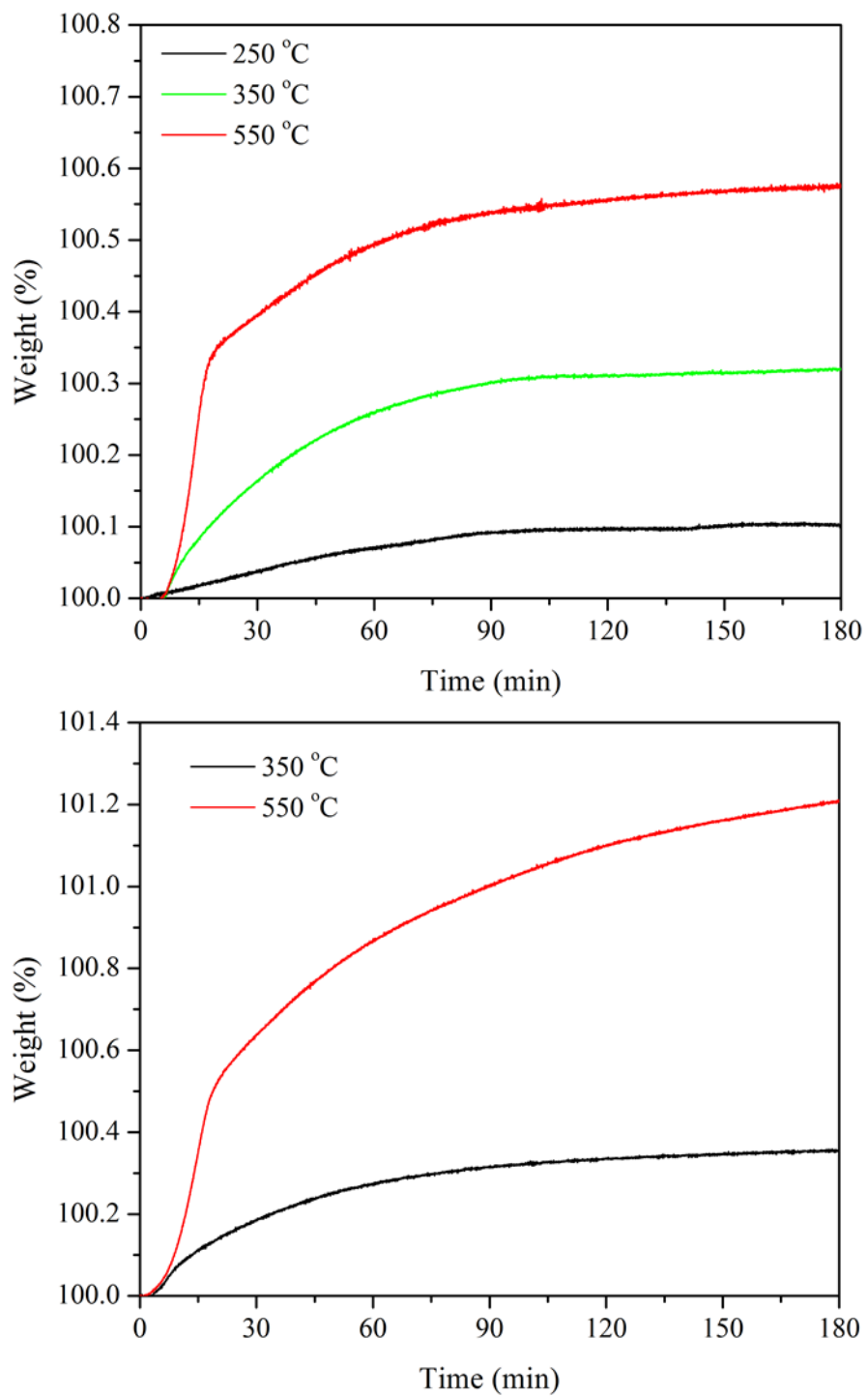


Figure 2.S2. Thermogravimetric analyses (in air) versus time for $\text{Cu}_5\text{Ta}_{11}\text{O}_{30}$ (upper) at 250 °C, 350 °C and 550 °C and for $\text{Cu}_3\text{Ta}_7\text{O}_{19}$ (lower) at 350 °C and 550 °C.

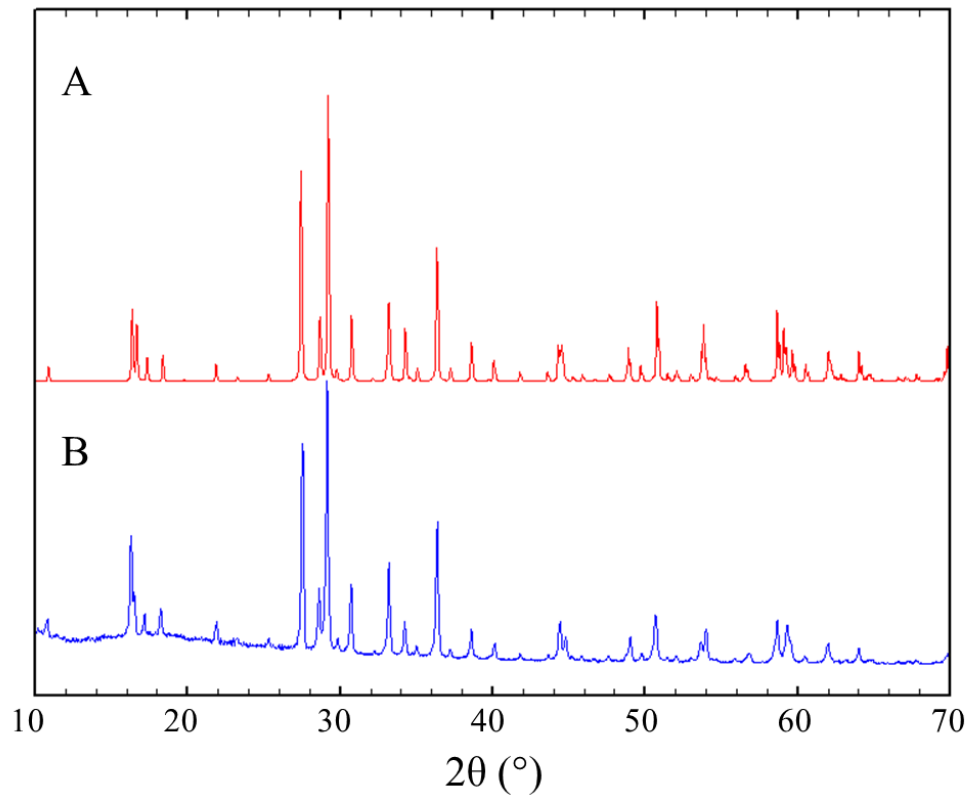


Figure 2.S3. Powder x-ray diffraction data of (A) calculated $\text{Cu}_5\text{Ta}_{11}\text{O}_{30}$ and (B) the $\text{Cu}_5\text{Ta}_{11}\text{O}_{30}$ film after chronoamperometry (-0.4 V applied bias potential) for 1 h.

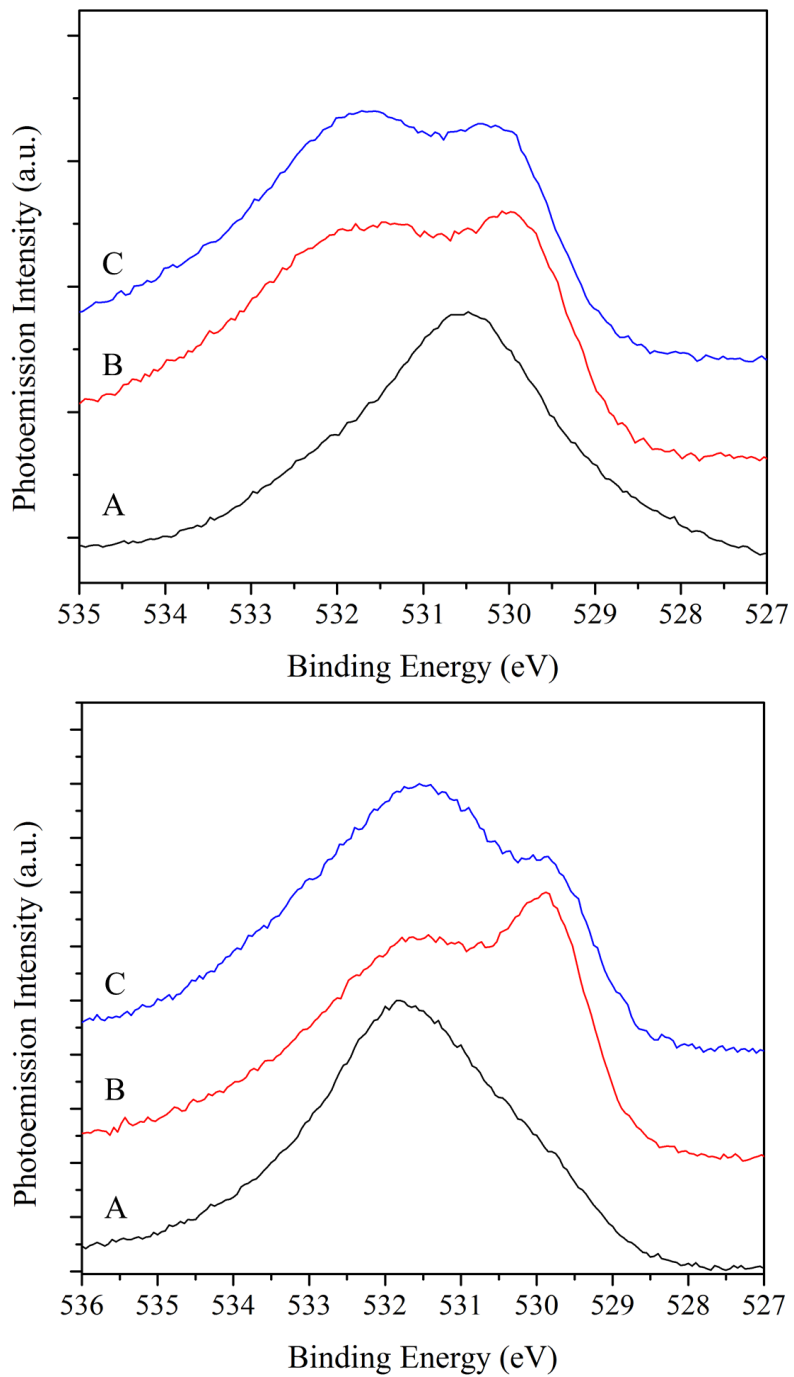


Figure 2.S4. O 1s core-level spectra for $\text{Cu}_5\text{Ta}_{11}\text{O}_{30}$ (upper plot) and $\text{Cu}_3\text{Ta}_7\text{O}_{19}$ (lower plot) films annealed at 500 °C without oxidation (A), oxidized at 350 °C before (B) and after chronoamperometry (C).

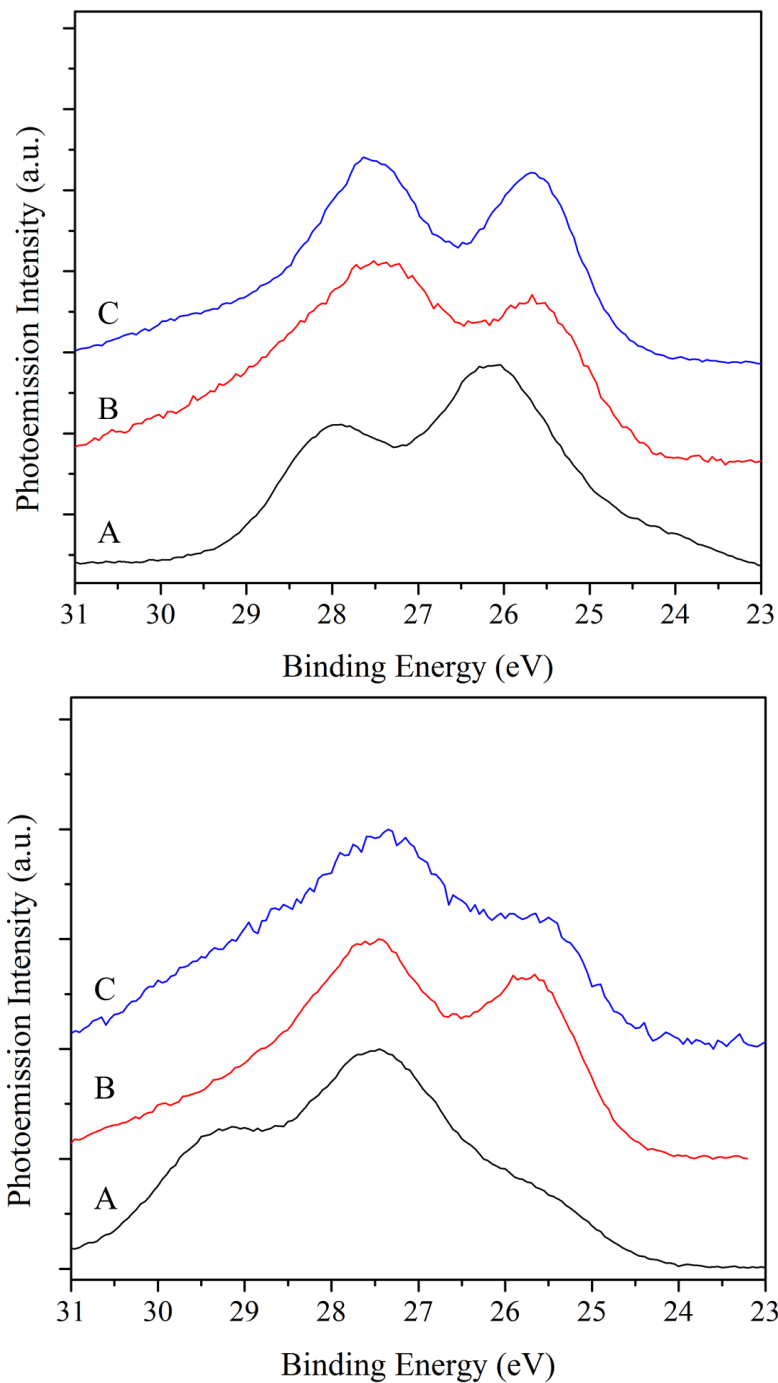


Figure 2.S5. Ta 4f core-level spectra for $\text{Cu}_5\text{Ta}_{11}\text{O}_{30}$ (upper plot) and $\text{Cu}_3\text{Ta}_7\text{O}_{19}$ (lower plot) films annealed at 500 °C without oxidation (A), oxidized at 350 °C before (B) and after chronoamperometry (C).

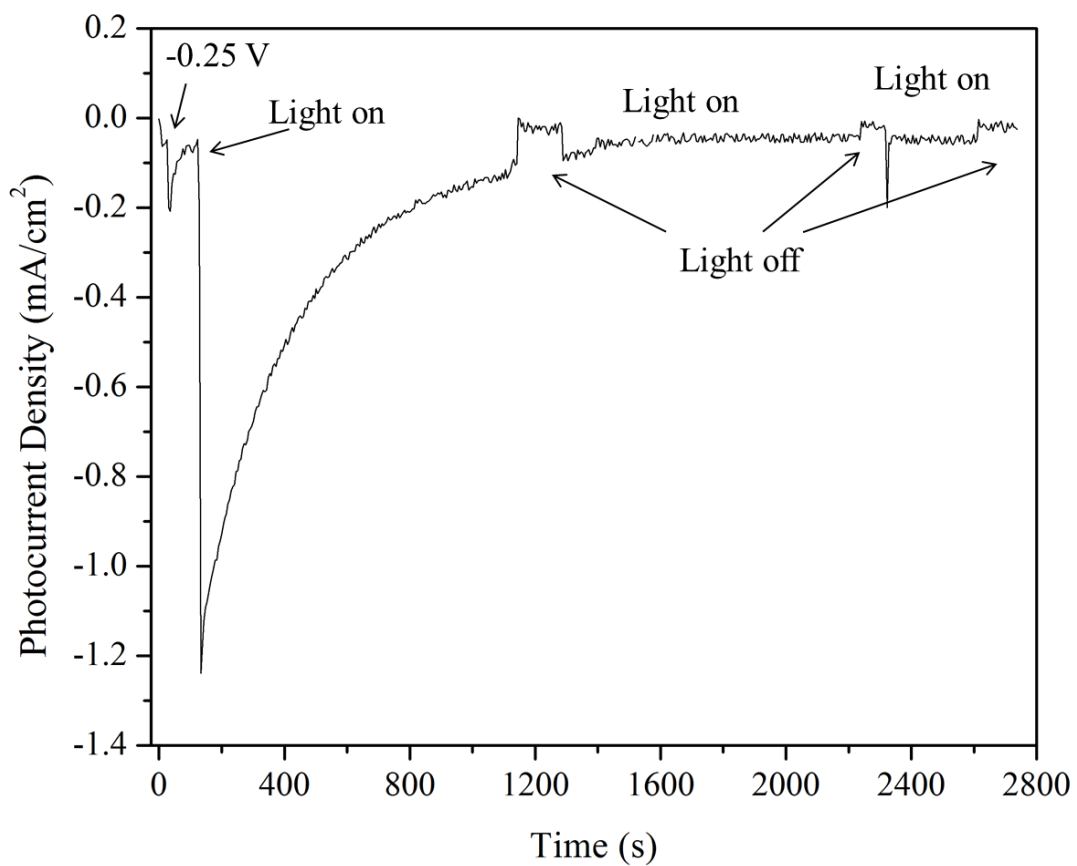


Figure 2.S6. Chronoamperometry for the $\text{Cu}_5\text{Ta}_{11}\text{O}_{30}$ sample analyzed by XPS.

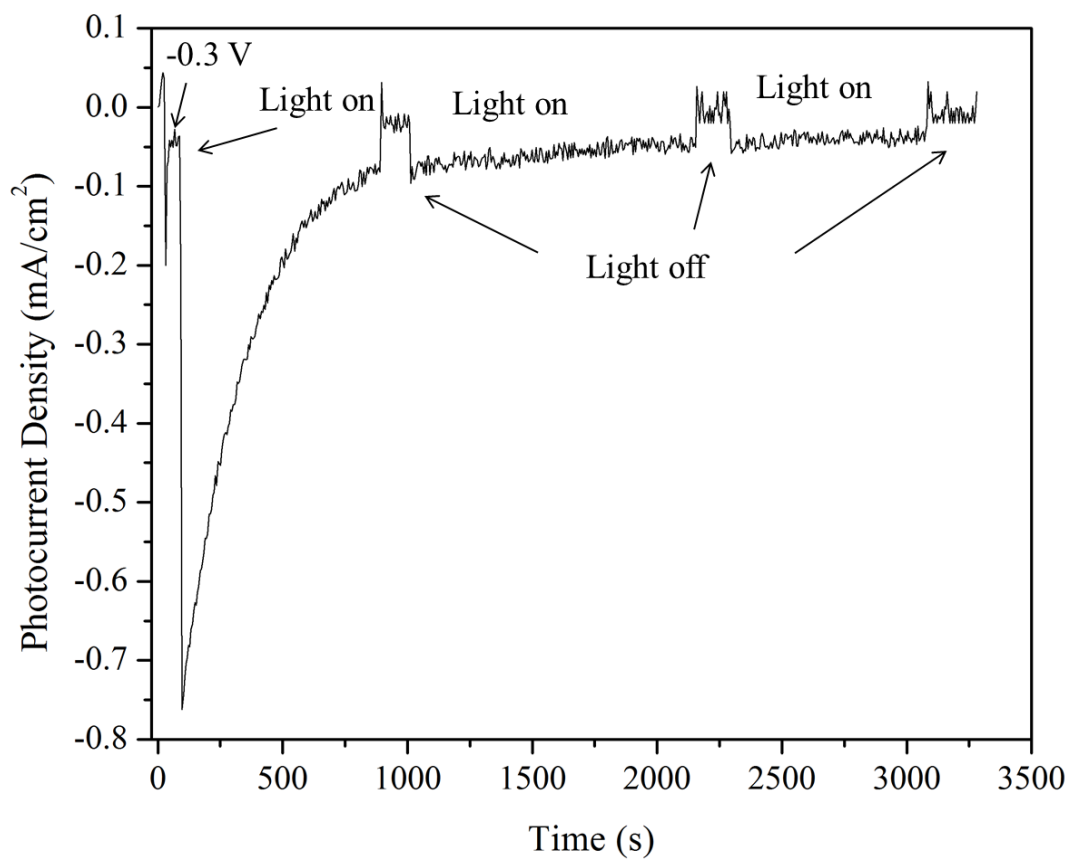


Figure 2.S7. Chronoamperometry for the $\text{Cu}_3\text{Ta}_7\text{O}_{19}$ sample analyzed by XPS.

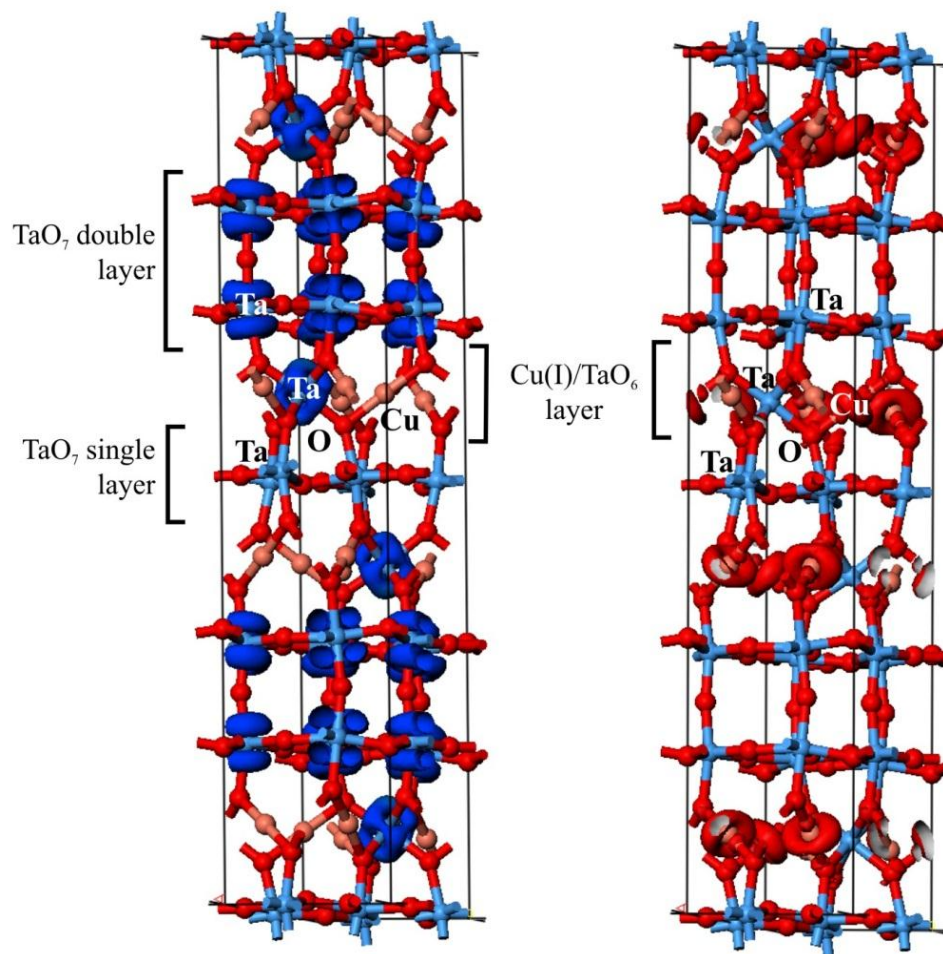


Figure 2.S8. Electron-density plots from the calculated electronic structures of $\text{Cu}_5\text{Ta}_{11}\text{O}_{30}$ for the lowest-energy states (blue electron density; unfilled) in the conduction band (on left) and the highest-energy states (red electron density; filled) in the valence band (on right). The “[“ brackets label the three different types of tantalate layers.

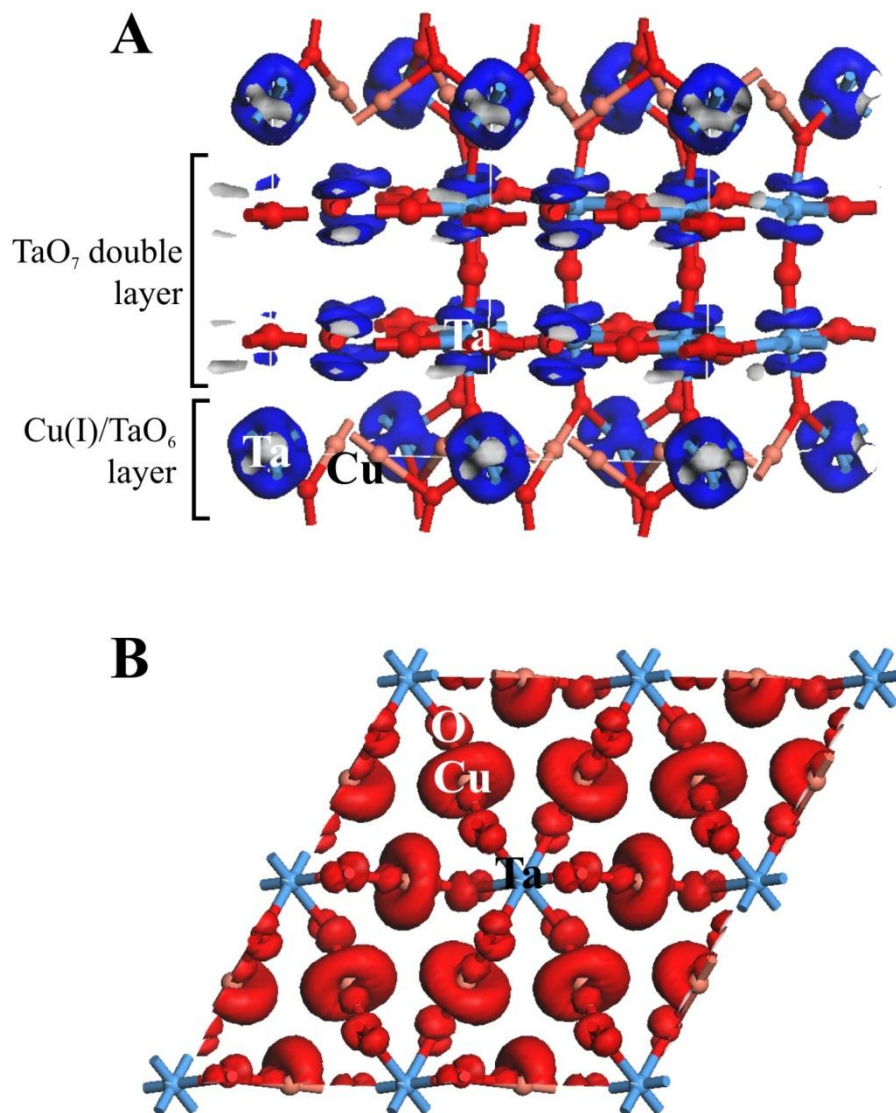


Figure 2.S9. Electron-density plots from the calculated electronic structures of Cu₃Ta₇O₁₉ for the lowest-energy states (blue electron density; unfilled) in the conduction band (A) and the highest-energy states (red electron density; filled) in the valence band (B) for just the Cu(I)/TaO₆ layer. The “[[” brackets label the three different types of tantalate layers.

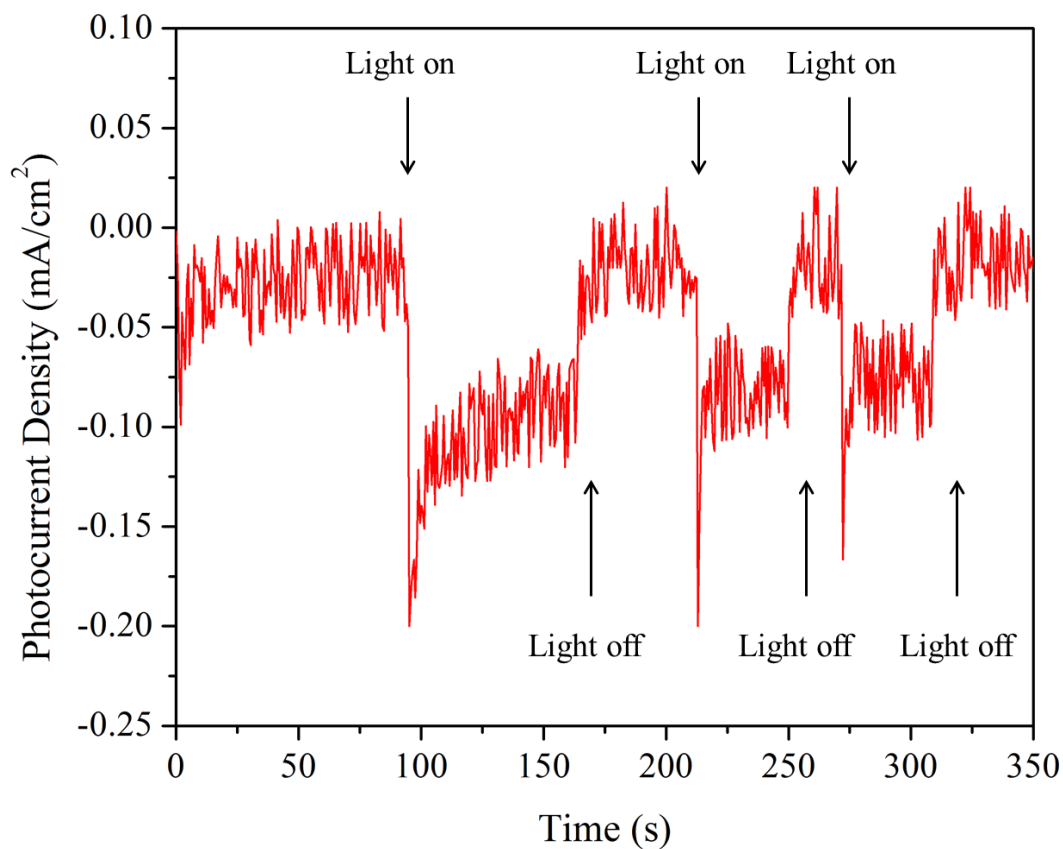


Figure 2.S10. Chronoamperometric measurements in aqueous 0.5 M Na₂SO₄ solution (pH = 6.3) for Cu₅Ta₁₁O₃₀ films annealed at 500 °C under vacuum and oxidized at 350 °C with zero applied voltage under visible-light illumination.

REFERENCES

- (1) Abe, R. *Photochemistry Reviews* **2010**, 11, 179.
- (2) Rajeshwar, K. *J Appl Electrochem* **2007**, 37, 765.
- (3) Fujishima, A.; Honda, K. *Nature* **1972**, 315.
- (4) Aroutiounian, V. M.; Arakelyan, V. M.; Shahnazaryan, G. E. *Solar Energy* **2005**, 581.
- (5) Kennedy, J. H.; Frese, K. W. J. *Electrochem. Soc.* **1978**, 125, 709.
- (6) Sayama, K.; Nomura, A.; Zou, Z.; Aby, R.; Abe, Y.; Arakawa, H. *Chem. Commun.* **2003**, 2908.
- (7) Hodes, G.; Cahen, D.; Manassen, J. *Nature* **1976**, 260, 312.
- (8) Shintaro, I.; Yamada, K.; Matsunaga, T.; Hagiwara, H.; Matsumoto, Y.; Ishihara, T. *J. Am. Chem. Soc.* **2010**, 132, 17343.
- (9) Hara, M.; Konda, T.; Komoda, M.; Ikeda, S.; Shinohara, K.; Tanaka, A.; Konda, J. N.; Domen, K. *Chem. Commun.* **1998**.
- (10) Ingler, W. B.; Baltrus, J. P.; Khan, S. U. M. *J. Am. Chem. Soc.* **2004**, 126, 10238.
- (11) Leygraf, C.; Hendewerk, M.; Somorjal, G. A. *J. Phys. Chem.* **1982**, 86, 4484.
- (12) Joshi, U.; Palasyuk, A. M.; Maggard, P. A. *J. Phys. Chem. C* **2011**, 115, 13534.
- (13) Palasyuk, O.; Palasyuk, A. M.; Maggard, P. A. *J. Solid St. Chem.* **2010**, 183, 814.
- (14) Palasyuk, O.; Palasyuk, A.; Maggard, P. A. *Inorg. Chem.* **2010**, 49, 10571.
- (15) Joshi, U. A.; Palasyuk, A.; Arney, D.; Maggard, P. A. *J. Phys. Chem. Lett.* **2010**, 1, 2719.
- (16) Li, G.; T., K.; Wang; D.; Zou, Z.; Ye, J. *J. Phys. Chem. Sol.* **2008**, 69, 2487.

- (17) MDI In Jade 9; Materials Data Incorporated: **2009**.
- (18) Jahnberg, L. *Acta Chem. Scand. A.*, **1987**, 41, 527.
- (19) Kubelka, P.; Munk, F. Z., *Tech. Physik.* **1931**, 12, 593.
- (20) Clark, S. J.; Segall, M. D.; Pickard, C. J.; Hasnip, P. J.; Probert, M. J.; Refson, K.; Payne, M. C., *Z. Kristallogr.* **2005**, 220, 567.
- (21) Payne, M. C.; Teter, M. P.; Allan, D. C.; Arias, T. A.; Joannopoulos, J. D. *Rev. Mod. Phys.* **1992**, 64, 1045.
- (22) Monkhorst, H.J.; Pack, J.D. *Phys. Rev. B* **1976**, 13, 5188.
- (23) Larson, P. E. J. *Electron Spectrosc. Relat. Phenom.* **1974**, 4, 213.
- (24) Haber, J., Machej, T., Ungier, L., Ziolkowski J. *J. Solid St. Chem.* **1978**, 25, 207.
- (25) Gomes, W.P.; Cardon, F. *Prog. Surf. Sci.* **1982**, 12, 155.
- (26) *Metal Oxides: Chemistry and Applications* (Ed. Fierro, J.L.G.; Ch. 6) Woodward, P. CRC Press: Boca Raton, FL, **2006**.
- (27) Garlea, O.; Darie, C.; Bougerol, C.; Isnard, O.; Bordet, P. *Solid St. Sci.* **2003**, 5, 1095.

CHAPTER 3

The Effect of Oxidation on the Structural Properties of *p*-type CuNbO_3 , CuNb_3O_8 , $\text{Cu}_5\text{Ta}_{11}\text{O}_{30}$ and $\text{Cu}_3\text{Ta}_7\text{O}_{19}$.

Lindsay Fuoco, Prangya P. Sahoo, Nacole King and Paul A. Maggard

INTRODUCTION

The renewable production of fuels from sunlight has generated intense research over the past few decades in the field of semiconducting photoelectrodes, especially in the development of photoelectrodes capable of utilizing visible-light, a significant fraction of the solar spectrum. The use of metal oxides as photoelectrodes is particularly attractive owing to their higher inherent stability against photocorrosion. However, metal oxides often exhibit large bandgap sizes that restrict their use to only ultraviolet energies, such as in *n*-type TiO_2 . Just a few examples of *p*-type semiconducting oxides that function as photocathodes under visible-light irradiation have been discovered so far, including Cu_2O , CaFe_2O_4 , and metal-ion doped Fe_2O_3 .²⁻⁶ Our research efforts in the area have focused on the reduction of bandgap sizes via the use of Nb(V) or Ta(V) cations (empty d^0 -orbitals) that form the conduction band states in early transition-metal oxides, together with a Cu(I) cation (filled d^{10} -orbitals) that can form higher energy valence-band states.⁷⁻¹⁰ For example, the isoelectronic substitution of Cu(I) for the Na cation in the NaNbO_3 photocatalyst decreases its bandgap size from ~ 3.4 eV

to ~2.0 eV via the creation of a new higher-energy valence band consisting of the filled Cu d^{10} orbitals, as found in CuNbO_3 .^{7,11}

Recently, we reported the preparation of four new *p*-type semiconducting photoelectrodes, i.e. CuNbO_3 , CuNb_3O_8 , $\text{Cu}_5\text{Ta}_{11}\text{O}_{30}$ and $\text{Cu}_3\text{Ta}_7\text{O}_{19}$ that exhibit bandgap sizes of 2.0 eV, 1.47 eV, 2.59 eV and 2.47 eV respectively.^{1,6} An example of the photocathodic current observed in each is shown in Figures 3.1-3.4. A mild oxidation of both of the Cu(I) tantalate phases results in an increase in their cathodic currents.⁶ Similarly, oxidation of CuNbO_3 was also shown to result in an increase in photocathodic currents.¹⁰ However, it is still unknown as to how the oxidation affects the composition and structure. Described herein is a preliminary investigation into the controlled oxidation of CuNbO_3 , CuNb_3O_8 , $\text{Cu}_5\text{Ta}_{11}\text{O}_{30}$ and $\text{Cu}_3\text{Ta}_7\text{O}_{19}$ by powder X-ray diffraction in order to probe the overall structural changes undergone in each structure and to provide a further understanding of its effects on their photoelectrochemical properties.

EXPERIMENTAL

The syntheses of $\text{Cu}_5\text{Ta}_{11}\text{O}_{30}$ and $\text{Cu}_3\text{Ta}_7\text{O}_{19}$ were performed by a molten-salt flux method using CuCl as the flux. Stoichiometric mixtures of reagent grade Ta_2O_5 (Alfa Aesar, min. 99.99%) or Nb_2O_5 (Alfa Aesar 99.998%) and Cu_2O (Alfa Aesar, min. 99.9%) were combined with CuCl (Alfa Aesar, min 99%) at a 10:1 molar ratio (flux:product) in a glovebox with an Argon atmosphere. The reactant mixtures were ground together, loaded into fused silica ampules, and flame sealed on a vacuum line. The reaction vessels were heated to 900 °C for $\text{Cu}_5\text{Ta}_{11}\text{O}_{30}$ and 700 °C for $\text{Cu}_3\text{Ta}_7\text{O}_{19}$ for 24 h, and allowed to

radiatively cool in the furnaces. The CuNb_3O_8 reaction was heated at 750 °C for 20 minutes and quenched. The resulting products were washed with 3M NH_4OH to remove the CuCl flux. The synthesis of CuNbO_3 was performed using excess Cu_2O as a flux. A 1.5:1 molar ratio of $\text{Cu}_2\text{O}:\text{Nb}_2\text{O}_5$ was ground together using a mortar and pestle in a glovebox with an Argon atmosphere for 30 minutes and flame sealed into a fused silica reaction vessel on a vacuum line. The vessel was heated at 900 °C for 48 h and allowed to radiatively cool in the furnace. The resulting product was washed with a 5 M NH_4OH to remove excess Cu_2O . Approximately 80 mg of each sample was then oxidized at 250 °C, 350 °C or 450 °C for 3 h in open air and allowed to radiatively cool.

Characterization. Solid-state products were characterized by high resolution powder X-ray diffraction (PXRD) on a Rigaku R-axis Spider diffractometer using $\text{Cu K}\alpha_1$ ($\lambda = 1.54056 \text{ \AA}$) radiation from a sealed-tube X-ray generator equipped with a curved image-plate detector. UV-Vis diffuse reflectance spectra were collected on a Shimadzu UV-3600 equipped with an integrating sphere. Pressed barium sulfate powder was used as a reference and the data were plotted as the remission function $F(R_\infty) = (1 - R_\infty)^2 / (2R_\infty)$, where R is diffuse reflectance based on the Kubelka-Munk theory of diffuse reflectance.¹²

Photoelectrochemical measurements were carried out in a Teflon cell with the $\text{Cu}_5\text{Ta}_{11}\text{O}_{30}$, $\text{Cu}_3\text{Ta}_7\text{O}_{19}$, CuNbO_3 or CuNb_3O_8 polycrystalline film as the working electrode, Pt foil as the counter electrode, and a standard calomel reference electrode (SCE). Films were immersed in a 0.5 M Na_2SO_4 electrolyte solution that was adjusted to a pH of ~6.3 using dilute H_2SO_4 (aq). The cell was purged with argon gas 30 minutes prior to and during all

measurements. An electrochemical analyzer (Princeton Applied Research, PARSTAT 2263) with PowerSuite software was used to measure photocurrent.

RESULTS AND DISCUSSION

$\text{Cu}_5\text{Ta}_{11}\text{O}_{30}$ and $\text{Cu}_3\text{Ta}_7\text{O}_{19}$ crystallize in a hexagonal structure with space groups $P6_2c$ and $P6_3/m$ such as shown in Figure 3.5. Both CuNbO_3 and CuNb_3O_8 crystallize in monoclinic structures with space groups $C2/m$ and $P2_1/c$ respectively and are shown in Figure 3.6. The bulk non-oxidized polycrystalline powders of CuNbO_3 , CuNb_3O_8 , $\text{Cu}_5\text{Ta}_{11}\text{O}_{30}$ and $\text{Cu}_3\text{Ta}_7\text{O}_{19}$ were prepared in high purity according to their powder X-ray diffraction (PXRD) patterns and are shown in Figure 3.7A, Figure 3.8A, Figure 3.9A and Figure 3.10 A respectively. Each diffraction peak could be indexed to the theoretical patterns, and the lattice constants were refined to the expected values for their reported crystal structures, listed in Table 3.1.^{8,13}

The UV-Vis diffuse reflectance spectra are shown in Figures 3.15 and 3.16 for both oxidized and non-oxidized films $\text{Cu}_5\text{Ta}_{11}\text{O}_{30}$ and $\text{Cu}_3\text{Ta}_7\text{O}_{19}$. The optical absorption edges of the non-oxidized films were sharp and clearly defined, consistent with previous reports of their bandgap sizes of ~2.0 eV, ~1.47 eV, ~2.59 eV and ~2.47 eV. However, oxidation of the $\text{Cu}_5\text{Ta}_{11}\text{O}_{30}$ and $\text{Cu}_5\text{Ta}_{11}\text{O}_{30}$ films at temperatures of 350 °C or greater results in the disappearance of a defined absorption edge and instead a broad diffuse reflectivity that is more characteristic of a degenerate semiconductor.

The PXRD patterns for the oxidation of each at 250 °C, 350 °C and 450 °C are shown in Figures 3.7-3.10. Both CuNb_3O_8 and $\text{Cu}_5\text{Ta}_{11}\text{O}_{30}$ phases were stable under all oxidation

conditions and no additional impurity phases were observed. However, the complete decomposition of CuNbO_3 was observed at 450 °C and evidence of decomposition in $\text{Cu}_3\text{Ta}_7\text{O}_{19}$ as peak broadening is also observed. The lattice constants for CuNbO_3 , CuNb_3O_8 , $\text{Cu}_5\text{Ta}_{11}\text{O}_{30}$ and $\text{Cu}_3\text{Ta}_7\text{O}_{19}$ samples with and without oxidation treatments from 250-450 °C were refined and are listed in Table 3.1. For CuNbO_3 , all lattice parameters show a linear decrease with increasing oxidation temperatures as shown in Figure 3.11. A similar trend was observed for CuNb_3O_8 of a general decrease in lattice constants with increasing oxidation temperature (Figure 3.12). In the case of $\text{Cu}_5\text{Ta}_{11}\text{O}_{30}$ and $\text{Cu}_3\text{Ta}_7\text{O}_{19}$, the a lattice constant was found to increase with increasing oxidation temperatures while c lattice parameter was found to decrease and is shown in Figures 3.13 and 3.14. Further investigation into the effects of oxidation is in progress via the collection of high resolution PXRD spectra and a full Rietveld refinement of the atomic positions.

CONCLUSIONS

Microcrystalline powders of CuNbO_3 , CuNb_3O_8 , $\text{Cu}_5\text{Ta}_{11}\text{O}_{30}$, and $\text{Cu}_3\text{Ta}_7\text{O}_{19}$ could be prepared in either a CuCl or Cu_2O flux in high purity. Samples were oxidized at 250 °C, 350 °C, and 450 °C and characterized by Powder X-ray diffraction. Refined lattice parameters for CuNbO_3 and CuNb_3O_8 were found to decrease with increasing oxidation temperatures. For, $\text{Cu}_5\text{Ta}_{11}\text{O}_{30}$ and $\text{Cu}_3\text{Ta}_7\text{O}_{19}$, the a lattice constant was found to increase with increasing oxidation temperatures while c lattice parameter was found to decrease. Further investigation into the effects of oxidation on CuNbO_3 , CuNb_3O_8 , $\text{Cu}_5\text{Ta}_{11}\text{O}_{30}$, and $\text{Cu}_3\text{Ta}_7\text{O}_{19}$ is currently in progress.

Table 3.1. Lattice parameters for CuNbO_3 , CuNb_3O_8 , $\text{Cu}_5\text{Ta}_{11}\text{O}_{30}$ and $\text{Cu}_3\text{Ta}_7\text{O}_{19}$ calculated from the PXRD.

Sample		$a(\text{\AA})$	$b(\text{\AA})$	$c(\text{\AA})$	$V(\text{\AA}^3)$
CuNbO_3	RT	9.489301(2)	8.433746(6)	6.765217(2)	541.3772(4)
	C2/m				
	250 °C	9.481757(6)	8.430655(8)	6.761132(10)	539.5992(10)
	350 °C	9.468114(3)	8.427990(8)	6.752099(5)	538.7274(7)
CuNb_3O_8	RT	15.35414(5)	5.069345(2)	7.530019(2)	560.2178(19)
	P2 ₁ /c				
	250 °C	15.34222(10)	5.068348(8)	7.533133(6)	560.070(5)
	350 °C	15.34089(4)	5.06442(3)	7.528267(4)	559.205(4)
	450 °C	15.34744(1)	5.069588(10)	7.524248(7)	559.527(6)
$\text{Cu}_3\text{Ta}_7\text{O}_{19}$	RT	6.232442(2)	-----	20.15926(3)	678.1436(11)
	P6 ₃ /m				
	250 °C	6.238174(2)	-----	20.14164(11)	678.7977(11)
	350 °C	6.246716(8)	-----	20.088499(10)	678.8622(13)
	450 °C	6.262435(2)	-----	20.103100(10)	682.7788(5)
$\text{Cu}_5\text{Ta}_{11}\text{O}_{30}$	RT	6.2264581(1)	-----	32.53343(2)	1092.3018(7)
	P6 ₂ c				
	250 °C	6.22775(3)	-----	32.52028(5)	1092.312(8)
	350 °C	6.232635(2)	-----	32.445511(10)	1091.5123(6)
	450 °C	6.235188(7)	-----	32.20213(4)	1084.212(2)

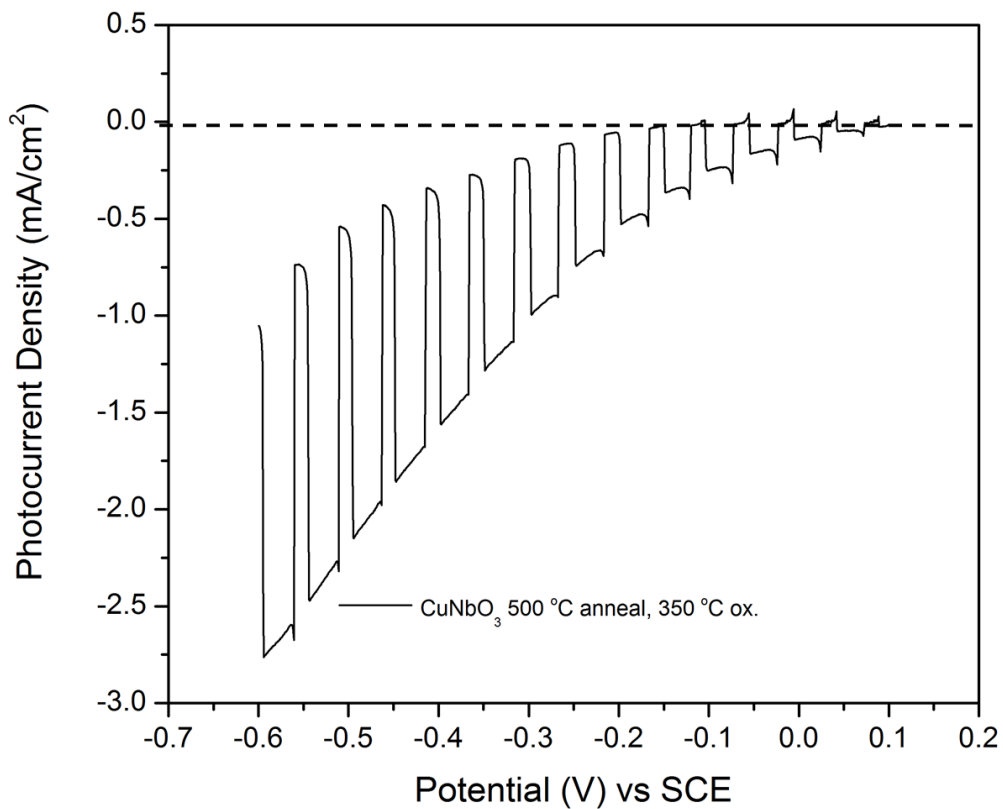


Figure 3.1. Current-potential curves in aqueous 0.5 M Na₂SO₄ solution (pH = 6.3) under chopped visible-light irradiation for a CuNbO₃ film annealed at 500 °C for 3 h and oxidized for 3 h at 350 °C.

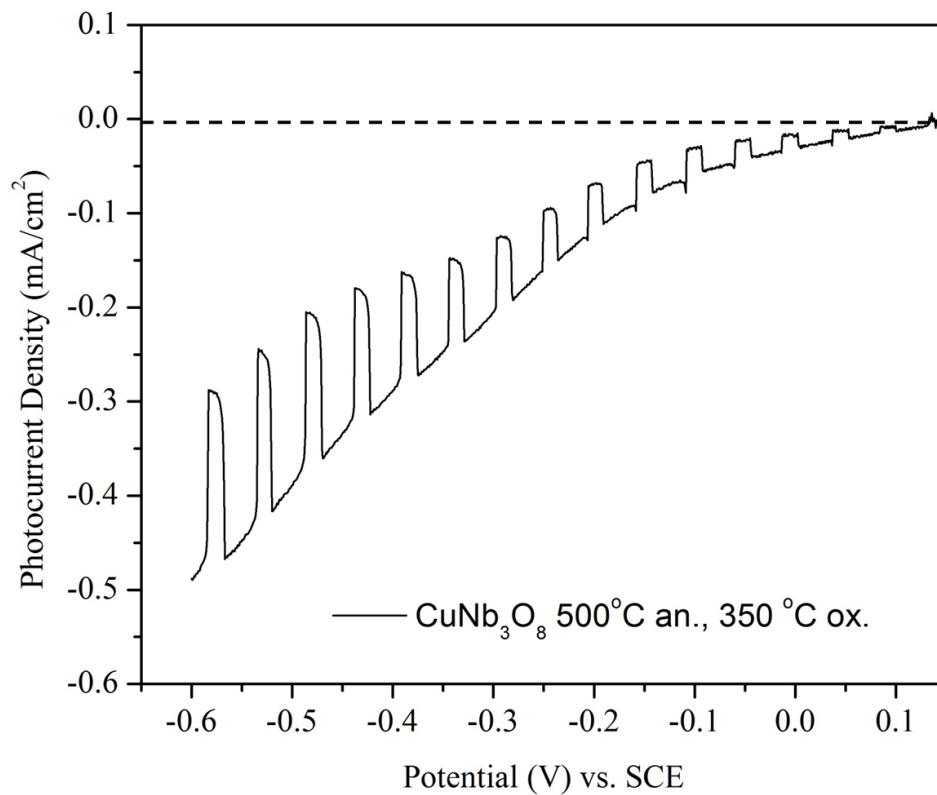


Figure 3.2. Current-potential curves in aqueous 0.5 M Na₂SO₄ solution (pH = 6.3) under chopped visible-light irradiation for a CuNb₃O₈ film annealed at 500 °C for 3 h and oxidized for 3 h at 350 °C.

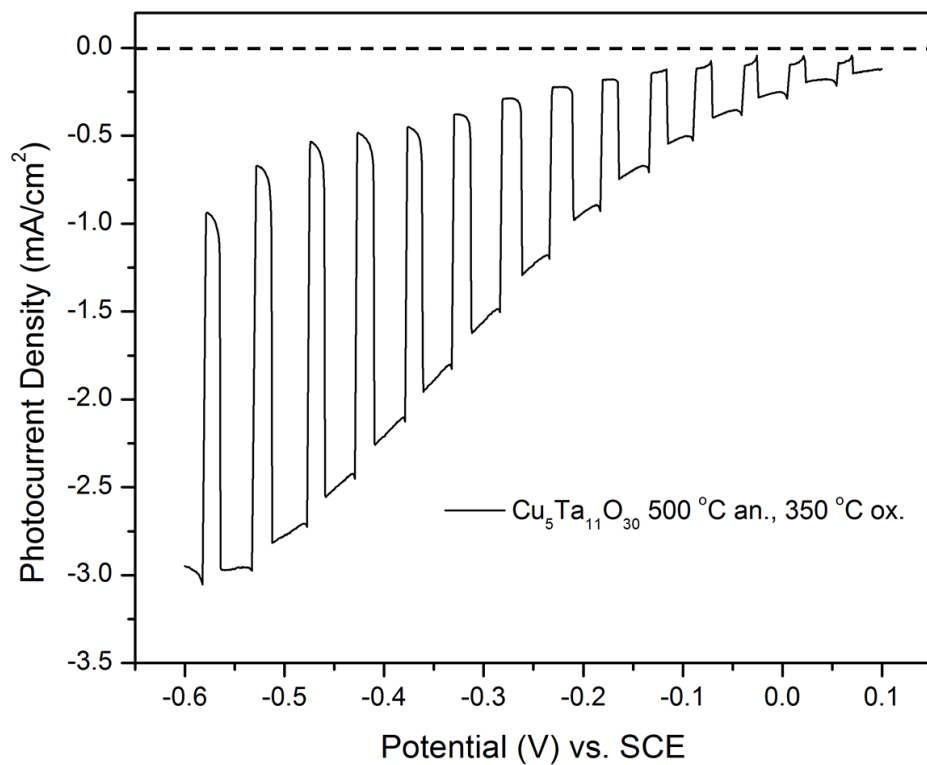


Figure 3.3. Current-potential curves in aqueous 0.5 M Na_2SO_4 solution (pH = 6.3) under chopped visible-light irradiation for a $\text{Cu}_5\text{Ta}_{11}\text{O}_{30}$ film annealed at 500 °C for 3 h and oxidized for 3 h at 350 °C.

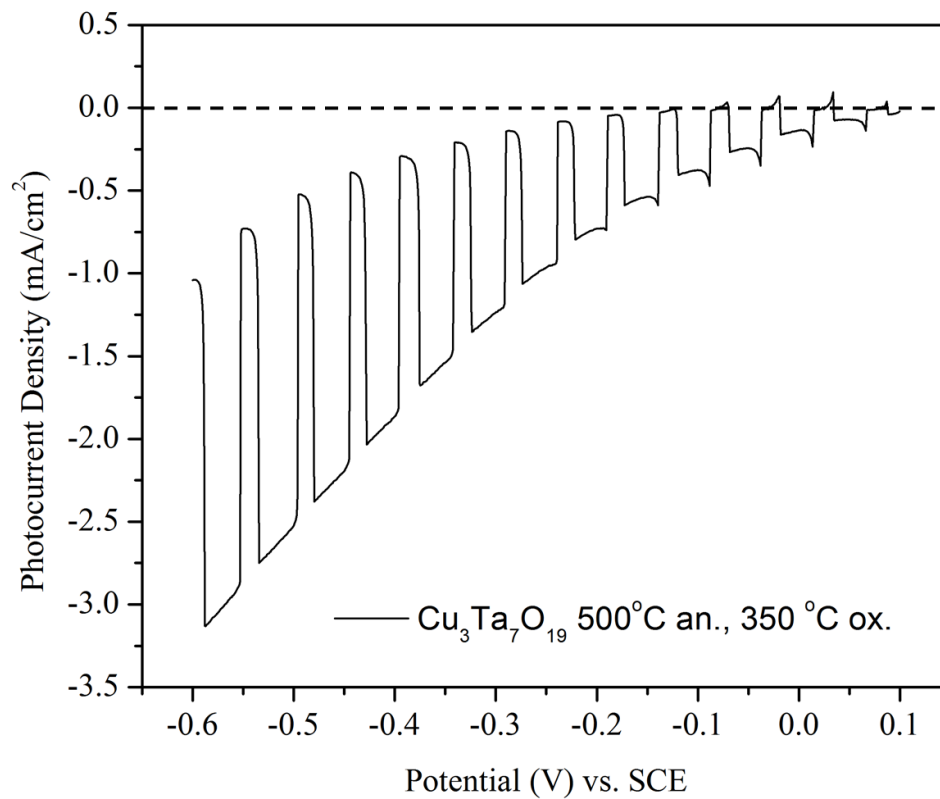


Figure 3.4. Current-potential curves in aqueous 0.5 M Na₂SO₄ solution (pH = 6.3) under chopped visible-light irradiation for a Cu₃Ta₇O₃₀ film annealed at 500 °C for 3 h and oxidized for 3 h at 350 °C.

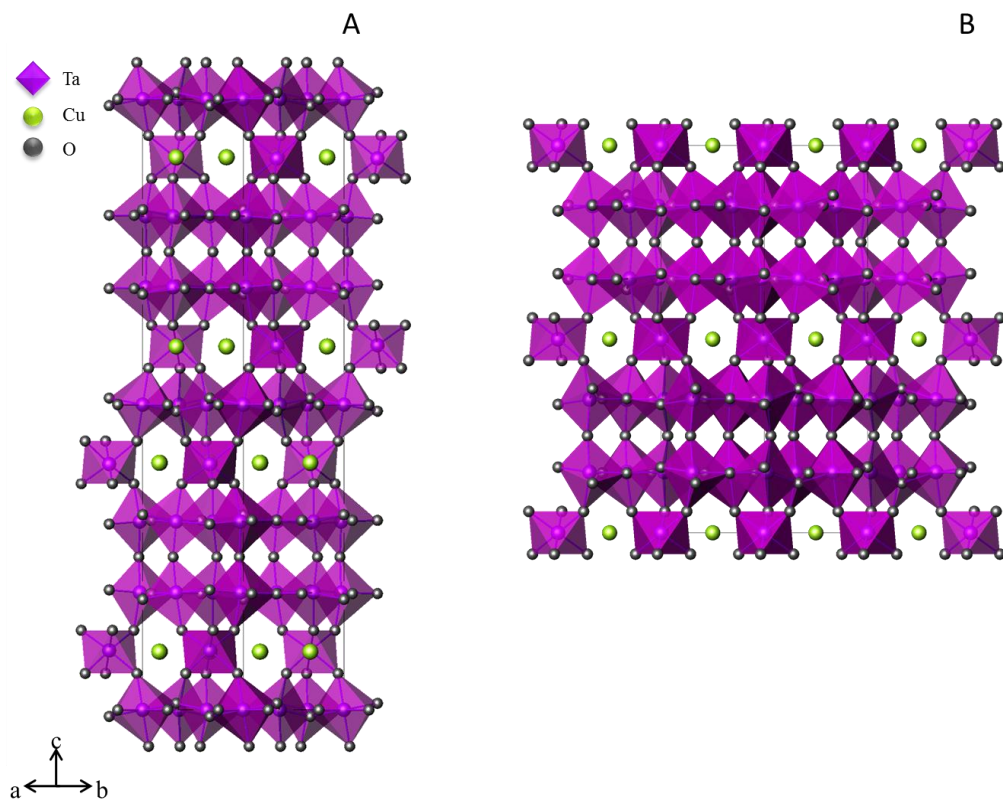


Figure 3.5. Representative drawings of the crystal structures of $\text{Cu}_5\text{Ta}_{11}\text{O}_{30}$ (A) and $\text{Cu}_3\text{Ta}_7\text{O}_{19}$ (B).

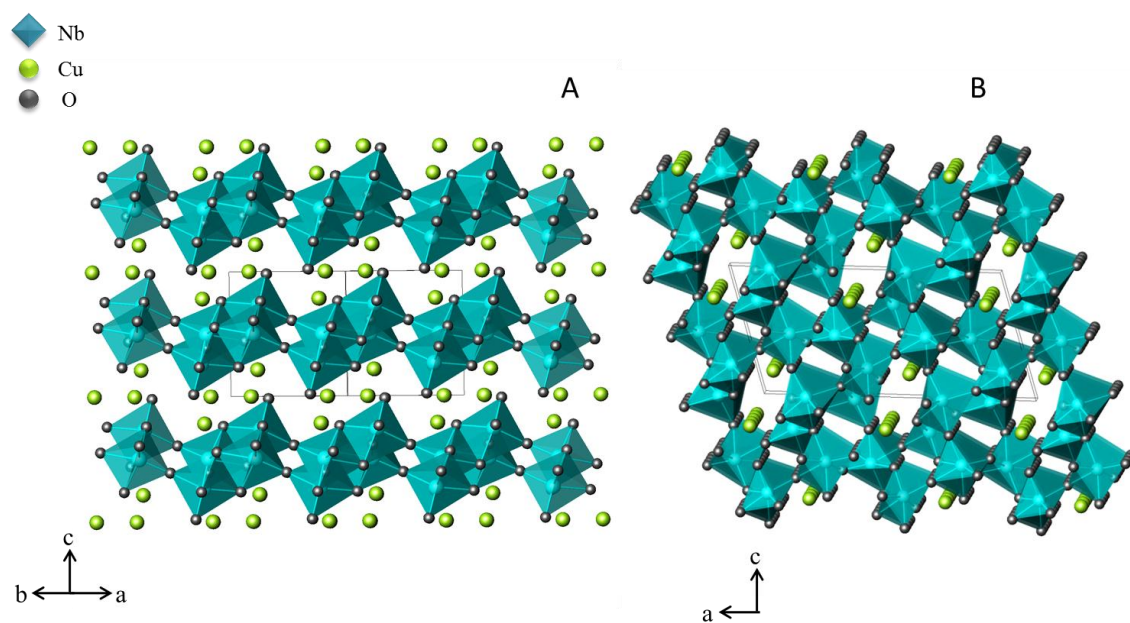


Figure 3.6. Representative drawings of the crystal structures of CuNbO_3 (A) and CuNb_3O_8 (B).

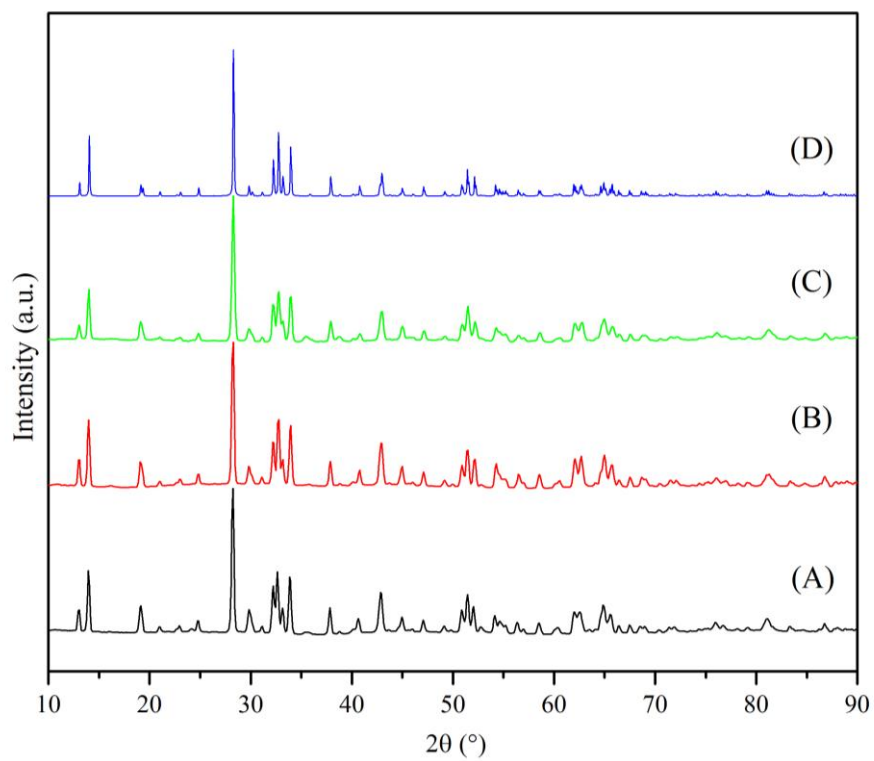


Figure 3.7. PXRD patterns for CuNbO_3 non-oxidized (A), oxidized at 250 °C (B), and 350 °C (C). Also shown is the calculated pattern of CuNbO_3 (D).

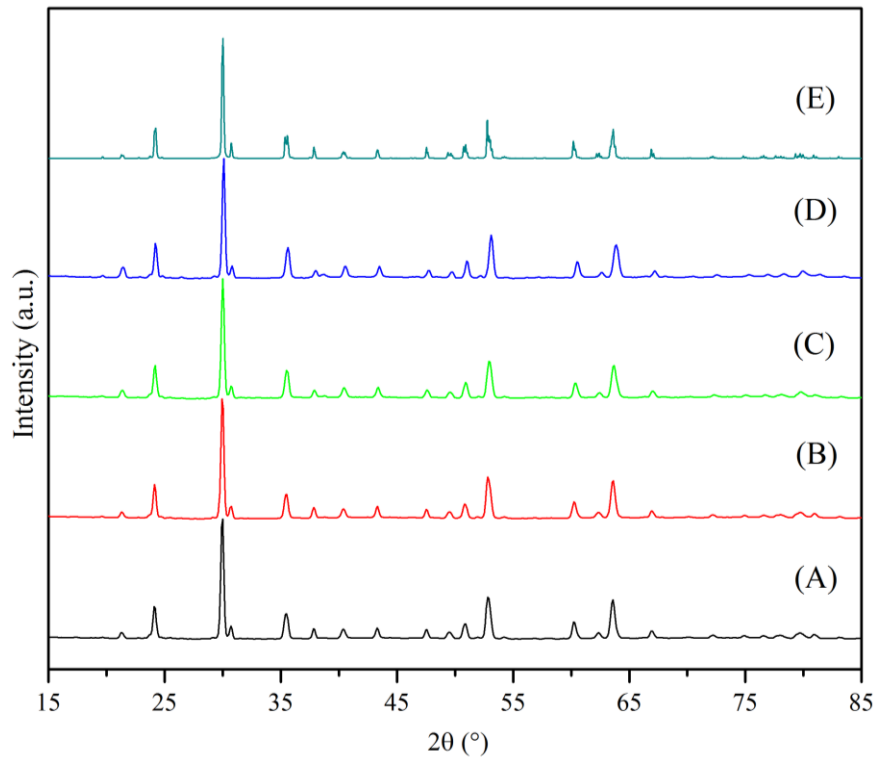


Figure 3.8. PXRD patterns for CuNb₃O₈ non-oxidized (A), oxidized at 250 °C (B), 350 °C (C) and 450 °C (D). Also shown is the calculated pattern for CuNb₃O₈ (E).

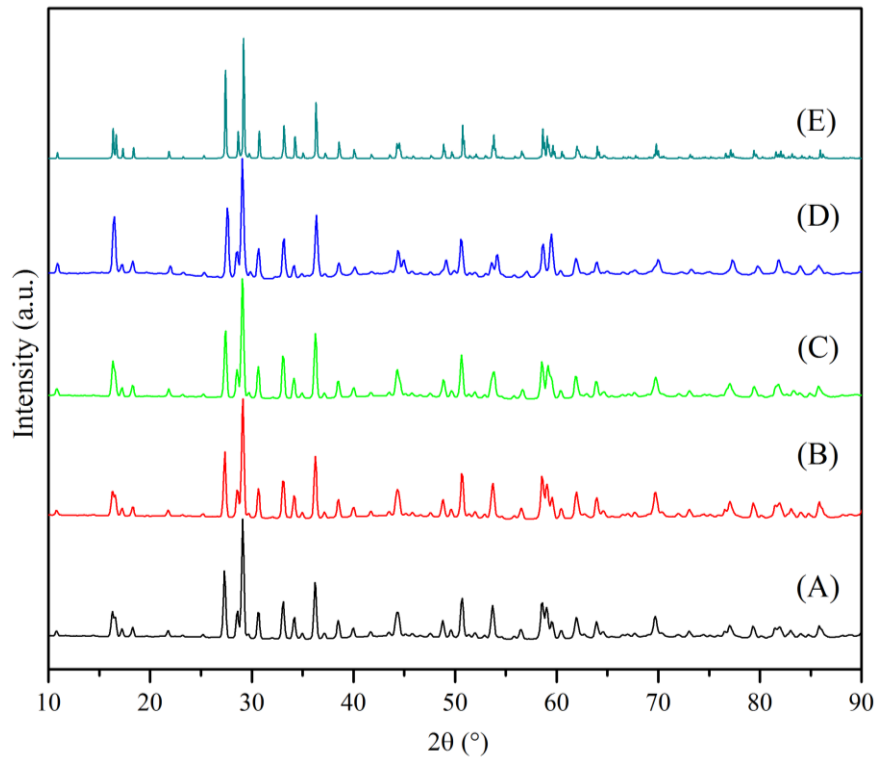


Figure 3.9. PXRD patterns for Cu₅Ta₁₁O₃₀ non-oxidized (A), oxidized at 250 °C (B), 350 °C (C) and 450 °C (D). Also shown is the calculated pattern of Cu₅Ta₁₁O₃₀ (E).

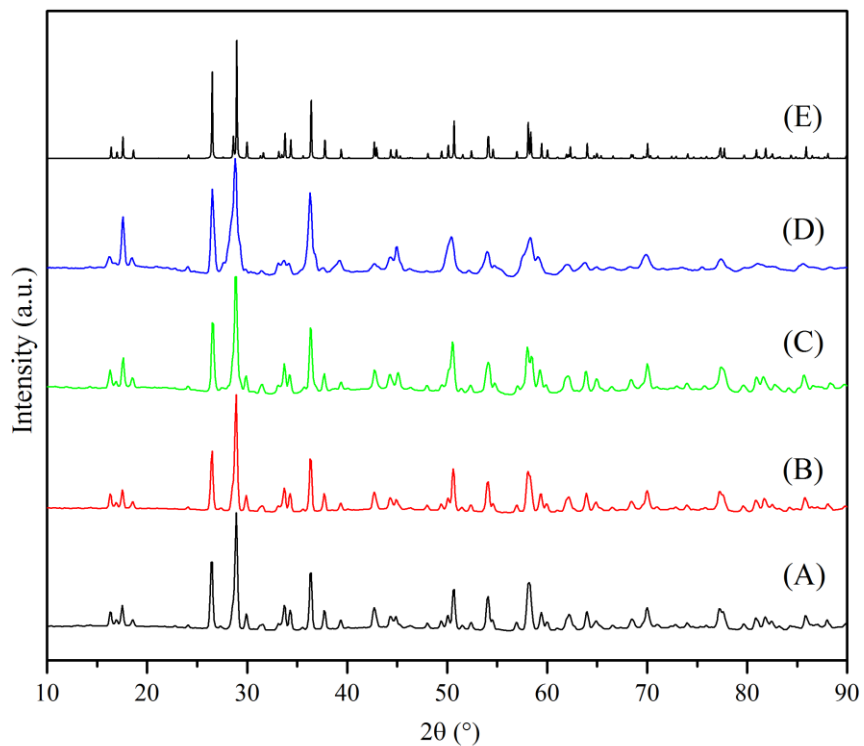


Figure 3.10. PXRD patterns for $\text{Cu}_3\text{Ta}_7\text{O}_{19}$ non-oxidized (A), oxidized at 250 °C (B), 350 °C (C) and 450 °C (D). Also shown is the calculated pattern of $\text{Cu}_3\text{Ta}_7\text{O}_{19}$ (E).

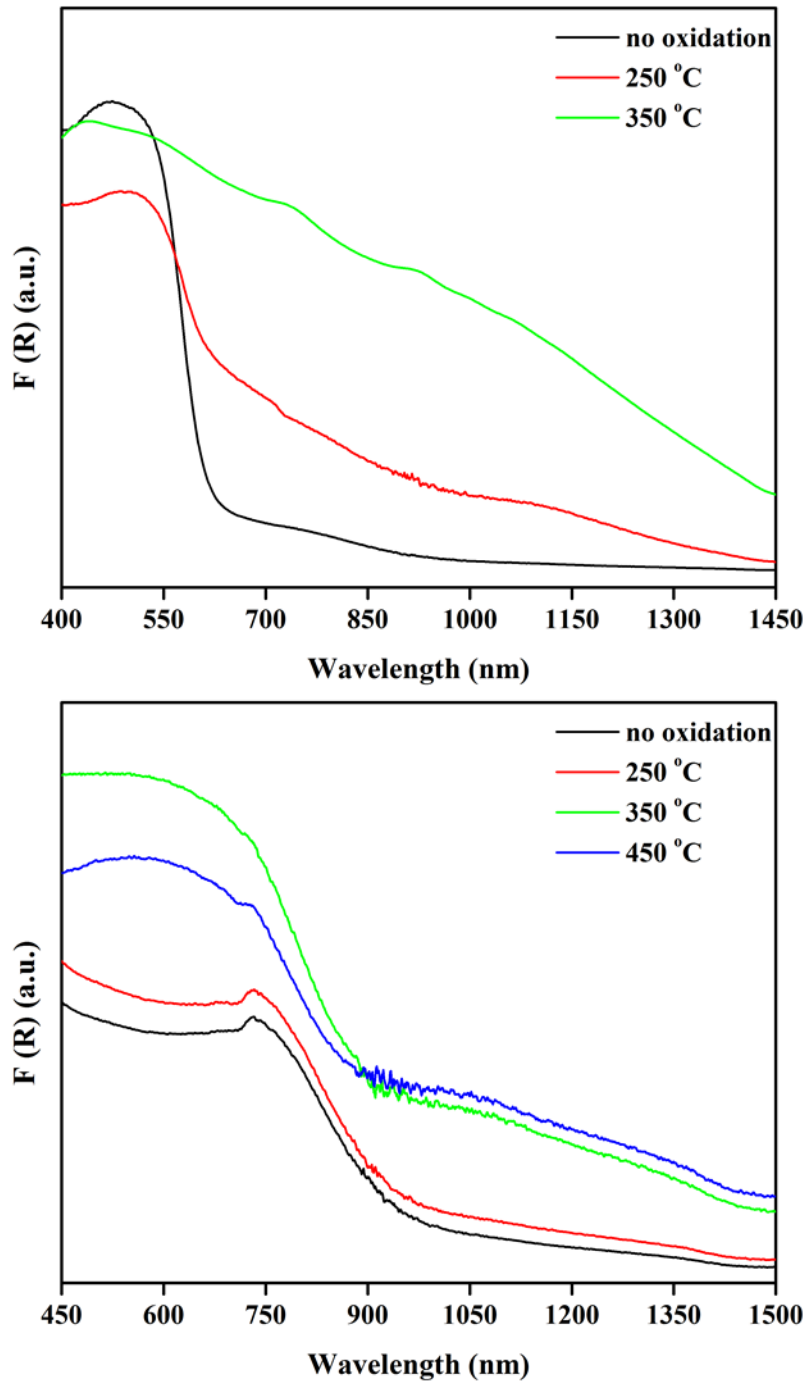


Figure 3.11. UV-Vis diffuse reflectance spectra for (upper plot) CuNbO_3 with no oxidation and oxidized for 3 h at 250 °C and 350 °C, and (lower plot) CuNb_3O_8 with no oxidation and oxidized for 3 h at 250 °C, 350 °C and 450 °C.

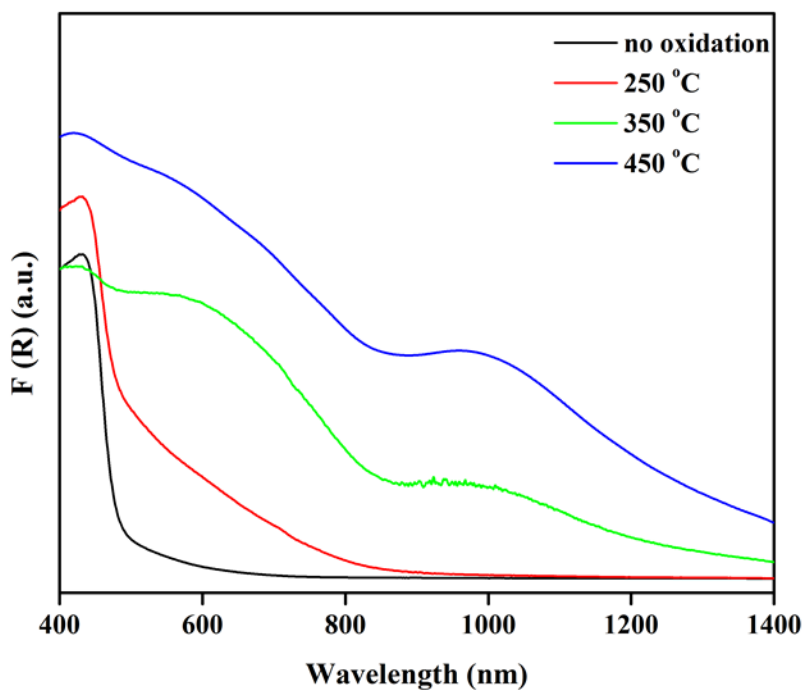
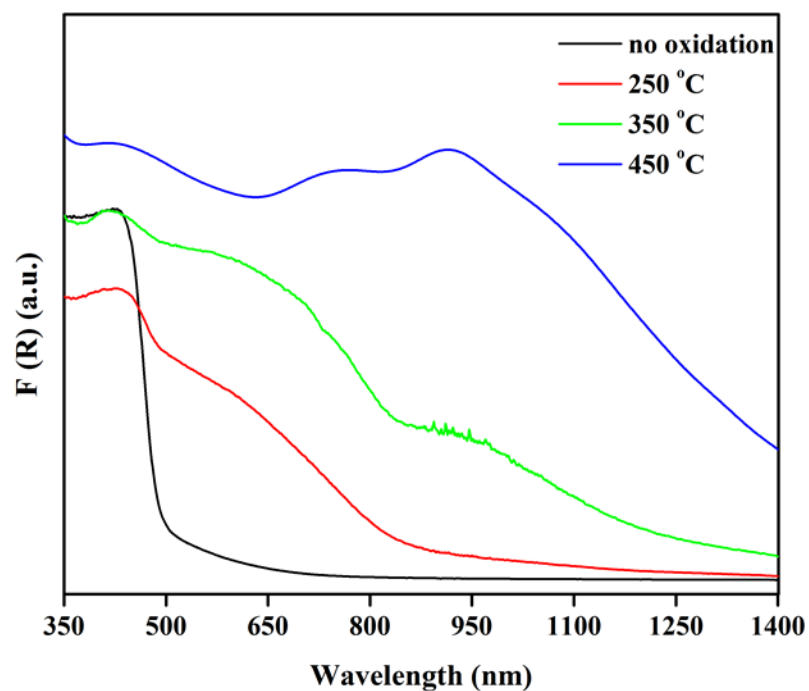


Figure 3.12. UV-Vis diffuse reflectance spectra for (upper plot) $\text{Cu}_3\text{Ta}_7\text{O}_{19}$ with no oxidation and oxidized for 3 h at 250 °C, 350 °C and 450 °C and (lower plot) $\text{Cu}_5\text{Ta}_{11}\text{O}_{30}$ with no oxidation and oxidized for 3 h at 250 °C, 350 °C and 450 °C.

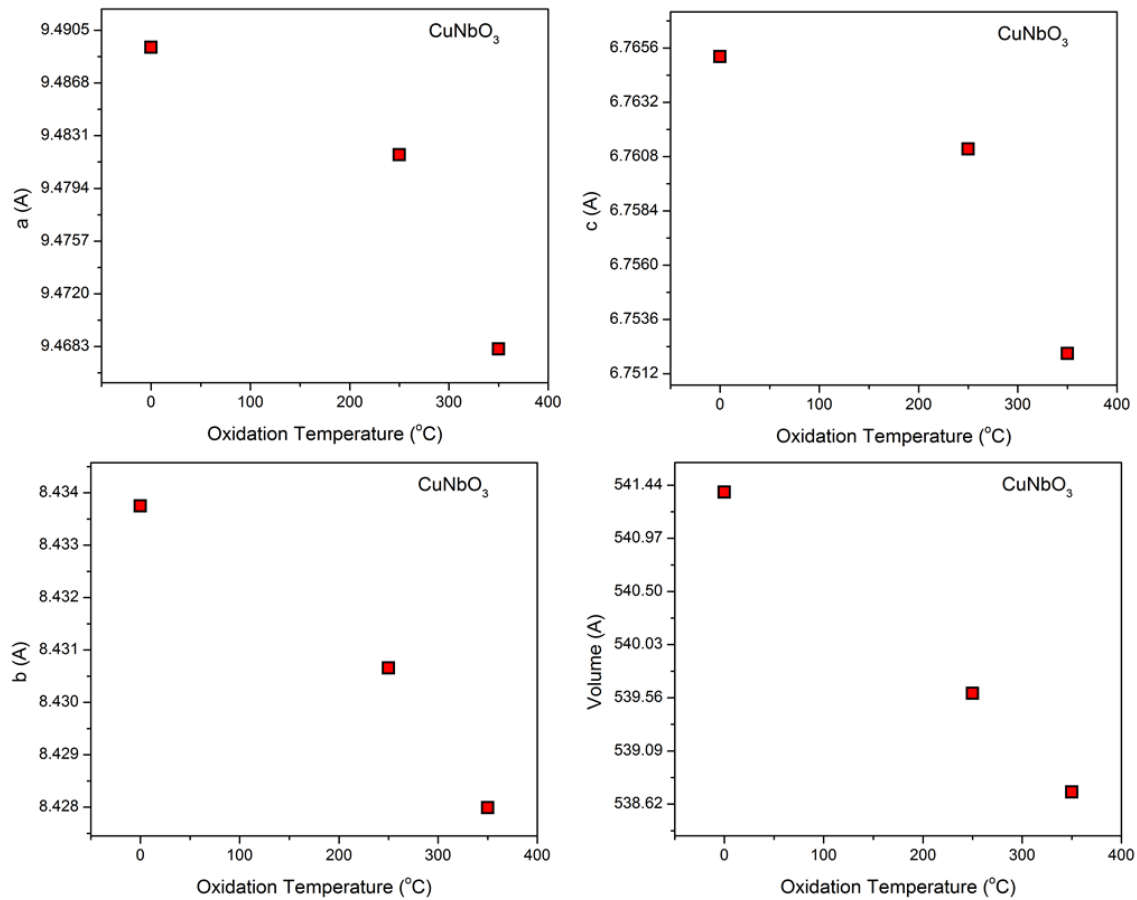


Figure 3.13. Unit cell lattice parameters versus oxidation temperature for CuNbO_3 .

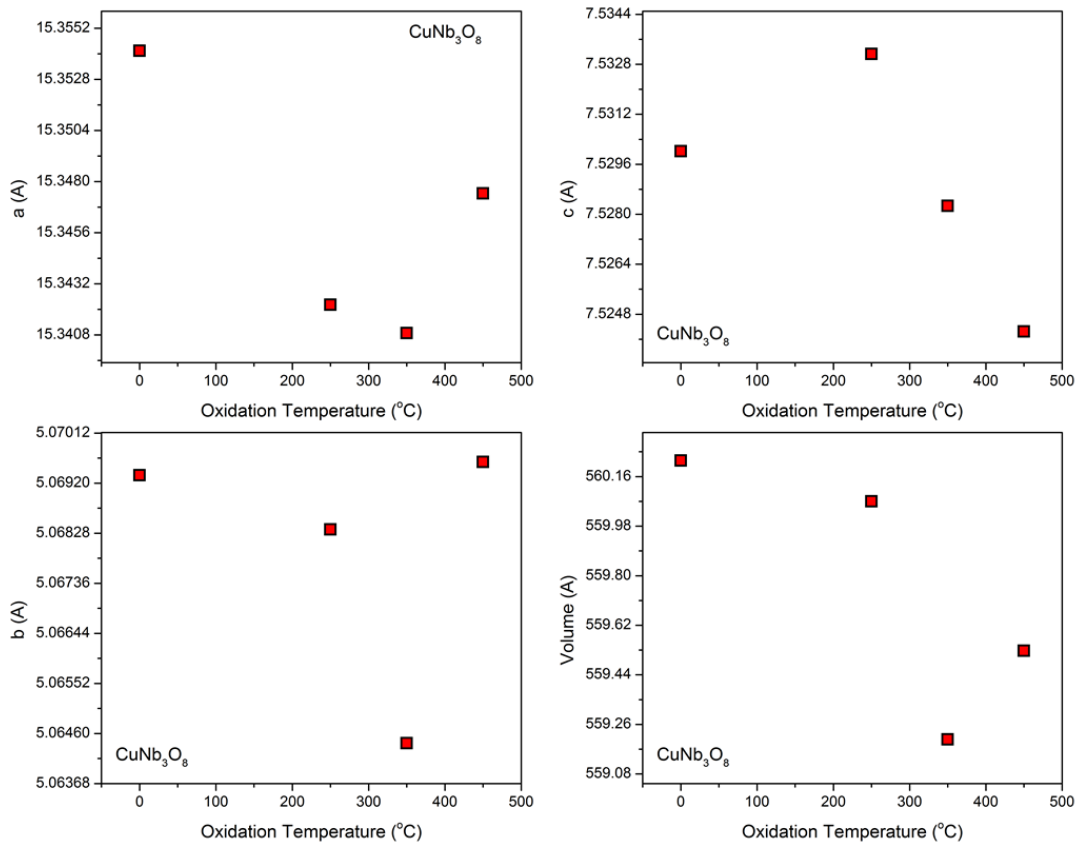


Figure 3.14. Unit cell lattice parameters versus oxidation temperature for CuNb_3O_8 .

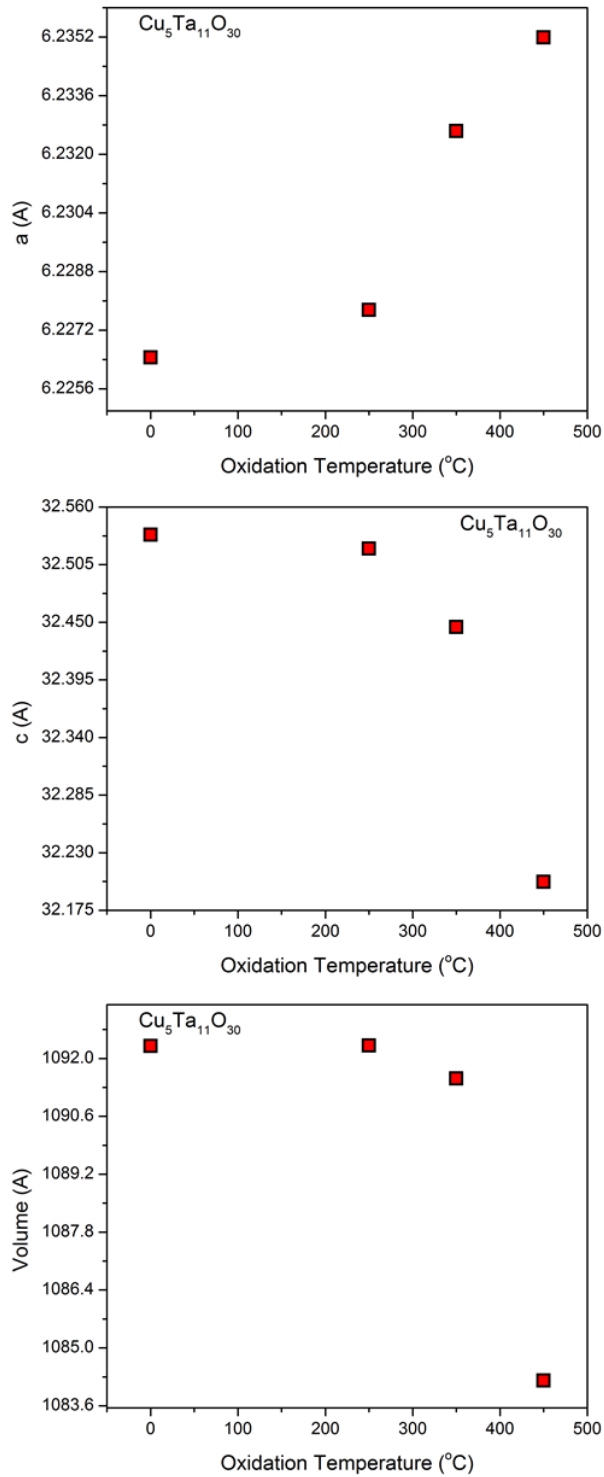


Figure 3.15. Unit cell lattice parameters for $\text{Cu}_5\text{Ta}_{11}\text{O}_{30}$.

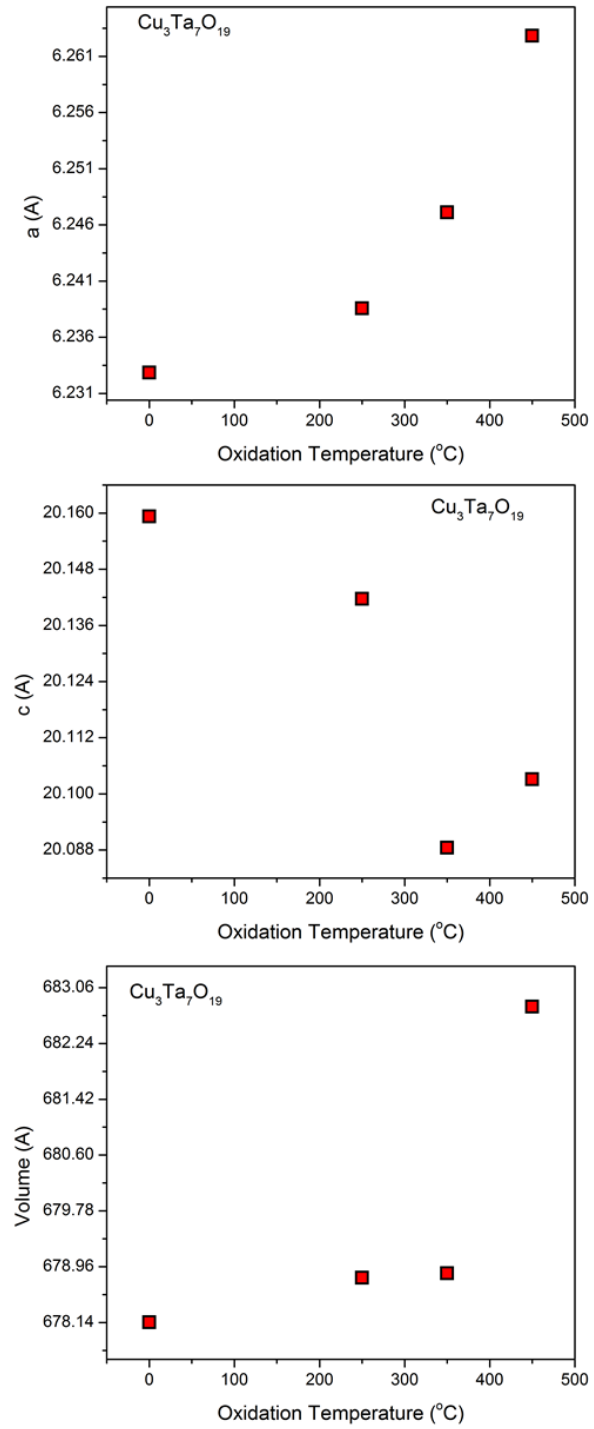


Figure 3.16. Unit cell lattice parameters for $\text{Cu}_3\text{Ta}_7\text{O}_{19}$.

REFERENCES

- (1) Joshi, U. A.; Maggard, P. A. *J. Phys. Chem. Lett.* **2012**, *3*, 1577.
- (2) Shintaro, I.; Yamada, K.; Matsunaga, T.; Hagiwara, H.; Matsumoto, Y.; Ishihara, T. *J. Am. Chem. Soc.* **2010**, *132*, 17343.
- (3) Hara, M.; Konda, T.; Komoda, M.; Ikeda, S.; Shinohara, K.; Tanaka, A.; Konda, J. N.; Domen, K. *Chem. Commun.* **1998**.
- (4) Ingler, W. B.; Baltrus, J. P.; Khan, S. U. M. *J. Am. Chem. Soc.* **2004**, *126*, 10238.
- (5) Leygraf, C.; Hendewerk, M.; Somorjal, G. A. *J. Phys. Chem.* **1982**, *86*, 4484.
- (6) Fuoco, L.; Joshi, U. A.; Maggard, P. A. *J. Phys. Chem. C* **2012**.
- (7) Joshi, U.; Palasyuk, A. M.; Maggard, P. A. *J. Phys. Chem. C* **2011**, *115*, 13534.
- (8) Palasyuk, O.; Palasyuk, A. M.; Maggard, P. A. *J. Solid State Chem.* **2010**, *183*, 814.
- (9) Palasyuk, O.; Palasyuk, A.; Maggard, P. A. *Inorg. Chem.* **2010**, *49*, 10571.
- (10) Joshi, U. A.; Palasyuk, A.; Arney, D.; Maggard, P. A. *J. Phys. Chem. Lett.* **2010**, *1*, 2719.
- (11) Li, G.; T., K.; Wang; D.; Zou, Z.; Ye, J. *J. Phys. Chem. of Solids* **2008**, *69*, 2487.
- (12) Kubelka, P.; Munk, F. *Z. Tech. Physik* **1931**, *12*, 593.

**PART 2: FLUX SYNTHESIS OF METAL OXIDE PARTICLES: INTERGRAIN
TUNNELING MAGNETORESISTANCE**

CHAPTER 4

INTRODUCTION TO MAGNETORESISTANCE

Magnetoresistance is an important property of materials defined by a change in the electrical resistance upon the application of a magnetic field. Growing research efforts have focused on materials exhibiting high magnetoresistance since the discovery of giant magnetoresistance in 1988 by Grünberg and Fert for their work with magnetic multilayered materials, which was awarded the Nobel prize in physics in 2007.¹ The discovery of giant magnetoresistance, defined as a change in resistance greater than 10%, has led to many technologically important applications of GMR materials such as in spin valves and highly sensitive read heads, both of which can allow for more data to be packed on a hard disk and are considered key contributors to the commercialization of computers.² As a result of increased research efforts, many additional types of materials have been explored and shown to exhibit GMR and even colossal magnetoresistance (magnetoresistance magnitudes larger than GMR), the most interesting of which have been ferromagnetic metal oxide materials.

There is growing research interest in the magnetoresistance displayed by ferromagnetic metal-oxide materials, especially in intergrain tunneling type magnetoresistance (ITMR) in which a theory has been proposed based on particle size and percent spin polarization. ITMR is an extrinsic magnetotransport property concerned with the spin polarized tunneling of current through a polycrystalline material.³ It is thought that

in polycrystalline samples that display ITMR, the grain boundary acts as an insulating barrier in which the tunneling of an electron between grains depends on the orientation of the moment between the adjacent grains.⁴ The application of a magnetic field aligns these moments between grains and allows greater current flow, thus lowering the resistance of the material (Figure 4.1). Materials displaying such properties at low magnetic fields and particularly at or above room temperature have potential applications as highly sensitive magnetic sensors.

Since ITMR is primarily concerned with the spin dependent tunneling of electrons, it is inherent to propose that materials with a higher amount of spin polarized electrons would thus produce a greater ITMR. The spin polarization of a ferromagnetic material in general, refers to the splitting of the spin density of states and an imbalance in their populations at the Fermi level and can be defined by

$$P = \frac{N_{\uparrow} - N_{\downarrow}}{N_{\uparrow} + N_{\downarrow}}$$

Where $N_{\uparrow\downarrow}$ is the density of the occupied state per unit volume of the majority or minority spin sub band at the Fermi level.⁵ Normal metals that are not ferromagnetic have a spin polarization of 0, ferromagnetic metals such as bcc Fe around 40 % spin polarized and the P values other of transition-metal ferromagnets range between 25-40 %.^{5,6} In theory a material which is 100% spin polarized would have a complete splitting of spins at the Fermi level in which one spin channel would be conducting while the other is insulating and as a result conduction would only occur in one specific spin direction. Compounds that exhibit this interesting spin splitting behavior are called half-metallic. An example of the spin

density of states for a normal metal, ferromagnetic metal and half-metal are shown in Figure 4.2. Half metallic character has been realized in some Heusler (ex. Co_2MnSi), half-Heusler (ex. NiMnSb) and ferromagnetic oxide compounds (ex. $\text{Sr}_2\text{FeMoO}_6$).⁷ Of the different types of half-metallic compounds mentioned, ITMR thus far is a property limited to only the half-metallic ferromagnetic oxide compounds.

Half-metallic ferromagnetic oxide compounds are rare, taking into consideration that only a small amount of oxides are ferromagnetic and an even smaller amount are also metallic. For this reason only a selected few of the half-metallic ferromagnetic oxides known today were in fact new compounds when initially labeled as half-metallic. A perfect example of this is CrO_2 which was mass produced in the 1970's for its use in magnetic recording tapes but wasn't actually predicted to be half-metallic until 1986 when the first set of band structure calculations for CrO_2 were performed.⁸ The bulk of information available on the prediction and labeling of the half-metallic metal oxides is in the form of DFT-based electronic structure calculations rather than direct measurement of the spin polarization. The spin polarization in ferromagnetic metal oxides however can be directly measured using the most commonly employed and least flawed point contact Andreev reflection method (PCAR).⁹ While the theory appears straightforward, this method as well as others does not give consistent results with all half-metallic materials and fabrication of the materials into thin films is challenging, and, as a result, the spin polarization of many half-metallic oxides has not been directly measured.

In addition to high spin polarization, ITMR is also proposed to be dependent on particle size. Research on polycrystalline samples in the doped magnetite perovskites La_1 .

$x\text{Ca}_x\text{MnO}_3$ show a strong correlation between decreasing grain size and increasing magnetoresistance which can be explained in terms of increased grain boundaries present in samples with smaller particles.⁵ This trend is projected to extend to other systems exhibiting ITMR. While the ITMR observed in magnetite perovskites is considered to be of colossal magnitude (>50 %), it is strongly reduced at room temperature and the application of these materials in actual devices would not be efficient in terms of the increased energy needed to cool the material to a working temperature. An alternative system with promising candidates is the half-metallic ordered double-perovskites, for example $\text{Sr}_2\text{FeMoO}_6$, that have been shown to exhibit low field ITMR at room temperature.

Materials with the ordered $\text{A}_2\text{BB}'\text{O}_6$ double-perovskite structure type host a variety interesting properties such as half-metallicity, ferromagnetism above room temperature, piezoelectricity, magnetoresistance, and superconductivity.¹⁰ The ordered $\text{A}_2\text{BB}'\text{O}_6$ double-perovskite structures of current interest in this research consists of alternating corner sharing BO_6 octahedra where B is usually a first row transition metal such as Cr, Mn, Fe, Co, or Ni and B' is Mo^{V} , Re^{V} , or W^{VI} (Figure 4.3). The A site cations situated within the cavities formed by the corner sharing octahedra are typically Sr, Ba or Ca. The B and B' cations adopt a 1:1 rock salt ordered sub lattice with the degree of ordering dependent on the charge difference between the B and B' cations. Compounds with $\text{A}_2^{\text{II}}\text{B}^{\text{II}}\text{B}^{\text{VI}}\text{O}_6$ are predicted to have partial ordering of the B and B' octahedra while compounds with $\text{A}_2\text{B}^{\text{III}}\text{B}^{\text{V}}\text{O}_6$ are predicted to have complete ordering of the B site cations. In the case of $\text{Sr}_2\text{FeMoO}_6$ and other reduced ferromagnetic double-perovskites listed in Table 4.1, this ordering of the B sub lattice is responsible for its ferromagnetic half-metallic nature.

The wide range of magnetic and electronic properties displayed by the double perovskite compounds listed in Table 4.1 such as ferromagnetism, half-metallic character, insulating character, antiferromagnetism. Their high Curie and Neel temperatures are based on the types of interactions between the d transition metals and oxygen p orbitals. The ideal $A_2BB'O_6$ double-perovskite structure is cubic with space group $Fm\bar{3}m$. However, it is estimated that around 70 % of reported ordered double-perovskites have distorted structures as a result of size mismatch between the A and B/B' cations.¹⁰ In addition to these structural distortions are the possibility of site defects. Antisite disorder is the most common defect that occurs in these structures. Other possible but rarely observed defects such as oxygen vacancies, antiphase boundaries and A site cation vacancies have also been noted to occur on rare occasions.¹¹ Antisite defects in the ordered double-perovskites refers to the misplacement between B and B' atoms in the structure. In ordered ferromagnetic double-perovskites with antiferromagnetically coupled B and B' sub lattices such as Sr_2FeMoO_6 , every antisite defect contributes to a lowering of the saturation magnetization of the sample.¹² In the half-metallic double-perovskites, large amounts of antisite defects can even lead to the breakdown of their half-metallic character. The amount of antisite defects have been shown to be synthesis in a number of the ordered double-perovskites most notably being half-metallic Sr_2FeMoO_6 .¹¹ Thus it is important to find synthetic methods that produce double-perovskites samples with a high degree of cation ordering. The current research is directed at a) investigation of flux synthetic methods to synthetically control particle sizes that have a distinct morphology, and, b) investigate the effect of flux on the B and B' cation ordering and the magnetoresistance which c) therefore enabling deeper investigations of the effects of

particle sizes and % B/B' site ordering on their magnetic properties of half-metallic double-perovskites in the $A_2BB'O_6$ ($A = \text{Ba, Sr}$, $M' = \text{Cr}^{3+}, \text{Fe}^{3+}$, $B = \text{Re}^{5+}$) family.

The bulk of synthetic methods used for the synthesis of double-perovskites involve the ceramic method (Table 4.1). In the ceramic method, the reactants are heated to high temperatures during which the product forms initially by phase boundary reactions and later by diffusion through the product phase.¹³ Because of the slow diffusion rate, reaction times are usually long, such as on the order of days to weeks. The resulting products are frequently a mixture of reactants and products which are often purified through intermittent regrinding to expose fresh reactant surfaces and followed by additional heating. In the synthesis of reduced double-perovskites, the ceramic method is often used in conjunction with a reduced atmosphere such as H_2 , and which must be carefully monitored. An alternative and much more accessible approach to the synthesis of these compounds is the molten flux synthetic method which involves the use of molten salts as a solvent media. This allows for product formation to occur at faster rates and lower temperatures than conventional ceramic methods.¹⁴ In a typical flux synthesis reaction, the flux and the reactants, which have some degree of solubility in the flux, are heated to a temperature above the melting point of the flux to achieve a molten solution. Reaction time is significantly decreased due to the increased mobility of the reaction constituents and products of high purity are obtained without any additional heating. One of the most important advantages of the flux method is the ability to control particle size which has been shown to have a significant effect on the physical properties of solid state materials. An example of such is the flux synthesis of the lithium battery material LiCoO_2 which showed enhanced cycling capacity as a function of

smaller and more uniform particle sizes obtained through flux synthesis.¹⁵ The size and shape of products can be controlled in a molten flux reaction by changing the amount of flux, type of flux, heating time, and heating temperature.¹⁶ An additional example of where Flux synthesis methods have been used to synthesize pure products and exercise control over particle size and morphology is in the flux synthesis of the layered perovskite $\text{Bi}_5\text{Ti}_3\text{FeO}_{15}$.¹⁷ Distinct platelet-like morphologies were obtained using a $\text{Na}_2\text{SO}_4/\text{K}_2\text{SO}_4$ flux at 1000 °C and control over particle size was exercised by varying the length of heating time.¹⁷

Factors to consider when selecting a suitable flux include the solubility of reaction components, volatility, ease of removal from product, and flux ion size. Ideally, a suitable flux is one that does not unintentionally become incorporated into the product lattice as impurities. This situation can be avoided by selecting a flux with ions that are the same as those in the product. The most common types of fluxes encountered in literature are alkali-halides, nitrates, carbonates, hydroxides, and molten metals. The alkali-halide fluxes are among the most common fluxes used in metal oxide synthesis. Reasons for this include their ease of removal, relatively low melting points, low volatility, and suitability for use in sealed ampoule reactions. Examples of the use of molten fluxes to synthesize reduced transition-metal oxide compounds are limited.¹⁸ An example of such is the flux synthesis of the reduced niobate compound Sr_xNbO_3 using a borate flux $\text{AO}_3 \cdot \text{B}_2\text{O}_3$ A= Ba, Sr under vacuum conditions.¹⁹ An alternative to using a borate type flux are the eutectic halide fluxes such as NaCl-KCl which have low volatilities and much lower melting points of around 650-800 °C. By using alkali halide fluxes such as NaCl-KCl in a sealed ampule, we have shown that it is

possible to obtain reduced double-perovskite compounds never before synthesized by molten flux method.

The major efforts of my research work described in Part 1 of this document involve the new flux synthesis of half-metallic double-perovskites that allows for particle size and morphology control, as well as extent of B/B' site ordering. The flux amount, heating duration and cooling rates were varied, and an investigation of their effects on particle sizes, extent of B/B' site ordering, as well as magnetic and electrical properties is presented.

Table 4.1. Magnetic and electronic properties, crystallographic parameters and the most common synthesis or only synthesis method employed for the half-metallic and related double-perovskites. Ferromagnetic is represented as FM, antiferromagnetic as AFM, paramagnetic as PM and canted ferromagnetism as CFM. Blank fields indicate an absence of a property reported in the literature.

Compound	Space Group	Prep. Method	T _c / T _N [K]	Conduction	Ref.
Sr ₂ FeMoO ₆	<i>I4/m</i>	* 3 h at 900 °C, 2 h at 1200 °C under H ₂ /Ar	420, AF	Half-metallic	20,21
Ca ₂ FeMoO ₆	<i>P2₁/n</i>	*3 h 950 °C, 5-10 h 1100 °C h under H ₂ /Ar mixture	320, FM	Half-metallic	20,22,23
Ba ₂ FeMoO ₆	<i>Fm3m</i>	* 2 days at 1000 °C, 2 h at 1150 °C under H ₂ / Ar mixture	330, PM	Half-metallic	12,24
Sr ₂ CrMoO ₆	<i>Fm3m</i>	*3 h at 900 °C, 2 h at 1200 °C under H ₂ /Ar	450	Half-metallic	25,26
Ca ₂ CrMoO ₆	<i>Pbnm</i>	*3 h at 900 °C, 12 h at 1290 °C under H ₂ /Ar	125	Half-metallic	11,27
Ba ₂ CrMoO ₆	<i>P6₃/mmc</i>	*3 h at 900 °C, 12 h at 1290 °C under H ₂ /Ar	PM	Semiconducting	11,28
Sr ₂ MnMoO ₆	<i>Fm3m</i>	*15 h at 950 °C, 48 h 1200°C, ¹ 48 h at 1350 °C, 48 h at 1400 °C, all under N ₂	AFM	Insulator	11,29
Sr ₂ FeReO ₆	<i>I4/m</i>	*3 h at 900 °C, ² 2 h at 1200 °C under H ₂	400,AF	Half-metallic	20,30
Ca ₂ FeReO ₆	<i>P2₁/n</i>	*48 h at 900 °C, ² 14 days at 900°C	540	Insulator	20,31
Ba ₂ FeReO ₆	<i>Fm3m</i>	*several days at 950 °C ²	300-340, FM	Metallic	20,32
Ca ₂ CrReO ₆	<i>P2₁/n</i>	*3 h at 900 °C, ² 3 h 1400 °C under Ar	360, FM	Insulator	20,33
Sr ₂ MnReO ₆	<i>P2₁/n</i>	*170 h at 1000 °C ³	120, CFM	Insulator	11,34
Sr ₂ NiReO ₆	<i>I4/m</i>	*heated at 900 °C, ² heated at 1200–1400 °C under Ar ¹	18 K, FM	Insulator	33
Sr ₂ CrReO ₆	<i>I4/m</i>	*2 h 1375 °C under H ₂ /Ar	635, FM	Metallic	11,20,24,35
Sr ₂ CoReO ₆	<i>I4/m</i>	*12 h at 1200 °C under N ₂ ⁵	65, AFM	Insulator	11,36
Ca ₂ CoReO ₆	<i>P2₁/n</i>	*heated at 900 °C, ² sintered at 1200–1400 C in Ar ¹	130, AFM	Insulator	11,33

Table 4.1. Continued

Ba ₂ CoReO ₆	<i>Fm3m</i>	*precursor Ba ₅ Re ₂ O ₁₂ , 24 h at 1100 °C. ^{2,3}	40, AFM	Semiconducting	11,37,38
Ca ₂ MnReO ₆	<i>P2₁/n</i>	*heated at 900 °C, ² sintered at 1200–1400 °C in Ar ¹	110, FM	Insulator	33
Sr ₂ ScReO ₆	<i>P2₁/n</i>	*heated at 900 °C, ² sintered at 1200–1400 °C in Ar ¹	75, AF	Insulator	33
Sr ₂ MgReO ₆	<i>I4/m</i>	*heated at 900 °C, ² sintered at 1200–1400 °C in Ar ¹	320, AF	Insulator	33
Sr ₂ ZnReO ₆	<i>I4/m</i>	*heated at 900 °C, ² sintered at 1200–1400 °C in Ar ¹	20, AF	Insulator	33
Sr ₂ FeWO ₆	<i>P2₁/n</i>	*15 h at 1000 °C under N ₂ , ⁴ 48 h at 1100 °K, ^{2,3} 48 h at 1623 K, ^{2,3} 6 h at 1400 K ^{2,3}	37, AFM	Insulator	39,40
Ba ₂ FeWO ₆	<i>I4/m</i>	* heated at 1000 °C, ⁴ several days at 1400 °C under N ₂	40, AFM		11,41
Sr ₂ CrWO ₆	<i>Fm3m</i>	*12 h at 800 °C 12 h, 10 h at 1500 °C under H ₂ /N ₂ ¹	460	Half-metallic	20,42,43
Ba ₂ CrWO ₆	<i>P62c</i>	*heating cycles up to 1570 °C ⁴	145,PM		11,44
Ca ₂ CrWO ₆	<i>P2₁/n</i>	*sintered at 1300 °C under H ₂ /Ar multiple times	160		20,45
Sr ₂ CoWO ₆	<i>I4/m</i>	*6 h at 900 °C, 24 h at 1150 °C	24, AFM	Half-metallic	46,47
Ca ₂ CoWO ₆	<i>P2₁/n</i>	*20 h at 900 °C, 40 h at 1000 °C ³	36, AFM		48,49
Ba ₂ CoWO ₆	<i>Fm3m</i>	*4 h at 1100 K, ⁴ 4 h at 1270-1570 K ⁴			50

The terms FM, AFM and PM correspond to ferromagnetic, antiferromagnetic and paramagnetic respectively. ¹ Indicates the sample was pressed into a pellet before heating. ² Indicates heating was done in a sealed evacuated silica ampule. ³ Indicates periodic regrinding was performed. ⁴ Indicates ball milling was done prior to the heating cycle. ⁵ Indicates a soft chemistry precursor method was used prior to the heating cycle.

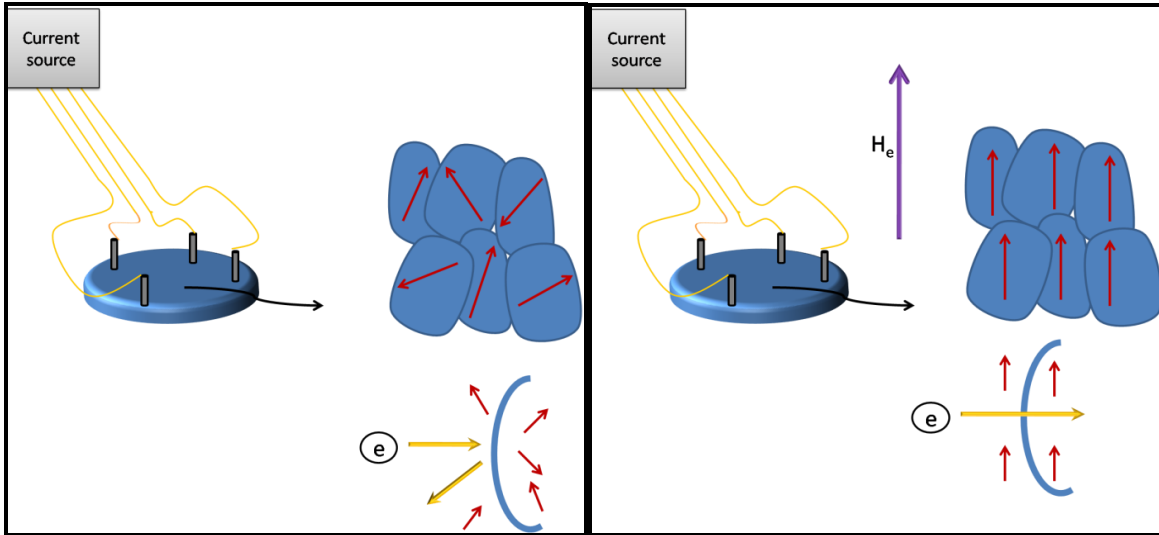


Figure 4.1. An illustration of ITMR where the set up on the right is in the absence of a magnetic field where tunneling is disfavored. The set up on the left represents the tunneling of an electron that occurs in the presence of a magnetic field.

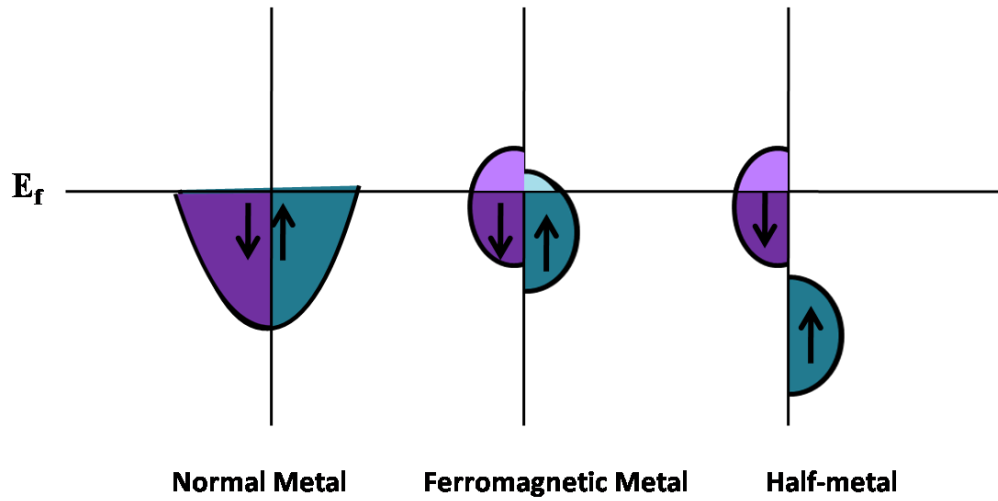


Figure 4.2. A representation of the spin density-of-states at the Fermi level for a normal metal, ferromagnetic metal and a half-metal.

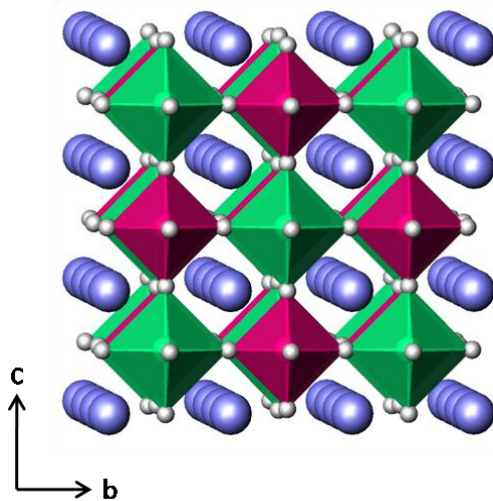


Figure 4.3. Crystal structure of the B-site ordered $A_2BB'O_6$ double-perovskite with space group $Fm\bar{3}m$. BO_6 octahedra are shown in green, $B'O_6$ octahedra are shown in pink, A atoms are shown in blue and O atoms are shown in gray.

REFERENCES

- (1) Fert, A. *Angew. Chem. Int. Ed.* **2008**, *47*, 5956.
- (2) Smart, L. E., Moore, E.A. *Solid State Chemistry An Introduction*; third ed.; Taylor and Francis: New York, **2005**.
- (3) Ziese, M. *Rep. Prog. Phys.* **2002**, *65*, 143.
- (4) Ju, S., Li, Z. *J. Appl. Phys* **2002**, *92*, 5281.
- (5) Gupta, A., Sun, J.Z. *J. Magn. Magn. Mater.* **1999**, *200*.
- (6) Zhu, Z., Zhang, H., Xu, S., Chen, J., Wu, G., Zhang, B. *J. Phys.: Condens. Matter* **2008**, *20*.
- (7) Pickett, W., Moodera, *Phys. Today* **2001**, 39.
- (8) Schwarz, K. *Institute of Physics: Letter to the editor* **1986**, 211.
- (9) Nadgorny, B. *J. Phys.: Condens. Matter* **2007**, *19*.
- (10) Lufaso, M. B., P., Woodward, P.M. *Acta Cryst.* **2006**, *B62*, 397.
- (11) Serrate, D., De Teresa, J.M., Ibarra, M.R. *J. Phys.: Condens. Matter* **2007**, *19*, 023201.
- (12) Navarro, J., Nogues, J., Munoz, J., Frontcuberta, J. *Phys. Rev. B* **2003**, *67*.
- (13) Rao, C. N. R., Gopalakrishnan, J. *New Directions in Solid State Chemistry*; Cambridge University Press, **1997**; Vol. Cambridge, U.K.
- (14) Elwell, D., Neate, B.W. *J. Mater. Sci.* **1971**, *6*, 1499.
- (15) Liang, H., Qiu, X., Zhang, S., He, Z., Zhu, W., Chen, L. *Electrochem. Commun.* **2004**, *6*, 505.
- (16) Zhou, H., Mao, Y., Wong, S. *Chem. Mater.* **2007**, *19*, 5238.

- (17) Porob, D., Maggard, P. A. *Mater. Res. Bull.* **2006**, *41*, 1513.
- (18) Hessen, B., Sunshine, S., Siegrist, T., Fiory, A., Waszczak, J. *Chem. Mater.* **1991**, *3*, 528.
- (19) Hessen, B., Sunshine, S., Siegrist, T., Jimenez, R. *Mater. Res. Bull.* **1991**, *26*, 85.
- (20) Haghiri-Gosnet, A. M., Arnal, T., Soulimane, R., Koubaa, M., Renard, J. P. *phys. stat. sol. (a)* **2004**, *201*, 1392.
- (21) Kobayashi, K.-I., Kimura, T., Sawada, H., Terakura, K., Tokura, Y. *Nature* **1998**, *395*, 677.
- (22) Rubi, D., Frontera, C., Roig, A., Nogues, J., Munoz, J., Frontcuberta, J. *J. Phys.: Condens. Matter.* **2005**, *17*, 8037.
- (23) Borges, R. P., Thomas, R.M., Cullinan, C., Coey, J.M.D., Suryanarayanan, R., Bendor, L., Pinsard-Gaudart, L., Revcolevschi, A. *J. Phys.: Condens. Matter* **1999**, *11*, 445.
- (24) Mandal, T. K., Felser, C., Greenblatt, M., Kubler, J. **2008**.
- (25) Bonilla, C. M., Landinez Tellez, D.A., Arbey Rodriguez, J., Vera Lopez, V., Roa-Rojas, J. *Physica B* **2007**, *398*, 208.
- (26) Arulraj, A., Ramesha, K., Gopalakrishnan, J., C.N.R. Rao *J. Solid State Chem.* **2000**, *155*, 233.
- (27) Martinez-Lope, M. J., Alonso, J.A., Casais, M.T., Garcia-Hernandez, M., Pomjakushin, V. *J. Solid State Chem.* **2006**, *179*, 2506.
- (28) Sher, F., Attfield, P. *Solid State Sci.* **2006**, *8*, 277.

- (29) Azad, A., Mellergard, A., Eriksson, S.-g., Ivanov, S.A., Mathiew, R., Svedlindh, P., Eriksen, J., Rundlof, H. *J. Alloys and Compd.* **2004**, 364, 77.
- (30) K.-I. Kobayashi, K., T., Y. Tomioka, H. Swada, K. Terakura, Y. Tokura *Phys. Rev. B* **1999**, 59, 159.
- (31) Westerburg, W., Lang, O., Ritter, C., Felser, C., Tremel, W., Jakob, G. *Solid State Commun.* **2002**, 122, 201.
- (32) Auth, N. J., G.; Westernurg, W.; Ritter, C.; Bonn, I.; Felser, C. *J. Magn. Magn. Mater.* **2004**, 272.
- (33) Kato, H., Okuda, T., Okimoto, Y., Tomioka, Y, Takenoya, Y., Ohkubo, A., Kawasaki, M., Tokura, Y. *Appl. Phys. Lett.* **2002**, 81.
- (34) Popov, G., Lobanov, M., Tsiper, E., Greenblatt, M., Caspi, E., Borissov, A., Kiryukhin, V., Lynn, J. *J. Phys.: Condens. Matter* **2004**, 16, 135.
- (35) Michalik, J. M. T. J. M., Ritter, C., Blasco, J., Serrate, M.R., Ibarra, M.R., Kapusta, C., Freudenberger, J., Kozlova, N. *Europhys. Lett.* **2007**, 78.
- (36) Rutuerto, M., Martinez-Lope, M., Garcia-Hernandez, M. Fernandez-Diaz, M., Alonso, J. *Eur. J. Inorg. Chem.* **2008**, 588.
- (37) Rammeh, N., Ehrenberg, H., Fuess, H., Cheikkh-Rouhou, A. *phys. stat. sol. (c)* **2006**, 3, 3225.
- (38) Sleight, A., Weiher, J. *J. Phys. Chem. Solids.* **1972**, 33, 679.
- (39) Carvajal, E., Navaroo, O., Allub, R., Avignon, M., Alascio, B. *phys. stat. sol. (b)* **2005**, 242, 1942.

- (40) Azad, A. K., Eriksson, S.-G, Mellergard, A., Ivanov, S.A., Eriksen, J., Rundlof, H
Mater. Res. Bull. **2002**, 37, 1797.
- (41) Azad, A., Mellergard, A., Eriksson, S.-g., Ivanov, S.A., Eriksen, J., Rundlof, H. *Appl. Phys. A* **2002**, 74, 763.
- (42) Chan, T. S., Liu, R.S., Guo, G.Y., Hu, S.F., Lin, J.G., Lee, J.-F., Jang, L.-Y., Chang, C.-R., Huang, C.Y. *Solid State Commun.* **2004**, 131.
- (43) Vaitheeswaran, G., Kanchana, V., Delin, A. *J. Phys.: Conference Series* **2006**, 29, 50.
- (44) Zhao, F., Yue, Z., Gui, Z., Li, L. *Jpn. J. Appl. Phys.* **2005**, 11, 8066.
- (45) Philipp, J. B., Majewski, P., Alff, L., Erb, A., Gross, R., Graf, T., Brandt, M.S., Simon, J., Walther, T., Mader, W., Topwal, D., Sarma, D.D. *Phys. Rev. B* **2003**, 68.
- (46) Viola, M. C., Martinez-Lope, M. J., Alonso, J. A., Martinez, J. L., Paoli, J. M., Pagola, S., Pedregosa, J. C., Fernandez-Diaz, M. T., Carbonio, R. E. *Chem. Mater.* **2003**, 15, 1655.
- (47) Bonilla, C. M., Landinez Tellez, D.A., Arbey Rodriguez, Aguiar, J., Roa-Rojas, J. *J. Magn. Magn. Mater.* **2008**, 320, 397.
- (48) Zhou, Q., Kennedy, B., Elcombe, M. *J. Solid State Chem.* **2007**, 180, 541.
- (49) Martinez-Lope, M. J., Alonso, J.A., Casais, M.T., Fernandez-Diaz, M.T. *Z. Naturforsch.* **2003**, 58b, 127.
- (50) Zhao, F., Yue, Z., Gui, Z., Li, L. *Jpn. J. Appl. Phys.* **2005**, 44, 8066

CHAPTER 5

Rapid Molten-salt Syntheses of $\text{Sr}_2\text{FeReO}_6$, $\text{Ba}_2\text{FeReO}_6$ and $\text{Sr}_2\text{CrReO}_6$: Particle Sizes, B/B'-site Disorder, and Magnetic Properties

Based on a paper published in *Chemistry of Materials* 2011, 23, 5409-5414.

Lindsay Fuoco, Dianny Rodriguez, Tim Peppel and Paul A. Maggard

Department of Chemistry, North Carolina State University, Raleigh, NC 27695

TOC Caption. An SEM image of $\text{Sr}_2\text{FeReO}_6$ synthesized in high-purity in an NaCl/KCl flux at 750 °C for 3 h with homogeneous particles ranging from ~50 – 100 nm in size. Temperature and magnetic-field dependence of the electrical resistivity for polycrystalline $\text{Sr}_2\text{FeReO}_6$ pellets prepared via the solid-state and flux-synthetic routes (1:1 molar ratio, 3 h).

Keywords: Double perovskites, flux-mediated synthesis, magnetoresistance

ABSTRACT

The half-metallic double-perovskites $\text{Sr}_2\text{FeReO}_6$, $\text{Ba}_2\text{FeReO}_6$ and $\text{Sr}_2\text{CrReO}_6$ were synthesized in high purity and homogeneity in a NaCl/KCl molten flux at 750-800 °C in as little as 3-6 h. The particle sizes could be varied from ~50 nm to > 1 μm depending on the

specific flux conditions and the double-perovskite composition. Powder X-ray diffraction refinements were used to characterize the extent of B/B'-site disorder (i.e. Fe/Re or Cr/Re sites), and that ranged from ~83-84% for Sr₂FeReO₆, ~90-94% for Ba₂FeReO₆ and ~83-90% for Sr₂CrReO₆. The magnetic properties were measured as a function of magnetic field strength and analyzed with respect to the extent of B/B' site ordering and resultant particle sizes that ranged from ~ 50 - 500 nm for Sr₂FeReO₆, ~ 100 - 800 nm for Sr₂CrReO₆ and ~ 250 nm to 2μm for Ba₂FeReO₆. Further, large temperature dependent magnetoresistivities were observed for the flux-prepared Sr₂FeReO₆, Ba₂FeReO₆ and Sr₂CrReO₆ owing to the increased concentration of grain boundaries.

INTRODUCTION

The double-perovskites of the composition A₂BB'O₆ (A = Sr or Ba; B = Fe or Cr; B' = Mo or Re) have been the focus of intense research interest owing to the discovery of high magnetic-ordering transition temperatures and the half-metallic properties of Sr₂FeMoO₆ (T_c ~ 415K), Sr₂FeReO₆ (T_c ~ 400K), Sr₂CrReO₆ (T_c ~ 635K) and others.¹⁻⁵ Interestingly, large magnetoresistances have been measured in their polycrystalline forms that result from spin-polarized intergrain tunneling across the particle grain boundaries, and as expected, is absent in the analogous single-crystal measurements.⁶ A spin-dependent transport mechanism were first proposed and found in metal oxides such as for La_{2/3}Sr_{1/3}MnO₃.⁷ In these A₂BB'O₆ double-perovskites, the magnetic properties exhibit a strong dependence on the resulting grain sizes and the extent of B/B' site disorder present in their structures, and which in turn depend closely on the synthesis conditions.⁸⁻¹⁰ In Sr₂FeMoO₆, for example, the formation of

much smaller metal-oxide particles has been shown to yield significant enhancements in the intergrain tunneling-magnetoresistance (i.e. ITMR) properties of multigrain samples.¹⁰⁻¹² However, high-purity and homogeneity are typically difficult to obtain for reduced rhenates (i.e. $\text{Re}^{5+}/\text{Re}^{6+}$) owing to their refractive nature. Members of the reduced rhenate family must predominantly be prepared according to relatively demanding solid-state procedures that involve multiple heating cycles (>1 - 2 weeks), carefully-controlled reducing conditions inside sealed-silica ampoules, and temperatures up to 1200 °C. Thus, more rapid and efficient routes that target high-purity, homogeneous, and tunable distributions of particle sizes are needed for probing their magnetic properties in polycrystalline forms.

The use of molten-salt fluxes can potentially yield a significantly greater flexibility to modulate metal-oxide particle sizes and microstructures via selection of the amount and type of flux, reaction time and temperature, and also cooling rates.¹³⁻¹⁶ Flux-mediated syntheses can allow for metal-oxide particles to form at relatively fast rates (< 1 h) and in a more well-faceted and homogeneous distribution of sizes, owing to the enhanced mobility of the metal-oxide reactants in the flux. For example, molten-salt mixtures of $\text{Na}_2\text{SO}_4/\text{K}_2\text{SO}_4$ and NaCl/KCl have been used to prepare the layered perovskites $\text{Bi}_5\text{Ti}_3\text{FeO}_{15}$ and $\text{La}_2\text{Ti}_2\text{O}_7$ in high purity in only 0.5 h with platelet morphologies and tunable particle sizes of down to <100 nm in thickness and ~500 - 5,000 nm on the edges.^{13,15} However, to the best of our knowledge, the flux synthetic method has never previously been reported for the preparation of reduced rhenate compositions (i.e. containing Re^{5+} or Re^{6+}). Reported herein are the first flux-mediated syntheses of three reduced-rhenate members (i.e. $\text{Re}^{5+}/\text{Re}^{6+}$) of the $\text{A}_2\text{BB}'\text{O}_6$ double-perovskite family, $\text{Sr}_2\text{FeReO}_6$, $\text{Ba}_2\text{FeReO}_6$ and $\text{Sr}_2\text{CrReO}_6$ via rapid, single-step

reactions using a eutectic NaCl/KCl salt mixture. The flux amount, heating duration and cooling rates were varied and investigated for their effects on particle sizes, extent of B/B' site ordering, as well as magnetic and electrical properties.

EXPERIMENTAL

Synthesis. Flux syntheses of $\text{Sr}_2\text{FeReO}_6$, $\text{Ba}_2\text{FeReO}_6$ and $\text{Sr}_2\text{CrReO}_6$ were performed by first combining stoichiometric mixtures of SrO (Alfa Aesar, 99.5%), BaO (Alfa Aesar, 99.5%), Cr_2O_3 (Sigma Aldrich, 99%), Fe_3O_4 (Alfa Aesar, 99), Re_2O_7 (Alfa Aesar, 99.995%), and Re (Alfa Aesar, 99.99%) inside a glove-box under a nitrogen atmosphere. The loaded Re: Re_2O_7 molar ratio for $\text{Sr}_2\text{FeReO}_6$ was stoichiometric (5:8 ratio), while reactions for $\text{Ba}_2\text{FeReO}_6$ and $\text{Sr}_2\text{CrReO}_6$ needed to be loaded more Re_2O_7 -rich (4.6:8 and 2:6 ratios, respectively) in order to achieve highly pure phases. The reactants were ground together and combined with a eutectic NaCl/KCl mixture to give flux: product molar ratios of 0.5:1 and 1:1 for $\text{Sr}_2\text{FeReO}_6$, and 1:1 and 3:1 for $\text{Ba}_2\text{FeReO}_6$ and $\text{Sr}_2\text{FeReO}_6$. These reactant mixtures were flame-sealed inside evacuated fused-silica ampoules (length = 90 mm, i.d. = 8 mm) and heated to 750 °C for $\text{Sr}_2\text{FeReO}_6$ for 3-12 h, or to 800 °C for both $\text{Sr}_2\text{CrReO}_6$ and $\text{Ba}_2\text{FeReO}_6$ for 6 h. The reactions were then either quenched, slow cooled or radiatively cooled to room temperature. The resulting products were washed with hot deionized water to remove the NaCl/KCl flux. Further increases in the flux amounts were unsuccessful and resulted in impurities. The standard solid-state synthesis of $\text{Sr}_2\text{FeReO}_6$ was performed for comparison by using a slightly modified procedure from the literature,¹⁷ which involved the preparation of a $\text{Sr}_2\text{ReO}_{5.5}$ precursor by combining stoichiometric amounts of SrCO_3 and

Re₂O₇ and heating in air at 1100°C for 6 h. The Sr₄Re₂O₁₁ precursor compound was then combined with Fe₂O₃ and Fe and ground together with a mortar and pestle in a glove-box under a nitrogen atmosphere. The resulting mixture was flame sealed inside an evacuated silica ampule and heated at 910°C for 72 h followed by annealing at 960°C for 72 h with intermittent regrinding. Powder X-ray diffraction analysis revealed a small Re impurity phase (~5%) still present in the solid-state reaction product.

Characterization. High resolution powder X-ray diffraction data sets were collected for all samples at room temperature on a Rigaku R-Axis Spider with a curved image plate detector and using Cu K α ₁ radiation from a sealed tube x-ray source. Refinements were performed by the Rietveld method using the WPF Refinement option in Jade 9.¹⁸ In a typical refinement, initially only the zero-point shift and scale factor were refined. The lattice constants and background parameters were then allowed to refine followed by the oxygen positions. This was followed by refinement of the isotropic thermal parameters which thereafter were fixed to refine the Fe/Re or Cr/Re site occupancies. The thermal parameters were then released in the last stage of the refinement. Multiple cations occupying the same site were assumed to have the same thermal displacement parameters. The thermal displacement parameters for multiple oxygen atomic positions were also set to be equal. Powder refinement parameters are given in Tables 5.1, 5.2 and 5.3 for Sr₂FeReO₆, Ba₂FeReO₆, and Sr₂CrReO₆, respectively, and resulting fits of the Rietveld refinements to the experimental powder data are plotted in Figures 5.1-5.3. More complete tables of all refinement parameters are provided in the Supporting Information.

Scanning Electron Microscopy (SEM) was performed on a FEI Quanta 200 and used to investigate the particle microstructures and sizes as a function of flux-preparation conditions. Field-dependent magnetization measurements were taken on ~50 mg of the powdered samples from -7 to 7 T at 5K using a Quantum Design MPMS XL SQUID. Electrical resistivity measurements were performed on high-purity pelletized samples using the four probe method (Hall effect instrument; MMR Technologies) at magnetic field strengths extending from 0 to 3 kG over a temperature range of 300-550 K.

RESULTS AND DISCUSSION

Structure Refinements and Particle Characterization. The double-perovskite structure of $\text{Sr}_2\text{FeReO}_6$ exhibits a rock-salt type ordering of the Fe/Re transition metals in a parent ABO_3 perovskite-type structure that also exhibits a small tetragonal distortion (space group: $I4/m$).⁴ The related structures of $\text{Sr}_2\text{CrReO}_6$ and $\text{Ba}_2\text{FeReO}_6$ also exhibit a rock-salt ordering of the Cr/Re and Fe/Re cations and crystallize in the non-distorted cubic crystal system (space group: $Fm-3m$; Figures 5.1, 5.2, and 5.3).^{4,19} The powder X-ray diffraction (PXRD) patterns for the flux and solid-state-prepared $\text{Sr}_2\text{FeReO}_6$, $\text{Ba}_2\text{FeReO}_6$, and $\text{Sr}_2\text{CrReO}_6$ products are shown in Figures 5.4, 5.5 and 6.6 respectively. These confirmed that each could be synthesized within a molten NaCl/KCl flux in high purity in reaction times of only ~3 – 6 h. Rietveld refinements of the PXRD data for all samples were carried out and the resultant lattice parameters, atomic coordinates, B/B' site occupancies and $R_b(\%)$ values are provided in Tables 5.1, 5.2, and 5.3. Rietveld refinement profiles for $\text{Sr}_2\text{FeReO}_6$ (using a 0.5:1 flux ratio for 12 h), $\text{Ba}_2\text{FeReO}_6$ (1:1 flux ratio for 6 h) and $\text{Sr}_2\text{CrReO}_6$ (1:1 flux ratio for

6 h), all radiatively cooled, are shown in Figures 5.4, 5.5 and 5.6 respectively. Rietveld refinement profiles for all other samples are provided in the Supporting Information. The extent of B/B' (i.e., Fe/Re) ordering is reflected in the peak intensities of the main superstructure (111) or (101) Bragg reflections. These characteristic peaks are presents in all the flux-synthesized and solid-state $\text{Sr}_2\text{FeReO}_6$, $\text{Ba}_2\text{FeReO}_6$ and $\text{Sr}_2\text{CrReO}_6$ products.

Powder X-ray refinement results listed in Table 5.1 show that the degree of B/B' site ordering obtained for the flux-prepared $\text{Sr}_2\text{FeReO}_6$ samples was ~83 - 84 % with relatively little variation except for a slightly higher ordering found for the 12 h versus 3 h reaction times. Conversely, the $\text{Sr}_2\text{FeReO}_6$ sample, prepared by solid-state methods over the course of one week of heating, was found to show an 97% complete Fe/Re site ordering, consistent with previous reports.^{2,20} For $\text{Ba}_2\text{FeReO}_6$, the degree of Fe/Re site ordering ranged from ~90-96%, with the highest ordering found for the longest reaction time of 24 h. This is somewhat lower than the 97% Fe/Re ordering obtained by solid-state methods at much longer reaction times.¹⁹ The Cr/Re ordering for the flux-prepared $\text{Sr}_2\text{CrReO}_6$ products ranged from ~83 - 90%, with the highest ordering of ~90% for the 1:1 flux reaction that was slow cooled over 2 days and the lowest ordering of ~84% for the 3:1 flux reaction that was quenched after 6 h. Previously reported solid-state preparations of $\text{Sr}_2\text{CrReO}_6$ resulted in a ~77 - 87% Cr/Re ordering, comparable to our flux preparations.^{4,21,22} Thus, while there is a significant tradeoff of the extent of B/B' site ordering for shorter flux-reaction times in $\text{Sr}_2\text{FeReO}_6$, there is little to almost no significant effect of the shorter flux-reaction times for $\text{Ba}_2\text{FeReO}_6$ and $\text{Sr}_2\text{CrReO}_6$.

Representative scanning electron microscopy (SEM) images of the flux-synthesized products for $\text{Sr}_2\text{FeReO}_6$, $\text{Ba}_2\text{FeReO}_6$, and $\text{Sr}_2\text{CrReO}_6$ are given in Figures 5.7 and 5.8, typically for both the smallest and largest particle-size distributions found for each. All SEM images revealed homogeneous distributions of aggregated block-like particles that, depending on the particular double-perovskite product and the flux reaction conditions, could be varied in size from ~ 50 nm to $> 1\ \mu\text{m}$. The smallest particle sizes of ~ 50 nm could be prepared for $\text{Sr}_2\text{FeReO}_6$ using 1:1 or 0.5:1 flux:product molar ratio reacted for only 3 h, shown in Figure 5.7 (A and C). These particles could be increased in size up to ~ 500 nm by increasing the reaction time to 12 h, Figure 5.7 B. By contrast, the variation of flux reaction conditions (i.e. flux amount, reaction time) had a relatively much smaller effect on the particle sizes and distributions for either $\text{Ba}_2\text{FeReO}_6$ or $\text{Sr}_2\text{CrReO}_6$. For $\text{Ba}_2\text{FeReO}_6$, shown in Figure 5.8 (A, B, and C), relatively larger particles of $> 1\ \mu\text{m}$ were formed after only a 6 h reaction using either 1:1 or 3:1 flux ratio. Quenching this reaction produced only slightly smaller particles, Figure 5.8 C. While for $\text{Sr}_2\text{CrReO}_6$, shown in Figure 5.8 (D, E, and F), a mixture of both smaller $\sim 50 - 100$ nm particles and larger ~ 500 nm particles nearly always resulted using these flux conditions. Either quenching or slow cooling these reactions only resulted in small changes in the distribution of smaller versus larger particles. While, in general, the particle sizes decreased with increasing amounts of flux and with faster cooling rates, the rate of particle growth in the NaCl/KCl flux was significantly more variable for $\text{Sr}_2\text{FeReO}_6$ than for either $\text{Ba}_2\text{FeReO}_6$ or $\text{Sr}_2\text{CrReO}_6$.

Magnetic Properties. Each of the $\text{Sr}_2\text{FeReO}_6$, $\text{Ba}_2\text{FeReO}_6$ and $\text{Sr}_2\text{CrReO}_6$ double-perovskites exhibits a high-temperature magnetic ordering that stems from the ferromagnetic

arrangement of localized spins on $\text{Fe}^{3+}/\text{Cr}^{3+}$ ($S = 5/2$ and $3/2$, respectively) that are ferromagnetically coupled via the delocalized and antiparallel Re^{5+} ($S = 1$) spins. Their Curie temperatures are all higher than room temperature, at $T_c = \sim 400\text{K}$, $\sim 303\text{K}$ and $\sim 635\text{K}$, respectively. Thus, in order to determine the effect of the flux reaction conditions on their magnetic properties, measurements of their magnetization versus applied field was measured, shown in Figures 5.9, 5.10 and 5.11. Summarized in Table 5.4 are the measured spontaneous and remanent magnetization (M_s and M_r respectively), the coercive field (H_c), and the % ordering of the B/B' cation sites as obtained from the powder X-ray refinements. However, at the maximum applied field of 7 Tesla, magnetization saturation cannot be completely reached for any of the compounds. Previous reports have shown that their maximum saturation magnetization can typically only be achieved by high magnetic fields approaching ~ 30 Tesla.^{22,23} The magnetization at 7 Tesla for all of the flux-prepared $\text{Sr}_2\text{FeReO}_6$ products ranged from ~ 1.57 - $2.17 \mu_B$ and were lower than the expected $3.0 \mu_B$ from the antiparallel alignment of the $\text{Fe}^{3+}/\text{Re}^{5+}$ spins. Lower than expected values for the saturation magnetization has also been previously correlated with the extent of B/B' site disorder.^{8,24} However, in these cases the % B/B' site disorder is relatively constant at $\sim 83 - 84\%$. In the case of $\text{Sr}_2\text{FeMoO}_6$, decreased particle sizes have also been found to increase the amount of magnetically-disordered grain boundaries and thus found to also contribute to a decreased saturation magnetization.^{3,10,25,26} The flux synthesis of $\text{Sr}_2\text{FeReO}_6$ showed the largest range of attainable particle sizes, but any such relationships in the magnetic data remain unclear. For the $\text{Ba}_2\text{FeReO}_6$ flux-prepared products, a smaller H_c and larger M_s values of from $\sim 2.10 - 2.40 \mu_B$ were observed. In this case, the higher Fe/Re site ordering of the cations results in

significantly higher M_s and M_r values, but a lower H_c as compared to Sr_2FeReO_6 . Further, the larger particle sizes of Ba_2FeReO_6 also serve to decrease the amount of grain boundaries that are magnetically-disordered, as described above. The decreased particle sizes of the quenched Ba_2FeReO_6 sample also show the clear trend toward smaller M_s value, though the % B/B' ordering is fairly similar. For the flux-prepared Sr_2CrReO_6 products, spontaneous magnetizations of $\sim 0.74 - 0.80 \mu_B$ were smaller than the $1.0 \mu_B$ predicted from the Cr^{3+}/Re^{5+} antiparallel alignment of spins. The M_s and M_r values primarily increased with an increasing % Cr/Re site ordering. In general, the coercivities of the Sr_2CrReO_6 products were much higher than for either Sr_2FeReO_6 or Ba_2FeReO_6 .

For these $A_2BB'O_6$ double-perovskites in their polycrystalline forms, a large magnetoresistance has previously been found that originates from the grain boundaries serving as an insulating barrier in which the tunneling probability of an electron depends on the orientation of their moments between the grains. Current theories show that the size of the intergrain tunneling magnetoresistance (i.e., ITMR) is dependent upon both the percent spin polarization and concentration of grain boundaries. However, while the amount of spin polarization has been reportedly adjusted up to near 100% with the appropriate combination of A/B/B' cations,³ The modulation of the grain boundaries through variations in particle sizes and surfaces has been restricted because of their conventional solid-state syntheses. Thus, the flux-prepared Sr_2FeReO_6 , Ba_2FeReO_6 , and Sr_2CrReO_6 particles were pressed into polycrystalline pellets without annealing and their temperature-dependent resistivities were measured. The resistivities of Sr_2FeReO_6 prepared by both solid-state and a 1:1 flux for 3 h, Ba_2FeReO_6 synthesized using a 1:1 flux radiatively cooled and Sr_2FeReO_6 at a 1:1 flux

radiatively cooled are compared in Figure 5.12. All samples exhibit a semiconducting-type behavior, but with the flux-preparations having greater temperature dependence and resistivity about 3x higher than that of the solid-state sample, at $\sim 0.38 - 0.12 \text{ } \Omega\text{cm}$ (from 300 – 550K) and $\sim 0.14 - 0.05 \text{ } \Omega\text{cm}$, respectively. The resistivity of the flux-prepared $\text{Ba}_2\text{FeReO}_6$, and $\text{Sr}_2\text{CrReO}_6$ products were a lower $\sim 1.0 - 0.40 \text{ } \Omega\text{cm}$ (300 – 550K) and a higher $\sim 13 - 3 \text{ } \Omega\text{cm}$, respectively. These measured resistivities are roughly 2 - 5 \times larger than the previously reported literature values,^{2,4,27,28} and which arises from the increased concentration of grain boundaries. The latter is based on the fact that a higher resistance is associated with a higher concentration of insulating grain boundaries, but which also enhances the extent of the spin-dependent intergrain tunneling between particles.

Magnetoresistance measurements were taken with the application of a 3 kG magnetic field, with each exhibiting a remarkably large magnetoresistance that can be adjusted between $\sim 40 - 70\%$ at room temperature depending on the particular double-perovskite and the flux synthesis conditions. Shown in Figure 5.13, the magnetic-field dependence of the resistivity has been measured for both the solid-state and flux-prepared $\text{Sr}_2\text{FeReO}_6$ particles. The higher resistivity of the flux-prepared $\text{Sr}_2\text{FeReO}_6$ is accompanied by a slightly larger change in resistance with the magnetic field. This based on the fact that a higher resistance is associated with a higher concentration of insulating grain boundaries, but which also serves to likely enhance the extent of the spin-dependent intergrain tunneling between particles. Both $\text{Ba}_2\text{FeReO}_6$ and $\text{Sr}_2\text{CrReO}_6$ exhibit a similarly large ITMR at room temperature of up to $\sim 65\%$ and $\sim 70\%$ respectively, given in the Supporting Information. Such large polycrystalline magnetoresistances at low magnetic fields have only been previously reported

for the more intensely studied $\text{Sr}_2\text{FeMoO}_6$ (ITMR of $\sim 20 - 30\%$ at 4 kG) when prepared as nanoscale particle grains of $\sim 29 - 45$ nm.¹⁰

CONCLUSIONS

The first flux-mediated syntheses have been investigated for three reduced Re-based members of the double-perovskite $\text{A}_2\text{BB}'\text{O}_6$ family, $\text{Sr}_2\text{FeReO}_6$, $\text{Ba}_2\text{FeReO}_6$ and $\text{Sr}_2\text{CrReO}_6$. Rapid and efficient single-step reactions are demonstrated herein using a eutectic NaCl/KCl mixture that can be used to achieve a high purity and homogeneous distribution of particle sizes that are tunable between ~ 50 nm to > 1 μm . Smaller particles could be obtained by increasing the flux ratio. Samples with smaller particle sizes have a greater concentration of grain boundaries and resulted in larger temperature dependent resistivities compared to solid-state samples. This new synthetic route enables deeper investigations of the effects of particle sizes and % B/B' site ordering on their magnetic properties.

ACKNOWLEDGEMENTS

Financial support from the National Science Foundation (DMR-0644833) and access to a SQUID magnetometer (D. Shultz).

Table 5.1. Powder X-ray diffraction refinement results for lattice constants and B/B' site ordering in Sr₂FeReO₆ (Space group *I4/m*).

Sr ₂ FeReO ₆ ^a	0.5:1, 3 h	0.5:1, 12 h	1:1, 3 h	1:1, 12 h	Solid State
	<u>Lattice Constants</u>				
<i>a</i> (Å)	5.5672(3)	5.5644(4)	5.5649(4)	5.5655(2)	5.5585(3)
<i>c</i> (Å)	7.9003(8)	7.8962(8)	7.8986(9)	7.8990(7)	7.8969(5)
	<u>Fractional B and B' Site Occupancies</u>				
<u>Site (x, y, z)</u>					
Fe1 (0,0,0)	0.8354(3)	0.8440(3)	0.8391(2)	0.8476(2)	0.9702(2)
Re1 (0,0,0)	0.1654(3)	0.1559(3)	0.1609(2)	0.1523(2)	0.0297(2)
Re2 (0,0,0.5)	0.8354(3)	0.8440(3)	0.8391(2)	0.8476(2)	0.9702(2)
Fe (0,0,0.5)	0.1654(3)	0.1559(3)	0.1609(2)	0.1523(2)	0.0297(2)

^a Synthesis conditions given in terms of flux ratio (#:#) and reaction time (#h).

Table 5.2. Powder X-ray diffraction refinement results for lattice constants and B/B' site ordering in Ba₂FeReO₆ (Space group *Fm-3m*)

Ba ₂ FeReO ₆	1:1, 6 h	3:1, 6 h	3:1,6 h quench	3:1,6 h, 24 h
	<u>Lattice Constant</u>			
<i>a</i> (Å)	8.0540(3)	8.0533(3)	8.0536(4)	8.0548(7)
	<u>Fractional B and B' Site Occupancies</u>			
<u>Site (x, y, z)</u>				
Fe1 (0,0,0)	0.90627(6)	0.94088(4)	0.90504(5)	0.96947(5)
Re1 (0,0,0)	0.09373(6)	0.05912(4)	0.09496(5)	0.03053(5)
Re2 (0.5,0.5,0.5)	0.90627(6)	0.94088(4)	0.90504(5)	0.96947(5)
Fe2 (0.5,0.5,0.5)	0.09373(6)	0.05912(4)	0.09496(5)	0.03053(5)

^a Synthesis conditions given in terms of flux ratio (#:#) and reaction time (#h).

Table 5.3. Powder X-ray diffraction refinement results for lattice constants and B/B' site ordering in Sr₂CrReO₆ (Space group *Fm-3m*)

Sr ₂ CrReO ₆	1:1, 6 h	3:1, 6 h	3:1,6 h, quench	1:1,6 h, 48 h
	<u>Lattice Constant</u>			
<i>a</i> (Å)	7.8077(5)	7.8080(3)	7.8075(5)	7.8085(5)
	<u>Fractional B and B' Site Occupancies</u>			
<u>Site (x, y, z)</u>				
Cr1 (0,0,0)	0.87343(5)	0.84815(3)	0.83813(4)	0.9007(3)
Re1 (0,0,0)	0.12657(5)	0.15186(3)	0.16187(4)	0.0993(3)
Re2 (0.5,0.5,0.5)	0.87343(5)	0.84815(3)	0.83813(4)	0.9007(3)
Cr2 (0.5,0.5,0.5)	0.12657(5)	0.15186(3)	0.16187(4)	0.0993(3)

^a Synthesis conditions given in terms of flux ratio (#:#) and reaction time (#h).

Table 5.4. Magnetic properties of the flux-prepared double-perovskites, including spontaneous and remanent magnetization (M_s and M_r respectively) and coercive field (H_c). Also shown are the fractional site occupancies of B/B' cations obtained by PXRD refinements.

Flux Preparation	(ratio, time)	M_s	H_c (T)	M_r (μ_B / F.U.)	B/B' ordering (%)
Sr ₂ FeReO ₆	0.5:1, 3 h	2.17	0.51	0.39	83.54(3)
	0.5:1, 12 h	1.57	0.31	0.37	84.40(3)
	1:1, 3 h	1.87	0.38	0.45	83.91(2)
	1:1, 12 h	1.96	0.41	0.48	84.76(2)
Ba ₂ FeReO ₆	1:1, 6 h	2.40	0.18	0.98	90.627(6)
	3:1, 6 h	2.32	0.25	0.98	94.088(4)
	3:1, 6 h, (24 h)	2.10	0.25	0.87	96.947(5)
	3:1, 6 h (quench)	2.16	0.25	0.92	90.504(5)
Sr ₂ CrReO ₆	1:1, 6 h	0.80	1.79	0.50	87.343(5)
	3:1, 6 h	0.77	1.91	0.48	84.815(3)
	3:1, 6 h (quench)	0.74	2.53	0.46	83.813(4)
	1:1, 6 h, (48 h)	0.79	2.41	0.50	90.07(3)

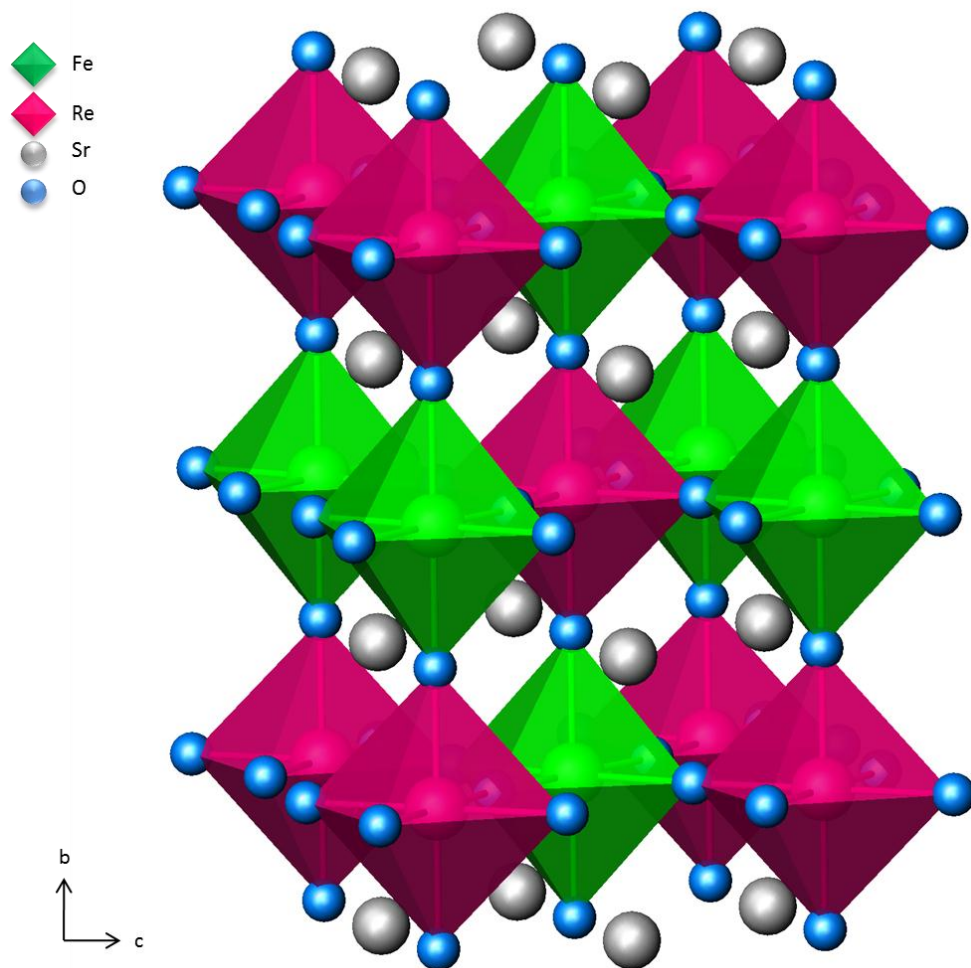


Figure 5.1. Crystal structure of $\text{Sr}_2\text{FeReO}_6$. FeO_6 polyhedra are shown in green, ReO_6 octahedra are shown in pink, Sr atoms are shown in grey and oxygen atoms are shown in blue.

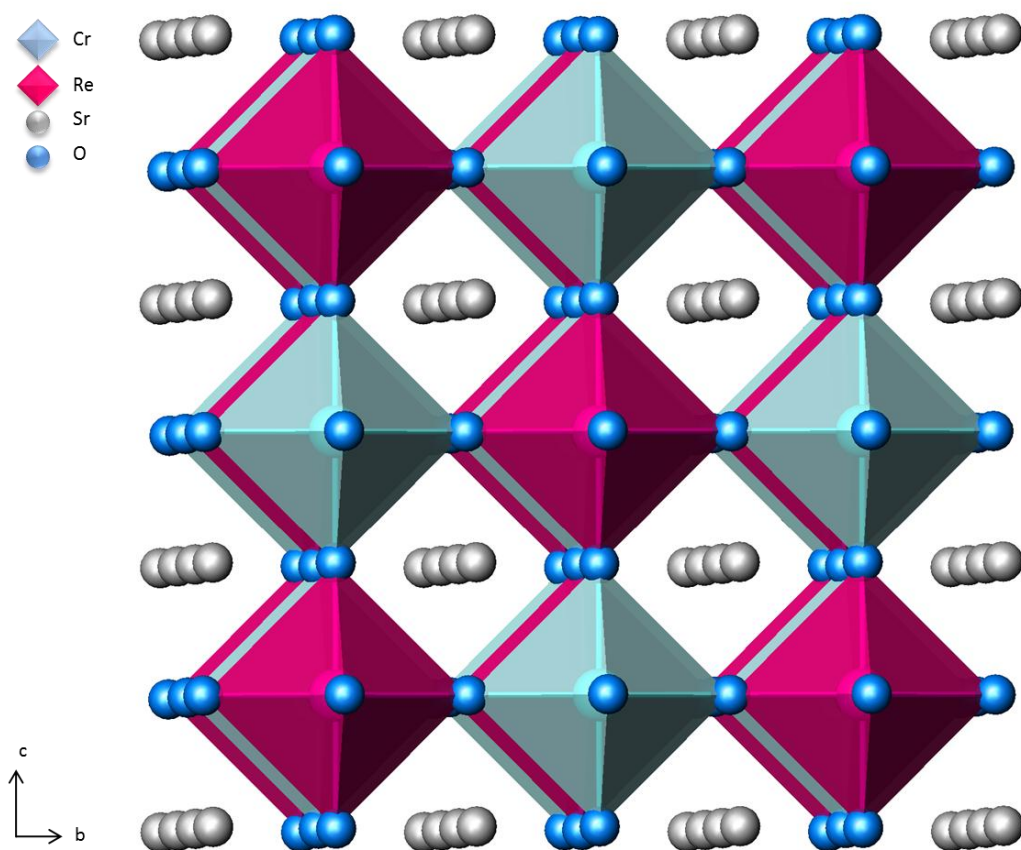


Figure 5.2. Crystal structure of $\text{Sr}_2\text{CrReO}_6$. CrO_6 polyhedra are shown in light blue, ReO_6 octahedra are shown in pink, Sr atoms are shown in grey and oxygen atoms are shown in blue.

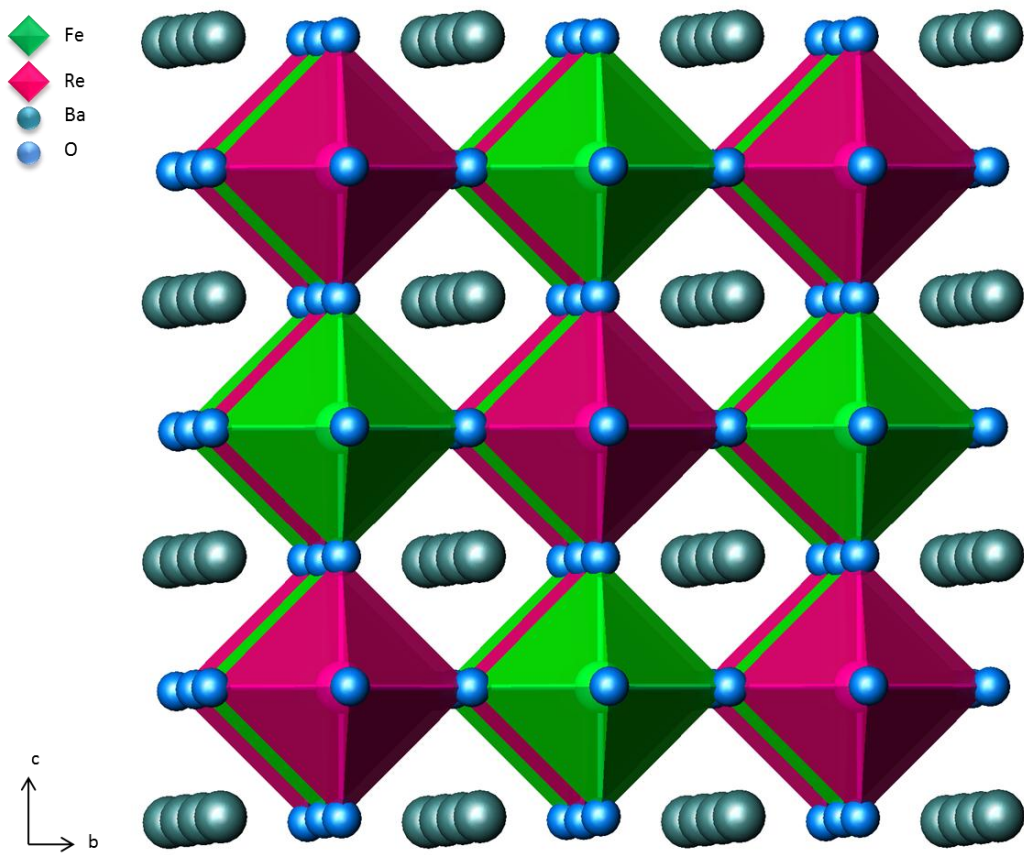


Figure 5.3. Crystal structure of Ba₂FeReO₆. FeO₆ polyhedra are shown in green, ReO₆ octahedra are shown in pink, Ba atoms are shown in dark green and oxygen atoms are shown in blue.

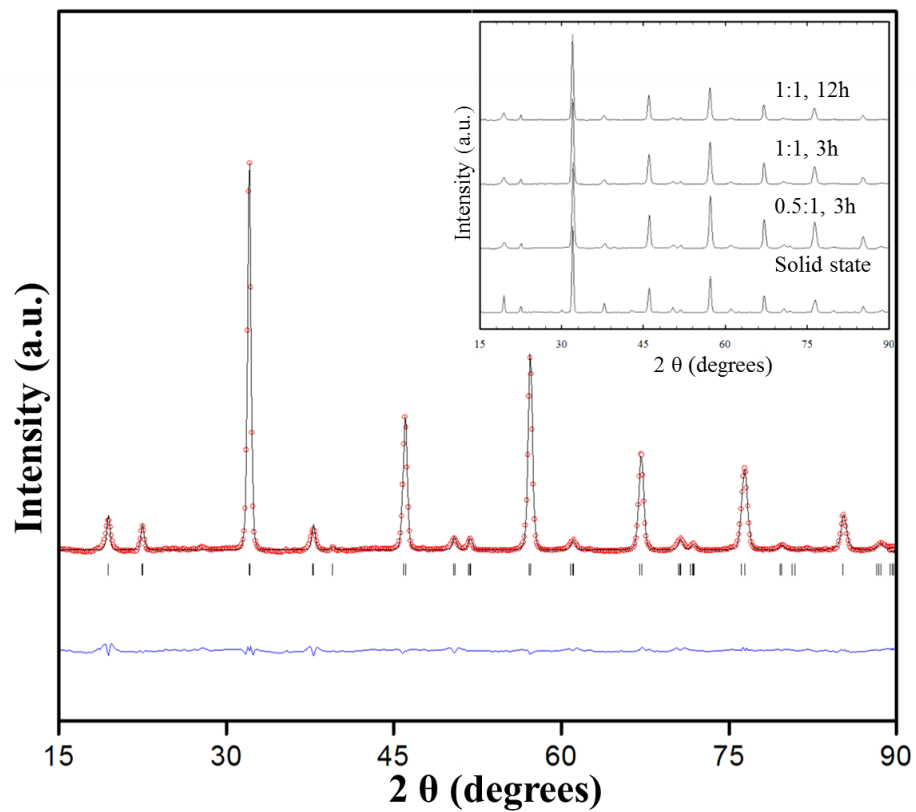


Figure 5.4. PXRD Rietveld refinement results for $\text{Sr}_2\text{FeReO}_6$ synthesized using a 0.5:1 flux for 12 h. The observed profile is indicated by the circles and the calculated profile by the solid line. Bragg peak positions are indicated by vertical peaks. The difference diffractogram is shown at the bottom.

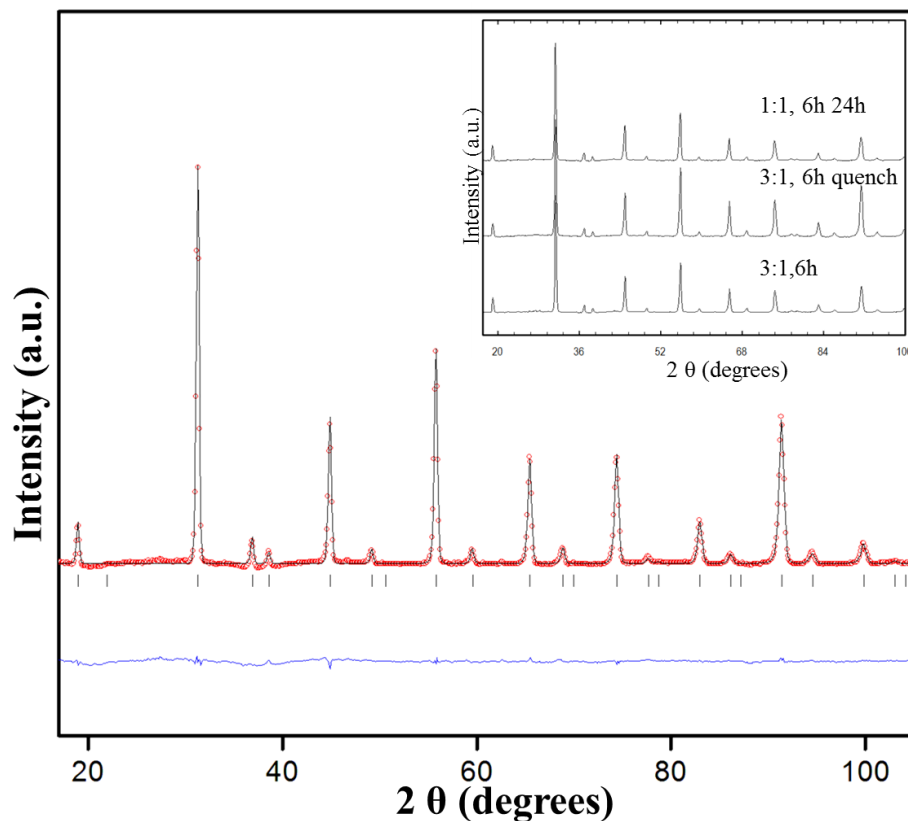


Figure 5.5. PXRd Rietveld refinement results for Ba₂FeReO₆ synthesized using a 1:1 flux and radiatively cooled. The observed profile is indicated by the circles and the calculated profile by the solid line. Bragg peak positions are indicated by vertical peaks. The difference diffractogram is shown at the bottom.

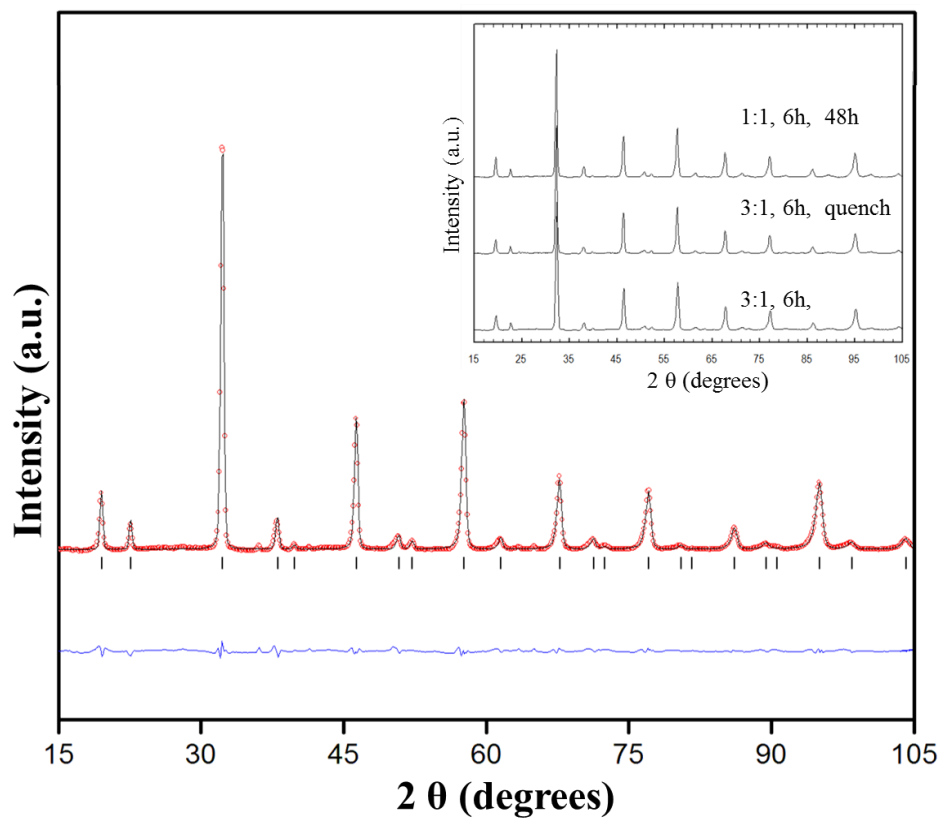


Figure 5.6. PXRD Rietveld refinement results for $\text{Sr}_2\text{CrReO}_6$ synthesized using a 1:1 flux radiatively cooled. The observed profile is indicated by the circles and the calculated profile by the solid line. Bragg peak positions are indicated by vertical peaks. The difference diffractogram is shown at the bottom.

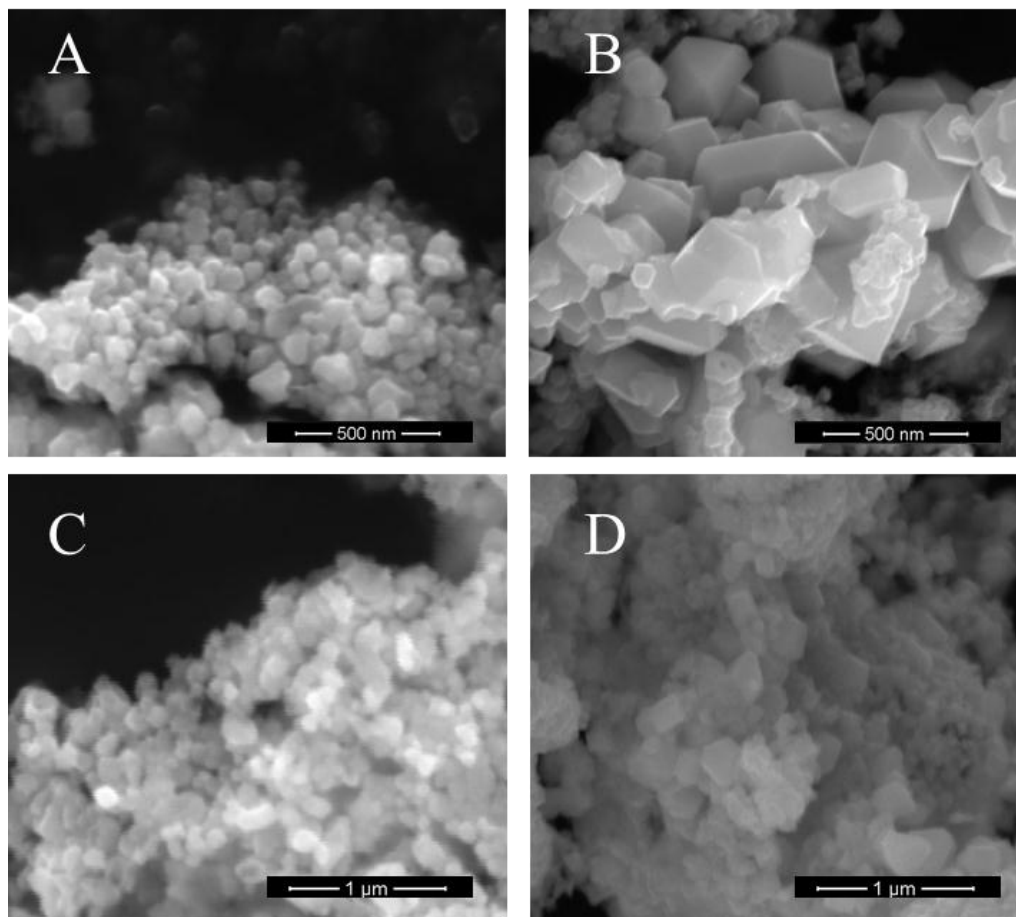


Figure 5.7. SEM images for $\text{Sr}_2\text{FeReO}_6$ synthesized using a molten NaCl/KCl flux at (A) a 0.5:1 ratio for 3 h, (B) 0.5:1 ratio for 12 h, (C) a 1:1 ratio for 3 h, and (D) a 1:1 ratio for 12 h.

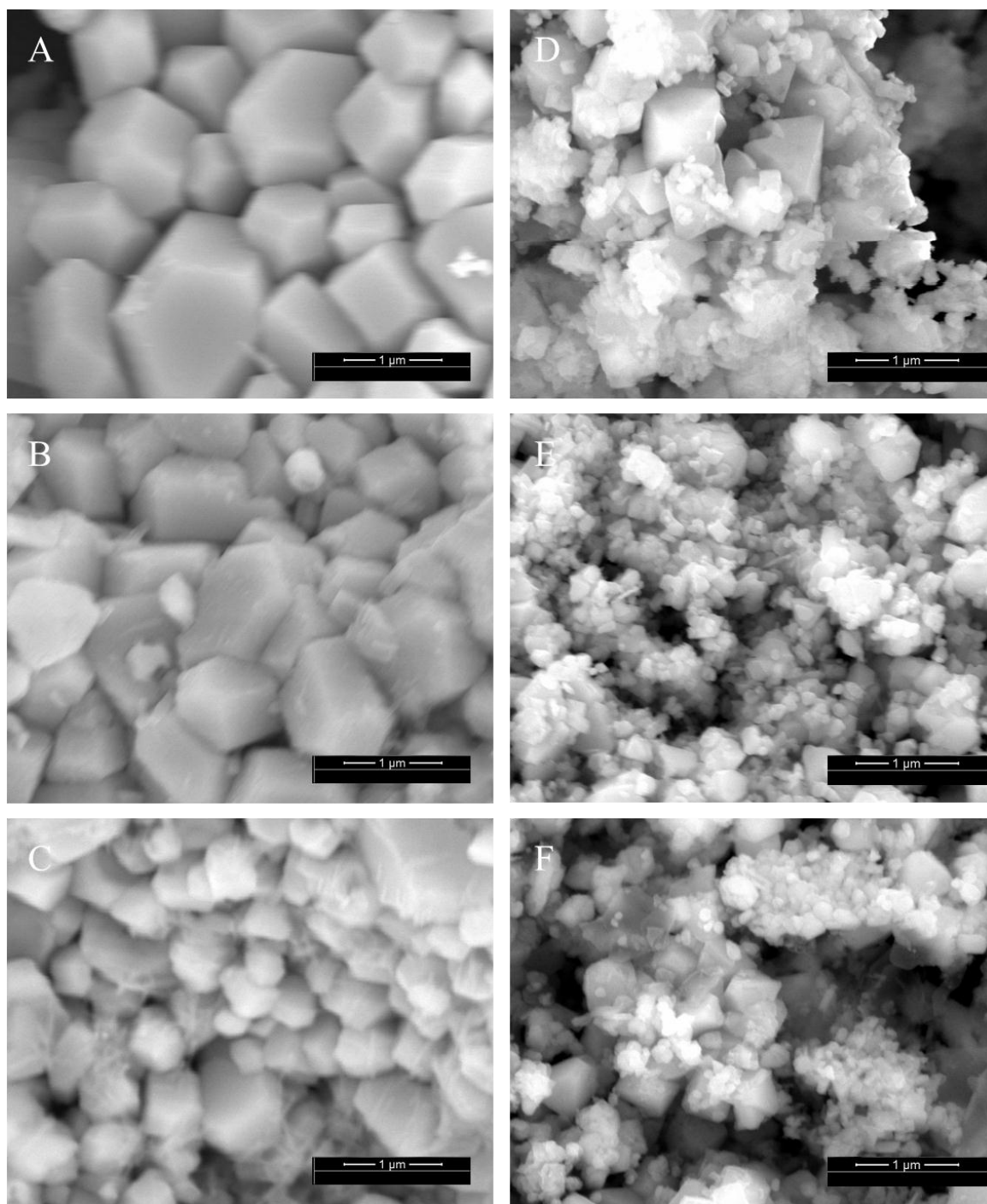


Figure 5.8. SEM images for $\text{Ba}_2\text{FeReO}_6$ synthesized using a molten NaCl/KCl flux at (A) a 1:1 ratio for 6 h, (B) 3:1 ratio for 6 h, (C) a 3:1 ratio for 6 h and quenching; $\text{Sr}_2\text{CrReO}_6$ using (D) a 1:1 ratio for 6 h, (E) a 1:1 ratio and slow cooling over 24 h and (F) a 3:1 ratio for 6 h and quenching. Samples in A, B and D were radiatively cooled.

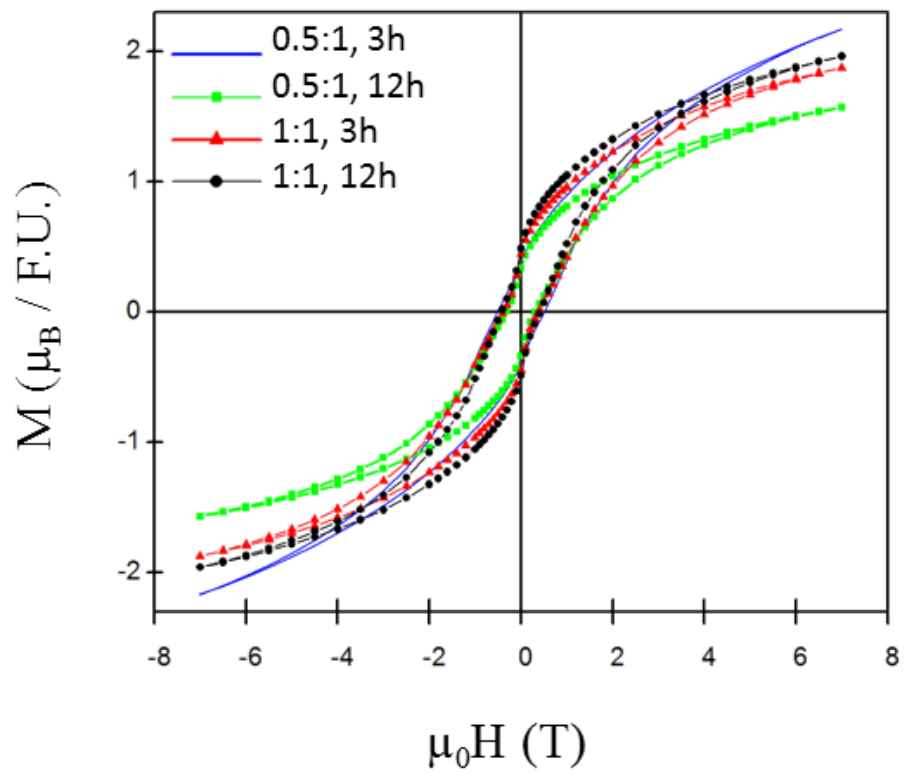


Figure 5.9. $M(H)$ curves for $\text{Sr}_2\text{FeReO}_6$ synthesized using a molten NaCl/KCl flux at 750°C at a 0.5:1 and 1:1 ratio for both 3 h and 12 h.

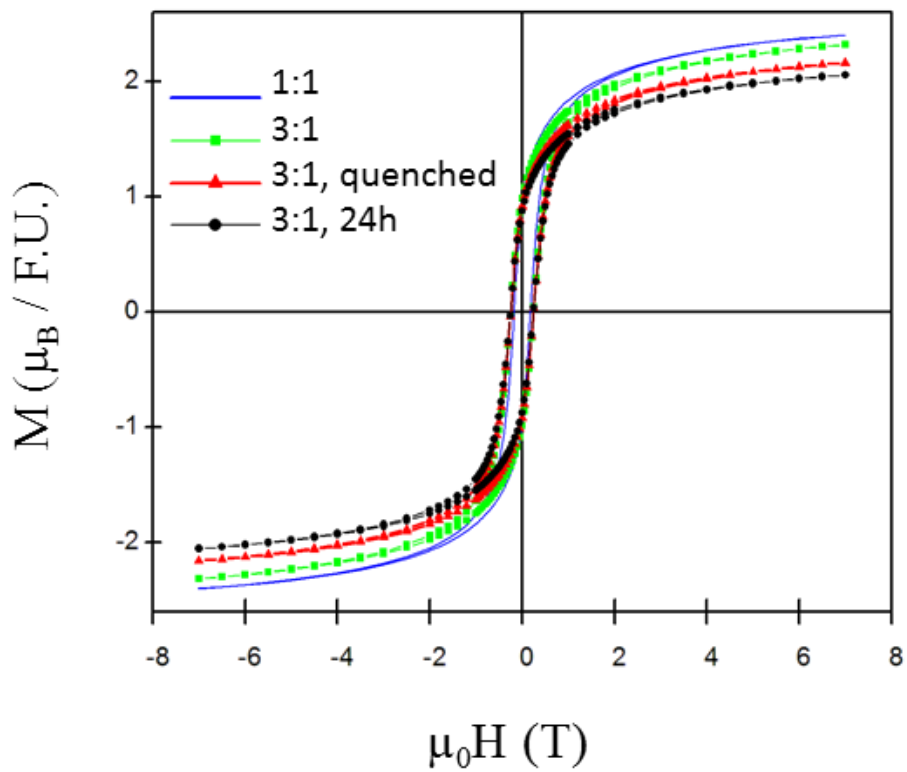


Figure 5.10. $M(H)$ curves for $\text{Ba}_2\text{FeReO}_6$ synthesized using a molten NaCl/KCl flux at 800°C at a 1:1 flux ratio for 6 h and 3:1 flux ratio for 6 h radiatively cooling, a 3:1 flux ratio for 6 h rapidly quenched, and a 1:1 flux ratio for 6 h slow cooled over 24 h.

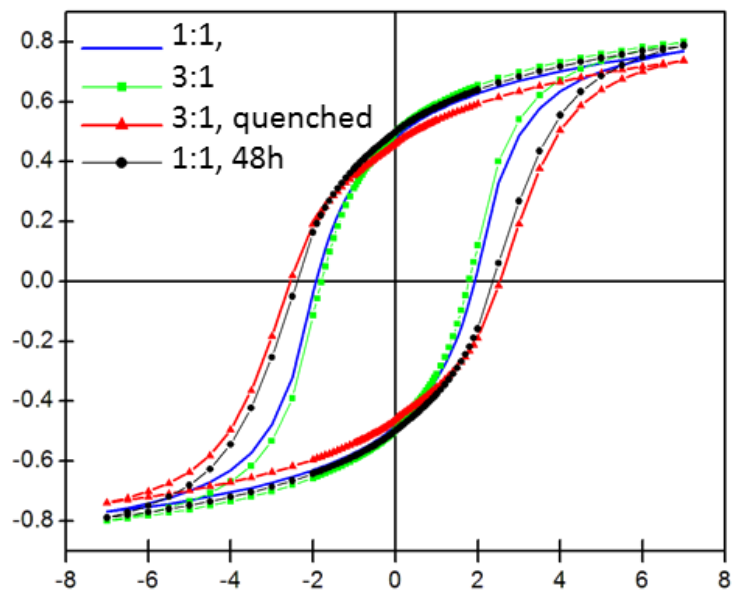


Figure 5.11. $M(H)$ curves for $\text{Sr}_2\text{CrReO}_6$ synthesized using a molten NaCl/KCl flux at 800°C at a 1:1 flux ratio for 6 h and 3:1 flux ratio for 6 h radiatively cooled, a 3:1 flux ratio for 6 h and rapidly quenched, and a 1:1 flux ratio for 6 h and slowly cooled over 2 days.

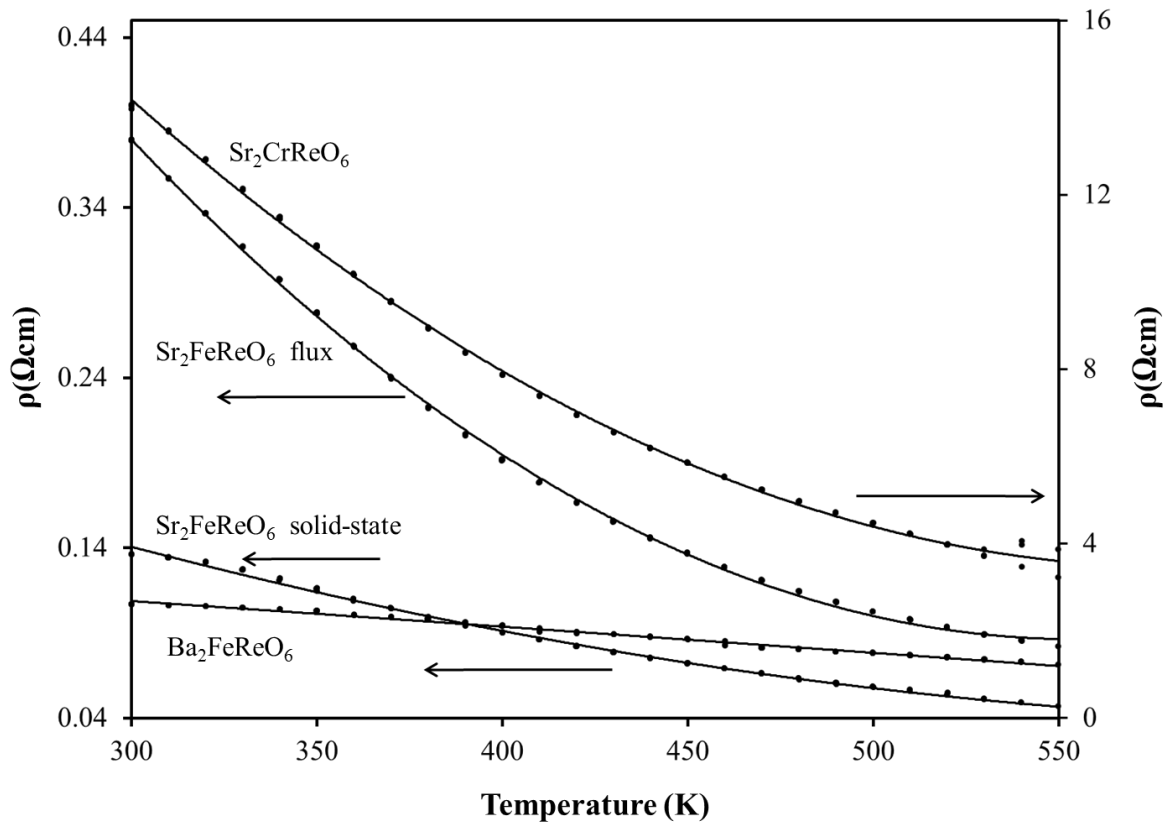


Figure 5.12. Temperature dependence of the resistivity for Sr₂FeReO₆ synthesized by the solid state method and at a 1:1 flux for 3 h; Ba₂FeReO₆ at a 1:1 flux for 6 h and radiatively cooled and Sr₂CrReO₆ at a 1:1 flux for 6 h and radiatively cooled.

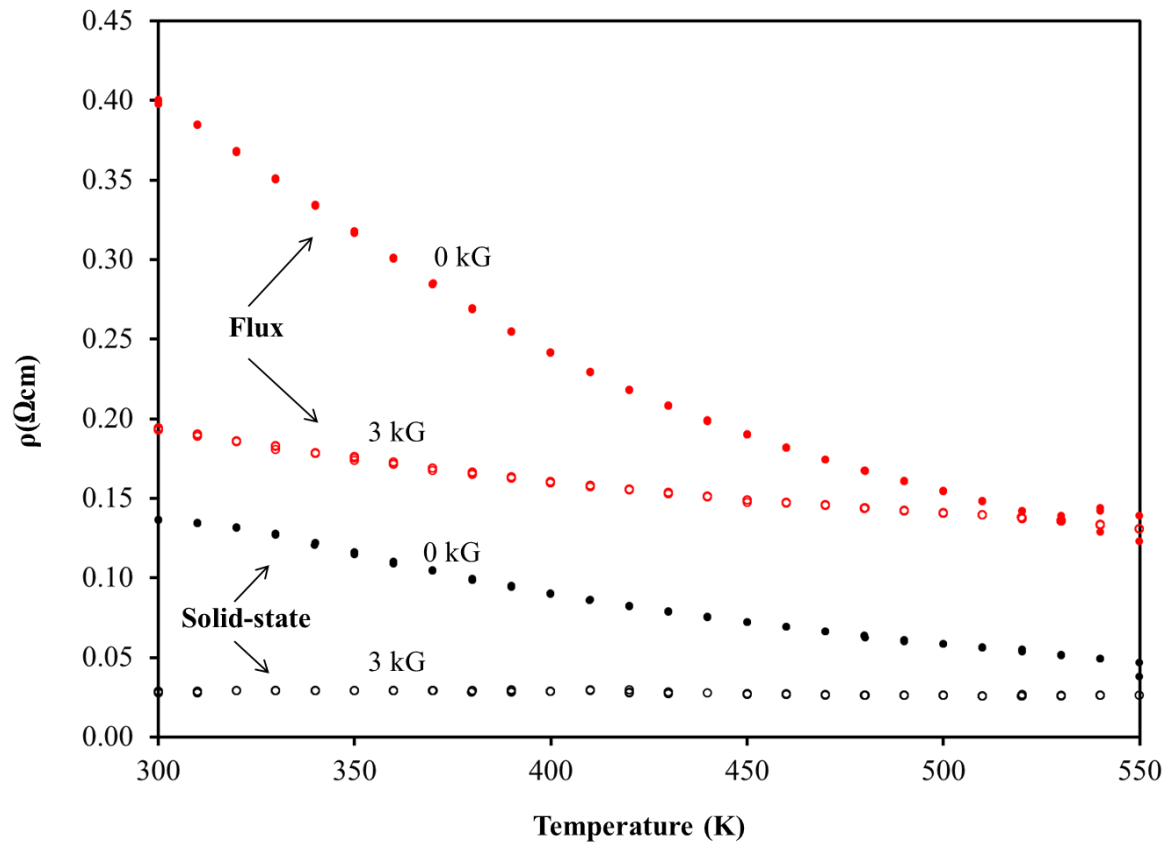


Figure 5.13. Temperature and magnetic-field dependence of the resistivity for polycrystalline $\text{Sr}_2\text{FeReO}_6$ pellets prepared via the solid-state and flux-synthetic routes (1:1 molar ratio, 3 h).

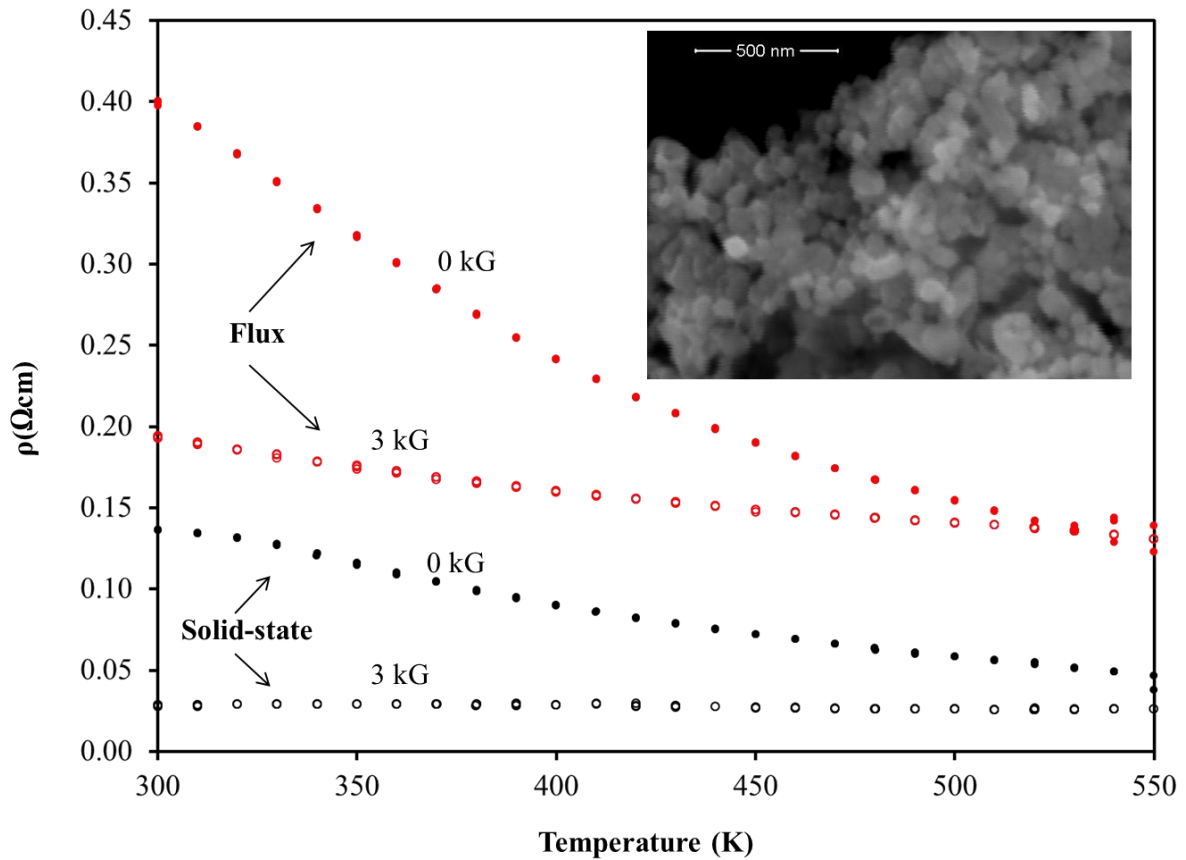


Figure 5.14. An SEM image of $\text{Sr}_2\text{FeReO}_6$ synthesized in high-purity in a NaCl/KCl flux at 750°C for 3 h with homogeneous particles ranging from $\sim 50 - 100$ nm in size. Temperature and magnetic-field dependence of the electrical resistivity for polycrystalline $\text{Sr}_2\text{FeReO}_6$ pellets prepared via the solid-state and flux-synthetic routes (1:1 molar ratio, 3 h).

SUPPORTING INFORMATION

“Rapid Molten-salt Syntheses of Sr₂FeReO₆, Ba₂FeReO₆ and Sr₂CrReO₆: Particle Sizes,
B/B'-site Disorder, and Magnetic Properties”

Lindsay Fuoco, Dianny Rodriguez, Tim Peppel and Paul A. Maggard

Department of Chemistry, North Carolina State University, Raleigh, NC 27695

Table 5.S1. PXRD refinement data for Ba₂FeReO₆.

Ba ₂ FeReO ₆				
fw	612.7			
Space group, <i>Z</i>	<i>F m-3m</i>			
Radiation	K α_1 = 1.54059 Å, K α_1 /K α_2 = 1.996			
	1:1	3:1	3:1, quenched	3:1, 24 h
Unit cell, <i>a</i> Å	8.0540(3)	8.0533(3)	8.0536(4)	8.0548(7)
2 θ range	16.5-110.0	14.0-115.0	16.5-110.0	16.5-110.0
Number of data points	936	1011	936	936
Number of variables	32	24	16	28
Background polynomial	8	8	9	8
R _{wp}	1.39%	1.71%	1.99%	1.83%
R _{exp}	2.17%	2.78%	2.24%	1.46%

Table 5.S2. PXRD refinement data for Sr₂FeReO₆.

Sr ₂ FeReO ₆					
fw	513.2				
Space group, <i>Z</i>	<i>I</i> 4/ <i>m</i>				
Radiation	K α_1 = 1.54059 Å, K α_1 /K α_2 = 1.996				
	0.5:1, 3 h	0.5:1, 12 h	1:1, 3 h	1:1, 12 h	Solid state
Unit cell, <i>a</i> Å	5.5672(3)	5.5644(4)	5.5649(4)	5.5655(2)	5.5585(3)
<i>c</i>	7.9003(8)	7.8962(8)	7.8986(9)	7.8990(7)	7.8969(5)
2 θ range	14.0-110.0	12.9-92.0	10.2-95.0	120.0-90.0	10.2-95.0
Number of data points	961	792	849	781	849
Number of variables	24	30	27	16	27
Background polynomial	9	6	8	7	8
R _{wp}	2.19%	1.8%	2.64%	2.5%	2.37%
R _{exp}	1.68%	1.41%	3.47%	1.37%	3.1%

Table 5.S3. PXRD refinement data for Sr₂CrReO₆.

Sr ₂ CrReO ₆				
fw	509.4			
Space group, <i>Z</i>	<i>F m-3m</i>			
Radiation	K α_1 = 1.54059 Å, K α_1 /K α_2 = 1.996			
	1:1	3:1	3:1, quenched	1:1, 48 h
Unit cell, <i>a</i> Å	7.8077(5)	7.8080(3)	7.8075(5)	7.8085(5)
2 θ range	12.0-105.0	13.0-110.0	14.0-115.9	13.0-115.0
Number of data points	931	971	1021	1021
Number of variables	28	9	12	23
Background polynomial	9	7	8	8
R _{wp}	2.57%	2.72%	2.95%	2.85%
R _{exp}	1.66%	1.96%	1.23%	1.77%

Table 5.S4. PXRD refinement results including thermal parameters for Sr₂FeReO₆ synthesized using a 0.5:1 flux for 12 h, Ba₂FeReO₆ at a 1:1 flux for 6 h radiatively cooled and Sr₂CrReO₆ at a 1:1 flux for 6 h radiatively cooled.

Compound	Atoms	x	y	z	Occupancy	B (Å ²)
Sr ₂ FeReO ₆ <i>I4/m</i> <i>a</i> (Å)= 5.5644(4) <i>c</i> (Å)= 7.8962(8)	Sr	0	0.5	0.25	1	0.51(6)
	Fe1	0	0	0	0.8440(3)	0.3(1)
	Re1	0	0	0	0.1559(3)	0.3(1)
	Re2	0	0	0.5	0.8440(3)	0.36(7)
	Fe2	0	0	0.5	0.1559(3)	0.36(7)
	O1	0	0	0.250(3)	1	1.1(1)
	O2	0.266(5)	0.230(4)	0	1	1.1(1)
Ba ₂ FeReO ₆ <i>Fm-3m</i> <i>a</i> = 8.0540(3)	Ba	0.25	0.25	0.25	1	0.67(9)
	Fe1	0	0	0	0.90627(6)	0.3(1)
	Re1	0	0	0	0.09373(6)	0.3(1)
	Re2	0.5	0.5	0.5	0.90627(6)	0.37(7)
	Fe2	0.5	0.5	0.5	0.09373(6)	0.37(7)
	O	0.2590(7)	0	0	1	1.4(1)
Sr ₂ CrReO ₆ <i>Fm-3m</i> <i>a</i> = 7.8077(5)	Sr	0.25	0.25	0.25	1	0.50(5)
	Cr1	0	0	0	0.87343(5)	1.2(1)
	Re1	0	0	0	0.12657(5)	1.2(1)
	Re2	0.5	0.5	0.5	0.87343(5)	0.72(7)
	Cr2	0.5	0.5	0.5	0.12657(5)	0.72(7)
	O	0.2479(6)	0	0	1	0.84(9)

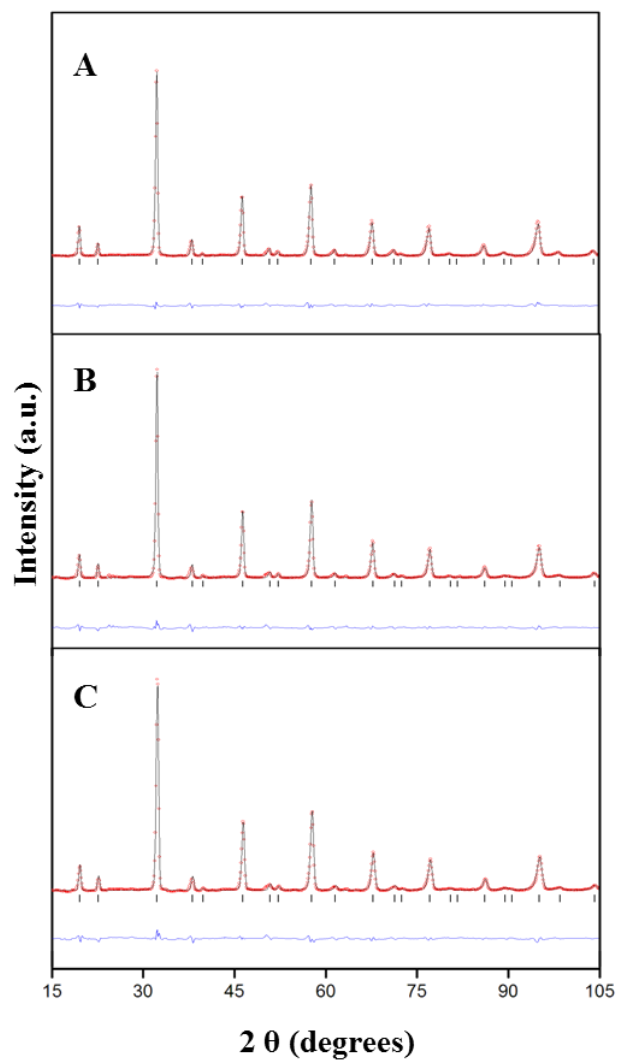


Figure 5.S1. PXR D Rietveld refinement results for $\text{Sr}_2\text{CrReO}_6$ synthesized using a molten NaCl/KCl flux at (A) a 1:1 flux for 6 h and slow cooling over 2 days, (B) a 3:1 flux for 6 h and rapidly quenched and (C) a 3:1 flux for 6 h radiatively cooled. The observed profile is indicated by the circles and the calculated profile by the solid line. Bragg peak positions are indicated by vertical peaks. The difference diffractogram is shown at the bottom.

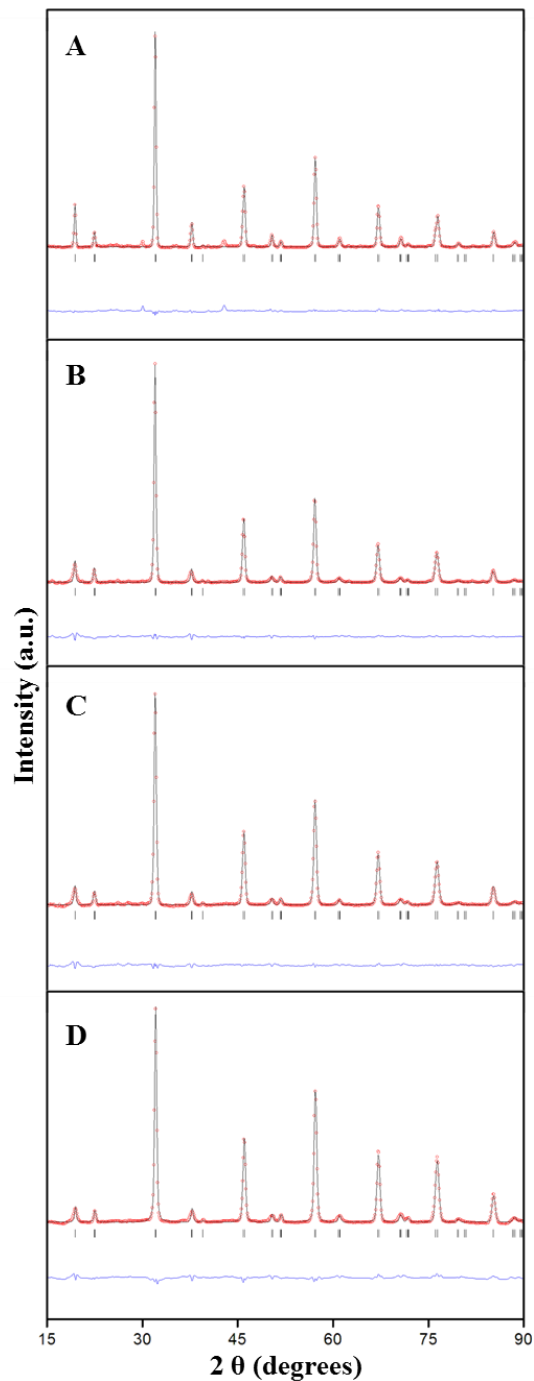


Figure 5.S2. PXR D Rietveld refinement results for $\text{Sr}_2\text{FeReO}_6$ synthesized by (A) solid state method; using a molten NaCl/ KCl flux at (B) a 1:1 flux for 12 h, (C) a 1:1 flux for 3 h and (D) a 0.5:1 flux for 3 h. The observed profile is indicated by the circles and the calculated profile by the solid line. Bragg peak positions are indicated by vertical peaks. The difference diffractogram is shown at the bottom.

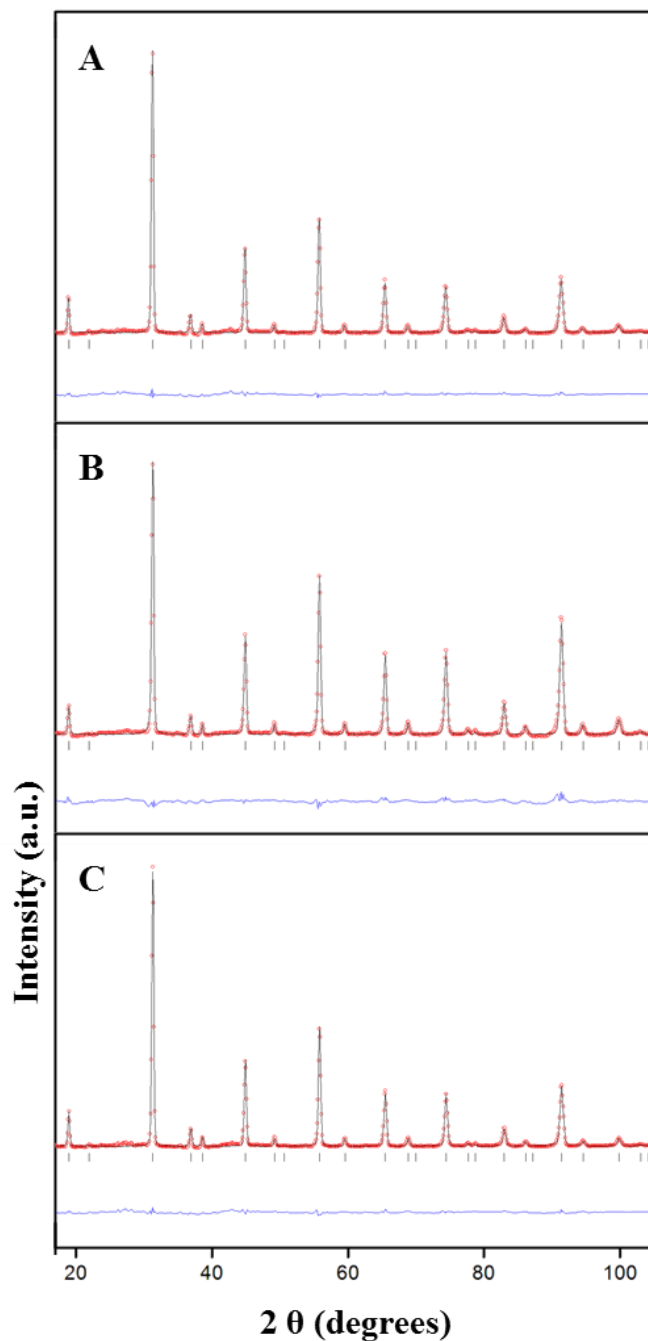


Figure 5.S3. PXRd Rietveld refinement results for $\text{Ba}_2\text{FeReO}_6$ synthesized by using a molten NaCl/KCl flux at (A) a 3:1 flux for 6 h and slow cooling over 24 h, (B) a 3:1 flux for 6 h and rapidly quenched and (C) a 3:1 flux for 6 h radiatively cooled. The observed profile is indicated by the circles and the calculated profile by the solid line. Bragg peak positions are indicated by vertical peaks. The difference diffractogram is shown at the bottom.

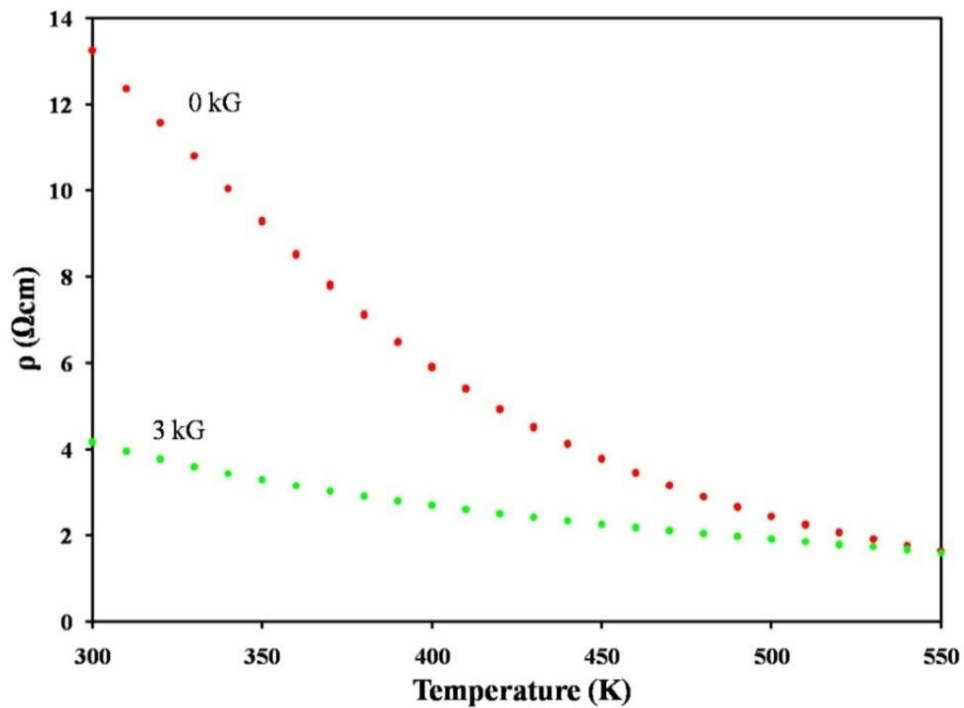


Figure 5.S4. Temperature-dependent resistivity measurements at 0 kG and 3 kG for $\text{Sr}_2\text{CrReO}_6$ particles prepared by a NaCl/KCl flux synthesis at 800 °C for 6 h using a 1:1 flux:product molar ratio radiatively cooled.

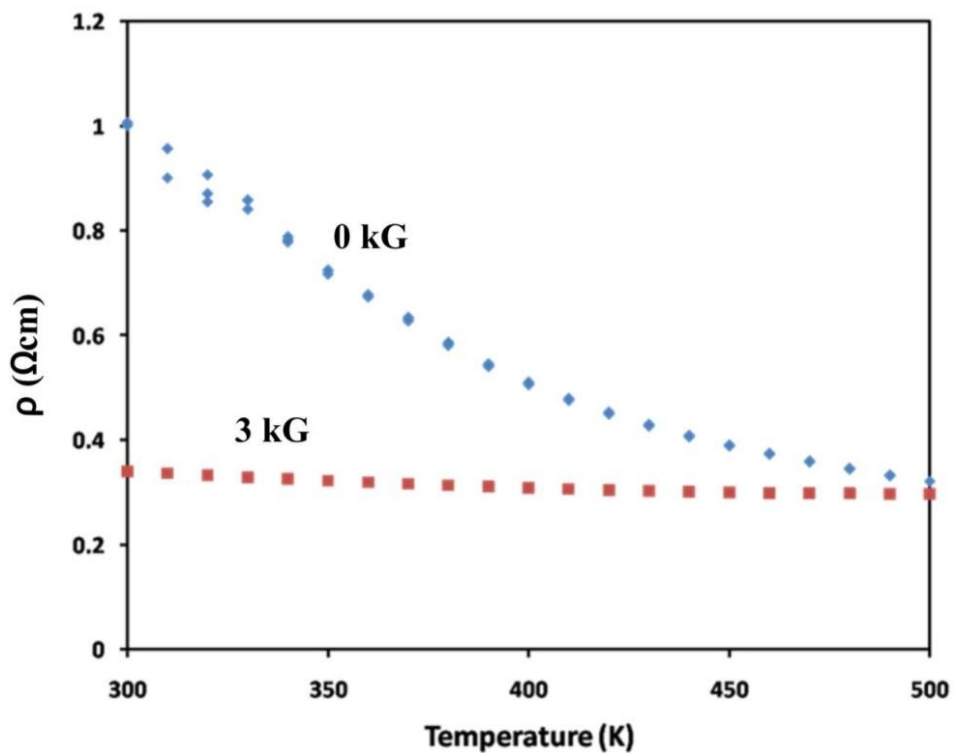


Figure 5.S5. Temperature-dependent resistivity measurements at 0 kG and 3 kG for $\text{Ba}_2\text{FeReO}_6$ particles prepared by a NaCl/KCl flux synthesis at 800 °C for 6 h using a 1:1 flux:product molar ratio radiatively cooled.

REFERENCES

- (1) Kobayashi, K.-I., Kimura, T., Sawada, H., Terakura, K., Tokura, Y. *Nature* **1998**, *395*, 677.
- (2) Kobayashi, K.-I., Kimura, T., Y. Tomioka, H. Swada, K. Terakura, Y. Tokura *Phys. Rev. B* **1999**, *59*, 159.
- (3) Serrate, D., De Teresa, J.M., Ibarra, M.R. *J. Phys.: Condens. Matter* **2007**, *19*, 023201.
- (4) Kato, H., Okuda, T., Okimoto, Y., Tomioka, Y., Oikawa, K., Kamiyama, T., Tokura, Y. *Phys. Rev. B* **2004**, *69*.
- (5) Kato, H., Okuda, T., Okimoto, Y., Tomioka, Y., Takenoya, Y., Ohkubo, A., Kawasaki, M., Tokura, Y. *Appl. Phys. Lett.* **2002**, *81*.
- (6) Tomioka, Y., Okuda, T., Okimoto, Y., Kumai, R., Kobayashi, K.-I. *Phys. Rev. B* **2000**, *61*, 422.
- (7) Hwang, H. Y., Cheong, S.W., Ong, N.P., Batlogg *Phys. Rev. Lett.* **1996**, *77*, 2041.
- (8) Balcells, J.; Navarro, M.; Bibes, M.; Roig, A.; Martinez, B.; Fontcuberta, J. *Appl. Phys. Lett.* **2001**, *78*.
- (9) Jacobo, S. E., Duhalde, S., Mercader, R.C. *physica B* **2004**, *354*, 59.
- (10) Yuan, C. L., Wang, S.G., Song, W.H., Yu, T., Dai, J.M., Ye, S.L., Sun, Y.P. *Appl. Phys. Lett.* **1999**, *75*, 3853.
- (11) Li, X. H., Sun, Y. P., Lu, W. J., Ang, R., Zhang, S. B., Zhu, X. B., Song, W. H., Dai, J. M. *Solid State Commun.* **2008**, *145*, 98.

- (12) Zhong, W., Liu, W., Au, C. T., DU, Y. W. *Nanotechnology* **2006**, *17*, 250.
- (13) Porob, D., Maggard, P. A. *Mater. Res. Bull.* **2006**, *41*, 1513.
- (14) Porob, D., Maggard, P. A. *J. Solid State Chem.* **2006**, *179*, 1727.
- (15) Arney, D., Porter, B., Greve, B., Maggard, P. *J. Photochem. Photobiol. A: Chemistry* **2008**, *199*, 230.
- (16) Arney, D.; Watkins, T.; Maggard, P. A. *J. Am. Ceram. Soc.* **2011**, *94*, 1483.
- (17) Prellier, W., Smolyaninova, V., Biswas, A., Galley, C., Greene, R.L., Ramesha, K., Gopalakrishnan, J. *J. Phys.: Condens. Matter* **2000**, *12*, 965.
- (18) MDI In *Jade 9*; Materials Data Incorporated: **2009**.
- (19) Gopalakrishnan, J., Chattopadhyay, A., Ogale, S.B., Venkatesan, T., Greene, R.L., Millis, A.J., Ramesha, K., Hannoyer, B., Marest, G. *Phys. Rev. B* **2000** 62.
- (20) Retuerto, M., Martinez-Lope, M.J., Garcia-Hernandez, M., Alonso, J.A. *Mater. Res. Bull.* **2009**, *44*, 1261.
- (21) Michalik, J. M. T. J. M., Ritter, C., Blasco, J., Serrate, M.R., Ibarra, M.R., Kapusta, C., Freudenberger, J., Kozlova, N. *Europhys. Lett.* **2007**, *78*.
- (22) Teresa, J. M. M., J. M.; Blasco, J.; Algarabel, P. A.; Ibarra, M. R. *Appl. Phys. Lett* **2007**, *90*.
- (23) Michalik, J. M., De Teresa, J.M., Blasco, J., Algarabel, P.A., Ibarra, M.R., Kapusta, Cz., Zeitler, U. *J. Phys.: Condens. Matter* **2007**, *19*, 1.
- (24) Lin, C., Chu, Y., Wang, S. *Mater. Lett.* **2006**, *60*, 2270.
- (25) Greneche, J. M.; Venkatesan, M.; Suryanarayanan, R.; Coey, J. M. D. *Phys. Rev. B* **2001**, *63*.

- (26) Yin, H. Q.; Zhou, J.-S.; Dass, R.; Zhou, J.-P.; McDevitt, J. T.; Goodenough, J. B. *J. Appl. Phys.* **2000**, *87*.
- (27) Alamelu, M., Varadaraju, U.V., Venkatesan, M., Douvalis, A.P., Coey, J.M.D *J. Appl. Phys.* **2002**, *91*, 8909.
- (28) Teresa, J. M., Serrate, D., Blasco, J., Ibarra, M.R., Morellon, L. *Phys. Rev. B* **2004**, *69*.

CHAPTER 6

CONCLUSIONS

The identification and development of photoelectrode materials capable of solar hydrogen production has been a topic of intense research interest in the field of renewable energy.¹⁻⁴ Metal-oxide based photoelectrodes are particularly attractive due to their relative stability against photocorrosion. However, most current metal-oxides such as *n*-TiO₂ have large bandgaps that restrict their use to ultraviolet-light. An alternative approach is the use of metal oxides composing of Cu(I) and Ta(V) or Nb(V) cations which have reduced bandgap sizes as a result of the creation of a new higher energy valence band created by the introduction of Cu(I) d¹⁰ valence orbitals.^{5,6}

An investigation into the photoelectrochemical properties of reduced bandgap Cu(I) tantalates was presented herein. Polycrystalline films of semiconducting Cu₅Ta₁₁O₃₀ and Cu₃Ta₇O₁₉ were prepared on fluorine-doped tin oxide (FTO) glass starting from their CuCl-flux synthesis. Scanning electron microscopy images revealed films composed of highly-faceted micron-sized particles with thicknesses of ~80 μm. The bulk powders of Cu₅Ta₁₁O₃₀ and Cu₃Ta₇O₁₉ exhibited bandgaps of ~2.59 eV and ~2.47 eV respectively and are located well within the visible-light range. Photoelectrochemical measurements of each under visible-light irradiation showed strong cathodic photocurrents indicative of a *p*-type photoelectrode. Onset of their cathodic photocurrents begins at wavelengths of ~500 – 550

nm, with the highest observed incident-photon-to-current efficiencies of ~5 % at 350 nm and ~1-2 % at 500 – 600 nm. The valence and conduction band positions of each were determined from their flat-band potentials obtained from Mott-Schottky plots, and their positions were determined to be +1.06 V and -1.53 V for $\text{Cu}_5\text{Ta}_{11}\text{O}_{30}$ and +1.19 V and -1.28 V vs. RHE for $\text{Cu}_3\text{Ta}_7\text{O}_{19}$ at pH=6.3. For both phases, the conduction band potentials are located at much more negative potentials than the hydrogen redox potential at this pH and are thus suitable to achieve the reduction of water to hydrogen under visible-light. The location of the conduction and valence band edges of $\text{Cu}_5\text{Ta}_{11}\text{O}_{30}$ and $\text{Cu}_3\text{Ta}_7\text{O}_{19}$ with respect to the water reduction and oxidation potentials are illustrated in Figure 6.1.

The polycrystalline films of $\text{Cu}_5\text{Ta}_{11}\text{O}_{30}$ and $\text{Cu}_3\text{Ta}_7\text{O}_{19}$ could be further enhanced for their observed photocurrent response by increasing the film preparation annealing and oxidation temperatures. Increased annealing temperatures and the mild oxidation of the films led to the significant enhancement of the cathodic photocurrent as a result of better sintering of particles and increased *p*-type dopant concentrations. Current research on the effects of different thicknesses and particle sizes of the films on their stability and cathodic photocurrent is underway. Thus, these initial investigations of two new *p*-type semiconductors show that they can be prepared as polycrystalline films and which are promising for their potential use in solar-energy-to-fuels production.

The second section described in this dissertation involves investigations into the half-metallic double-perovskite oxides with the composition A_2BReO_6 (A = Sr or Ba; B = Fe or Cr). These double-perovskites have been the focus of intense research interest owing to the discovery of high magnetic-ordering transition temperatures and half-metallic properties in

members of this family.⁷⁻¹¹ Interestingly, large magnetoresistances have been measured in their polycrystalline forms that result from spin-polarized intergrain tunneling across the particle grain boundaries, and, as expected, is absent in the analogous single-crystal measurements.¹² The particle size, morphology and the amount of B/B' site ordering in polycrystalline samples have been shown to significantly effect their intergrain tunneling magnetoresistances. However, current synthesis methods do not allow for the tunable manipulation of the particles.¹³⁻¹⁵

Synthesis of members in this family of compounds in high purity and homogeneity is often hard to achieve by their current preparation methods. Furthermore, these methods provide no control over particle size or morphology, and which strongly impact their magnetic properties. The use of molten-salt fluxes as synthesis media has been shown to yield a significantly greater flexibility to modulate metal-oxide particle sizes and microstructures by changing the amount and type of flux, reaction time and temperature, and also cooling rates. These investigations described herein have been primarily focused on the use of flux synthesis to probe the effects of particle size and surface variation on the extent of B/B' site ordering, as well as magnetic and electrical properties.

The use of a NaCl/KCl flux in the synthesis of $\text{Sr}_2\text{FeReO}_6$, $\text{Ba}_2\text{FeReO}_6$ and $\text{Sr}_2\text{CrReO}_6$ resulted in high-purity homogeneous distributions of particles prepared at temperatures much lower than the previously reported solid-state preparations. The smallest particle sizes of ~50 nm could be prepared for $\text{Sr}_2\text{FeReO}_6$, and which could be increased in size up to ~500 nm by increasing the reaction duration. By contrast, relatively larger

particles of $> 1\ \mu\text{m}$ were formed for $\text{Ba}_2\text{FeReO}_6$ after only a 6 h reaction using either a 1:1 or 3:1 flux ratio.

Rietveld refinements of the powder X-ray diffraction patterns for all flux reaction conditions were investigated in order to determine the extent of the B/B' site ordering. The extent of B/B' site ordering was found to increase with reaction duration of $\text{Sr}_2\text{FeReO}_6$ while there was no significant effect of the shorter flux-reaction times for $\text{Ba}_2\text{FeReO}_6$ and $\text{Sr}_2\text{CrReO}_6$. The degree of Fe/Re site ordering ranged from 90-96 % for $\text{Ba}_2\text{FeReO}_6$ and ~83-84 % for $\text{Sr}_2\text{FeReO}_6$. Significantly, larger magnetization values were observed for the $\text{Ba}_2\text{FeReO}_6$ samples as compared to $\text{Sr}_2\text{FeReO}_6$ as a result of lower Fe/Re site ordering. Further, the larger particle sizes of $\text{Ba}_2\text{FeReO}_6$ also serve to decrease the amount of grain boundaries that are magnetically-disordered. The measured resistivities of all flux-prepared samples were roughly 2 - 5 \times larger than the previously reported literature values,^{8,10,16,17} and which arises from the increased concentration of grain boundaries. Furthermore, large temperature-dependent magnetoresistivities of ~70%, ~65% and ~70% were observed for the flux-prepared $\text{Sr}_2\text{FeReO}_6$, $\text{Ba}_2\text{FeReO}_6$ and $\text{Sr}_2\text{CrReO}_6$, respectively, owing to the increased concentration of grain boundaries. From these studies, flux synthesis has shown to be a valuable synthetic method for the synthesis of double-perovskites with size-dependent magnetoresistance properties.

Potential (V) vs. RHE at pH 6.3

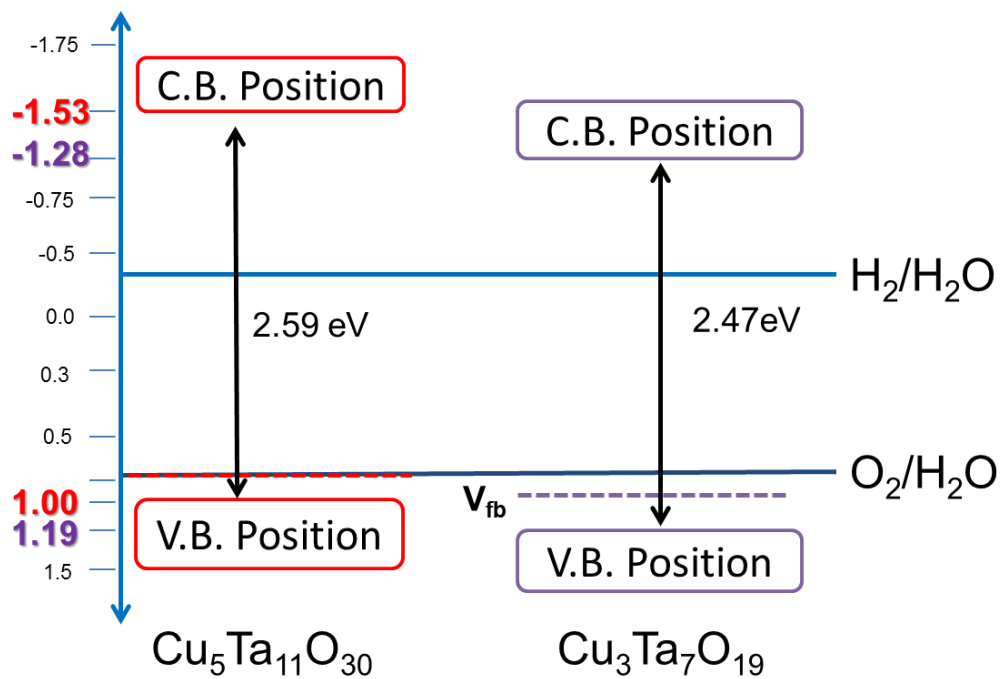


Figure 6.1. The valence and conduction band positions for Cu₅Ta₁₁O₃₀ and Cu₃Ta₇O₁₉ determined from their flat-band potentials vs. RHE (pH = 6.3) with respect to the water oxidation and reduction potentials.

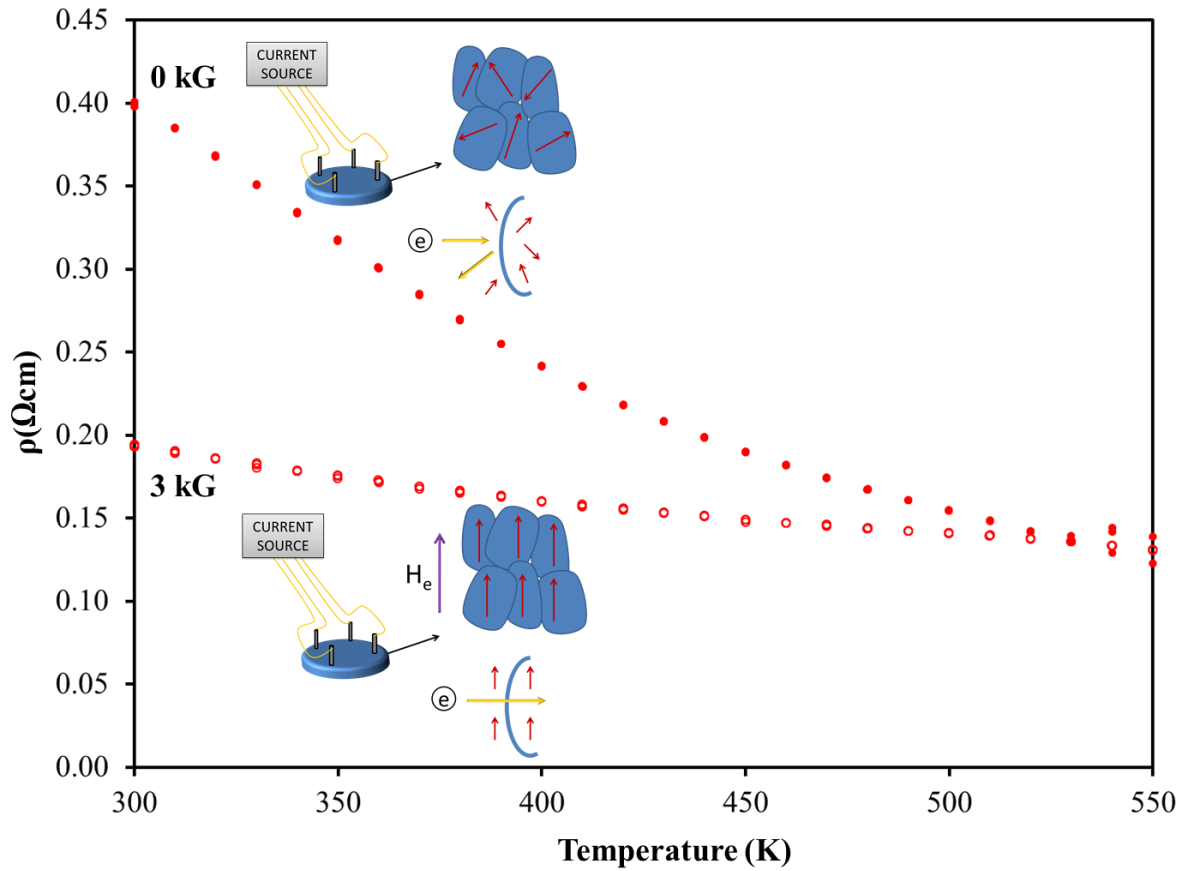


Figure 6.2. Temperature and magnetic-field dependence of the resistivity for a polycrystalline $\text{Sr}_2\text{FeReO}_6$ pellet prepared by flux synthesis. Also shown is an illustration of ITMR where the set up above is in the absence of a magnetic field where tunneling is disfavored. The set up on the left represents the tunneling of an electron that occurs in the presence of a magnetic field.

REFERENCES

- (1) Abe, R. *Photochem. Rev.* **2010**, *11*, 179.
- (2) Rajeshwar, K. *J. Appl. Electrochem.* **2007**, *37*, 765.
- (3) Fujishima, A.; Honda, K. *Nature* **1972**, *315*.
- (4) Aroutiounian, V. M.; Arakelyan, V. M.; Shahnazaryan, G. E. *Solar Energy* **2005**, *581*.
- (5) Joshi, U.; Palasyuk, A. M.; Maggard, P. A. *J. Phys. Chem. C* **2011**, *115*, 13534.
- (6) Li, G.; T., K.; Wang; D.; Zou, Z.; Ye, J. *J. Phys. Chem. Solids* **2008**, *69*, 2487.
- (7) Kobayashi, K.-I., Kimura, T., Sawada, H., Terakura, K., Tokura, Y. *Nature* **1998**, *395*, 677.
- (8) Kobayashi, K.-I., Kimura, T., Y. Tomioka, H. Swada, K. Terakura, Y. Tokura *Phys. Rev. B* **1999**, *59*, 159.
- (9) Serrate, D., De Teresa, J.M., Ibarra, M.R. *J. Phys.: Condens. Matter* **2007**, *19*, 023201.
- (10) Kato, H., Okuda, T., Okimoto, Y., Tomioka, Y., Oikawa, K, Kamiyama, T., Tokura, Y *Phys. Rev. B* **2004**, *69*.
- (11) Kato, H., Okuda, T., Okimoto, Y., Tomioka, Y, Takenoya, Y., Ohkubo, A., Kawasaki, M., Tokura, Y. *Appl. Phys. Lett.* **2002**, *81*.
- (12) Tomioka, Y., Okuda, T., Okimoto, Y., Kumai, R., Kobayashi, K.-I. *Phys. Rev. B* **2000**, *61*, 422.
- (13) Balcells, J.; Navarro, M.; Bibes, M.; Roig, A.; Martinez, B.; Fontcuberta, J. *Appl. Phys. Lett.* **2001**, *78*.

- (14) Jacobo, S. E., Duhalde, S., Mercader, R.C. *physica B* **2004**, 354, 59.
- (15) Yuan, C. L., Wang, S.G., Song, W.H., Yu, T., Dai, J.M., Ye, S.L., Sun, Y.P. *Appl. Phys. Lett.* **1999**, 75, 3853.
- (16) Alamelu, M., Varadaraju, U.V., Venkatesan, M., Douvalis, A.P., Coey, J.M.D *J. Appl. Phys.* **2002**, 91, 8909.
- (17) Teresa, J. M., Serrate, D., Blasco, J., Ibarra, M.R., Morellon, L. *Phys. Rev. B* **2004**, 69.